

Tuning the Localized Surface Plasmon Resonance in Copper Chalcogenide Nanoparticles

Von der Naturwissenschaftlichen Fakultät der
Gottfried Wilhelm Leibniz Universität Hannover

zur Erlangung des Grades

Doktor der Naturwissenschaften (Dr. rer. nat.)

genehmigte Dissertation

von

Andreas Wolf, M.Sc.

2016

Referent: Prof. Dr. rer. nat. Jürgen Caro
Korreferent: Dr. rer. nat. Nadja-Carola Bigall
Korreferent: Prof. Dr. rer. nat. Alexander Eychmüller
Tag der Promotion: 15.12.2016

Preface

The present thesis shows the results that I achieved during my time as a researcher in the research group of Dr. Dirk Dorfs, a subgroup of Prof. Dr. Jürgen Caro's group, at the Gottfried Wilhelm Leibniz Universität Hannover, Institute of Physical Chemistry and Electrochemistry from 2012 until 2016. The work was financed by DFG research grant DO 1580/3-1 under the guidance of Dr. Dirk Dorfs and Prof. Dr. Jürgen Caro.

In this thesis 4 selected scientific articles are presented, of which I am the first author. Furthermore, I am co-author of 3 publications that are not included in this thesis, yet have been written during the time of my dissertation and are listed in chapter 6. In the following I will point out my contributions to the articles included in this thesis. I would like to acknowledge the supervision, support and valuable discussions during the preparation of all manuscripts by Dr. D. Dorfs.

The first article, *Tuning the LSPR in Chopper Chalcogenide Nanoparticles by Cation Intercalation, Cation Exchange and Metal Growth*, which is presented in chapter 2.2, was written by me. I conducted the syntheses, sample preparations, optical spectroscopy, X-ray diffraction (XRD) analysis, energy dispersive X-ray (EDX) spectroscopy measurements, scanning transmission electron microscopy (STEM) measurements, atomic absorption spectroscopy (AAS) and all data interpretations. Some preliminary cation exchange experiments were conducted by T. Kodanek during his master thesis under my supervision. Furthermore, the conventional transmission electron microscopy (TEM) measurements by him are kindly appreciated.

The second article, *Growth of $\text{Cu}_{2-x}\text{Se}-\text{CuPt}$ and $\text{Cu}_{1,1}\text{S}-\text{Pt}$ Hybrid Nanoparticles*, is presented in chapter 2.3, was written by me. Here I performed the syntheses, sample preparations, optical spectroscopy, XRD analysis, EDX spectroscopy measurements, STEM measurements, AAS and all data interpretation. I thank D. Hinrichs for the conventional TEM measurements; Dr. J. Sann for the X-ray photoelectron

spectroscopy (XPS) measurements and support with XPS data interpretation; and J. F. Miethel for the measurements of cyclic voltammograms.

The third article, *Synthesis of Plasmonic Cu_{2-x}Se@ZnS Core@Shell Nanoparticles*, is presented in chapter 3.2, was written by me. I performed the syntheses, XRD analysis, optical spectroscopy, STEM measurements and all data interpretations. The conventional TEM measurements by D. Hinrichs and the electrodynamic calculations by T. Härtling are kindly appreciated.

The fourth article, *Plasmonic Semiconductor Nanoparticles in a Metal-Organic Framework Structure and Their in Situ Cation Exchange*, is presented in chapter 4.2, was written by me. I conducted the syntheses (except ITO NP fabrication), most EDX spectroscopy measurements, STEM measurements, optical spectroscopy, XRD analysis, AAS and all data interpretations. I am grateful to T. Kodanek for the conventional TEM measurements; to F. Lübke for the EDX spectroscopy measurements of the ITO@ZIF-8 particles, and the SEM measurements; to T. Mohamed for the ITO NP synthesis; and to L. Diestel and Prof. J. Caro for the ZIF-8 XRD simulation as well as valuable discussions.

Abstract

This thesis explores multiple approaches to tune the localized surface plasmon resonance (LSPR) of colloidal copper chalcogenide nanoparticles (NPs). The main focus lies on two representatives of this group: degenerately copper-vacancy doped Cu_{2-x}Se NPs, and $\text{Cu}_{1.1}\text{S}$ covellite NPs, whose high charge carrier density originates from lattice constitutional free holes. Both exhibit, by redox reactions post synthetically tunable LSPRs.

The first objective of this thesis was to reduce the air-sensitivity after the controlled tuning of the LSPR. In order to achieve this, a partial cation exchange, and intercalation of Ag(I) and Au(I) into Cu_{2-x}Se and $\text{Cu}_{1.1}\text{S}$ was conducted, respectively. The changes of the LSPR were then compared to the changes induced by Cu(I) treatment. The results showed that the damping and shifting of the LSPR caused by Ag(I) and Au(I) are significantly more stable under exposure to air. Furthermore, metal-copper chalcogenide hybrids were grown. Specifically, dual plasmonic Au- Cu_{2-x}Se NPs with surprisingly little interaction between the two LSPRs, as well as CuPt- Cu_{2-x}Se and Pt- $\text{Cu}_{1.1}\text{S}$ hybrids, were synthesized. The growth of Pt containing domains resulted in the complete damping of the LSPR with already very small amounts of Pt.

The second objective of the present work was the separation of the plasmonic core from environmental influences. A synthesis strategy was developed which yielded a crystalline, closed ZnS shell with controlled and homogeneous thickness. The resulting $\text{Cu}_{2-x}\text{Se}@Zn\text{S}$ core@shell NPs were fabricated under preservation of the plasmonic properties of the core. The ZnS shell significantly slowed down oxygen induced oxidation of the core, and protected it fully against strong reducing agents.

In a further step, p-type doped Cu_{2-x}Se NPs as well as n-type doped indium tin oxide (ITO) NPs were encapsulated in nanoporous ZIF-8 particles. The encapsulation was achieved under conservation of their individual plasmonic properties, with independent

control over the loading and size of the resulting $\text{Cu}_{2-x}\text{Se}@ZIF-8$, and $\text{ITO}@ZIF-8$ composite particles. The encapsulation fixed the NPs within the framework, preventing agglomeration, but at the same time allowed controlled access to the NPs. The accessibility was shown by *in situ* cation exchange reactions of the $\text{Cu}_{2-x}\text{Se}@ZIF-8$ composite particles, yielding $\text{Ag}_2\text{Se}@ZIF-8$ and $\text{HgSe}@ZIF-8$ composites, while retaining the structural integrity of the ZIF-8.

In summary, multiple approaches to tune and stabilize copper chalcogenide NP LSPRs were developed.

Keywords: Localized Surface Plasmon Resonance, Nanoparticle,
Copper Chalcogenide

Zusammenfassung

Die vorliegende Dissertation untersucht mehrere Methoden die lokalisierte Oberflächenplasmonenresonanz (LSPR) von Kupfer-Chalkogeniden einzustellen. Der Schwerpunkt wurde dabei auf zwei Vertreter dieser Gruppe gelegt: durch Kupfervakanzen entartet dotierte Cu_{2-x}Se Nanopartikel (NP) und $\text{Cu}_{1,1}\text{S}$ Covellin NP, deren hohe Konzentration an freien Ladungsträgern durch strukturbedingte Elektronenfehlstellen hervorgerufen werden. Beide Verbindungen besitzen LSPR, welche durch Redoxreaktionen einstellbar sind.

Ein Schwerpunkt der hier vorgestellten Dissertation war die Reduzierung der Luftempfindlichkeit nach der kontrollierten Einstellung der LSPR. Hierfür wurden Ag(I) und Au(I) in Cu_{2-x}Se und $\text{Cu}_{1,1}\text{S}$ über Kationenaustausch bzw. Kationeninterkalation eingebracht. Die auftretenden Änderungen der LSPR wurden mit denen, die durch die Behandlung mit Cu(I) hervorgerufen wurden, verglichen. Die Ergebnisse zeigten, dass die durch Ag(I) und Au(I) verursachten Dämpfungen und Verschiebungen eine signifikant höhere Beständigkeit gegenüber Sauerstoff aufweisen. Darüber hinaus wurden in dieser Arbeit auch Kupfer-Chalkogenide-Metall Hybride synthetisiert. So wurden dual-plasmonische $\text{Au-Cu}_{2-x}\text{Se}$ Hybride, deren LSPRs nur minimale Wechselwirkungen aufweisen, sowie $\text{CuPt-Cu}_{2-x}\text{Se}$ und $\text{Pt-Cu}_{1,1}\text{S}$ Hybride dargestellt. Hierbei sorgten bereits geringe Menge an Pt für eine vollständige Dämpfung des LSPR.

Ein weiterer Kernpunkt dieser Arbeit war die Abschirmung des plasmonischen Kernes von Einflüssen des umgebenden Mediums. Es wurde eine Synthesestrategie entwickelt, welche zum erfolgreichen Aufwachsen einer geschlossenen, homogenen und kristallinen ZnS -Schale führte, deren Stärke einstellbar ist. Die plasmonischen Eigenschaften des Kernes wurden in den resultierenden $\text{Cu}_{2-x}\text{Se@ZnS}$ Kern@Schale NP erhalten. Die ZnS -Schale führte zu einer signifikanten Verlangsamung der

Sauerstoff induzierten Oxidation des Kernes, und schirmte diesen außerdem vollständig gegen starke Reduktionsmittel ab.

Des Weiteren wurden sowohl p-dotierte Cu_{2-x}Se NP, als auch n-dotierte Indiumzinnoxid (ITO) NP in nanoporöse ZIF-8 Partikel eingebunden. Die Einkapselung erfolgte unter unabhängiger Kontrolle über Beladung und Größe der $\text{Cu}_{2-x}\text{Se}@ZIF-8$ und $\text{ITO}@ZIF-8$ Kompositpartikel, wobei die individuellen plasmonischen Eigenschaften bewahrt wurden. Durch Fixierung der NP in der Gerüststruktur wird eine Agglomeration verhindert. Zugleich bleibt jedoch der Zugang zu den NP erhalten. Dies wurde gezeigt durch die Umwandlung von $\text{Cu}_{2-x}\text{Se}@ZIF-8$ in $\text{Ag}_2\text{Se}@ZIF-8$ bzw. $\text{HgSe}@ZIF-8$ Komposit-Partikeln durch *in situ* Kationenaustauschreaktionen. Hierbei wurde die strukturelle Integrität des ZIF-8 erhalten.

Zusammenfassend wurden vielfältige Ansätze entwickelt, die die erfolgreiche Einstellung und Stabilisierung von Kupfer-Chalkogenid NP LSPR ermöglichen.

Schlagwörter: Lokalisierte Oberflächenplasmonenresonanz, Nanopartikel,
Kupfer-Chalkogenide

Contents

Preface	I
Abstract	III
Zusammenfassung	V
Contents	VII
1 Introduction	1
1.1 General Introduction and Motivation	1
1.2 Nanoparticle Synthesis	5
1.2.1 Direct NP Synthesis.....	5
1.2.2 Core@Shell NP Synthesis	6
1.2.3 Cation Exchange in Ionic NPs.....	7
1.3 LSPR Theory in Metals	9
1.3.1 Drude-Sommerfed Theory	9
1.3.2 Quasi-Static Approximation.....	10
1.3.3 Mie Theory	15
1.4 Plasmonic Semiconductor Nanoparticles	17
1.5 Metal Organic Framework Composites.....	22
1.5.1 Metal Organic Frameworks.....	22
1.5.2 NP@MOF-Composites	23
1.6 References.....	25

2	Tuning the LSPR by Metal Growth, Cation Intercalation & Exchange	37
2.1	Summary	37
2.2	Tuning the LSPR in Copper Chalcogenide Nanoparticles by Cation Intercalation, Cation Exchange and Metal Growth	40
2.3	Growth of Cu_{2-x}Se -CuPt and $\text{Cu}_{1.1}\text{S}$ -Pt Hybrid Nanoparticles	53
3	Encapsulation of Cu_{2-x}Se in a Closed ZnS Shell	67
3.1	Summary	67
3.2	Synthesis of Plasmonic Cu_{2-x}Se @ZnS Core@Shell Nanoparticles	69
4	Encapsulation of Plasmonic Semiconductor NPs in a Porous Shell	80
4.1	Summary	80
4.2	Plasmonic Semiconductor Nanoparticles in a Metal-Organic Framework Structure and Their <i>in Situ</i> Cation Exchange	82
5	Closing Remarks	98
6	Appendix	102
	Acknowledgement	105

1 Introduction

1.1 General Introduction and Motivation

Nowadays, nanoscience has become a focus point within research activities.¹⁻³ The tuning of properties by control over composition, size and shape represents a promising potential for applications in many different sectors, like *e.g.* photovoltaic, optoelectronic, catalytic or bio/medical fields. Advanced synthesis methods, developed within the last 30 years since the Henglein group started the colloidal semiconductor nanocrystal (NCs)^{4,5} – quantum dots- research, enable the controlled synthesis of advanced shapes, while enabling high control over composition and crystal phase. For semiconductor nanoparticles (NPs) in a size regime of and below the size of the exciton, the confinement causes the quantization of their energy levels.⁶ The resulting optical properties have fueled the research in size and shape controlled syntheses, as well as in the development of their applications, *e.g.* in solar cells, displays and biological imaging.^{3,7}

Nanosized noble metal nanoparticles exhibit a different, but at the same time highly fascinating effect. When their free electrons are excited by an electromagnetic field, they collectively oscillate. Due to the small particle size this coherent oscillation cannot propagate. When the frequency of the exciting light becomes resonant with the electron oscillation, this is called localized surface plasmon resonance (LSPR).⁸⁻¹⁰ The material, size, shape and wavelength dependent absorption and scattering properties, caused by the LSPR, were (unknowingly) used since the seventeenth century, when church glass windows were stained red and purple, by what nowadays are known to be gold nanoparticles.¹¹ After intensive research in the last decades, the decorative feature is only a small fraction of the possible applications from LSPRs. LSPRs are used in a broad range of applications, such as surface enhanced Raman spectroscopy

(SERS),^{9,12,13} plasmon enhanced fluorescence,^{13,14} bio-diagnostics (*e.g.* pregnancy tests),¹⁵⁻¹⁷ photothermal therapy,¹⁸ light antennas or scattering elements in photovoltaics,¹⁹ etc.

However, noble metal based plasmonic NPs exhibit also considerable disadvantages. A significant tuning of their LSPRs is mainly possible during synthesis by control over shape and composition. Furthermore, noble metal NP LSPRs are mostly restricted to the visible spectral range, owing to their high charge carrier densities of 10^{22} - 10^{23} cm^{-3} , and can be shifted into the second biological window in the NIR only with very large particles or shape control. This spectral region of 1000-1350 nm is highly interesting for biological applications, as body tissue exhibits at these wavelengths low absorption coefficients, thus enabling a deep penetration depth.²⁰⁻²² Both limitations can be overcome by materials with a slightly lower and tunable free carrier concentration – degenerately doped semiconductor nanoparticles. Their tunable charge carrier density of up to 10^{21} cm^{-3} still supports a plasmon resonance, but is more than a magnitude lower than that of noble metals. Therefore the LSPR of these NPs is situated in the NIR or MIR part of the spectrum.²³⁻²⁵ Hence, degenerately doped semiconductor NPs present a continuous bridge between metal NPs and intrinsic semiconductor NPs.

Copper chalcogenides (*e.g.* Cu_{2-x}Se , Cu_{2-x}S , Cu_{2-x}Te) are attractive materials, as they have a high environmental compatibility, high biocompatibility, high abundance and comparably low costs.^{26,27} Furthermore, they allow a continuous study of their properties depending on their charge carrier concentration. As vacancy doped semiconductors, their charge carrier concentration can be controlled by defining their vacancy density. A process that can be easily achieved post synthetically through oxidation and reduction.^{23,24,28} Several articles in recent years have proven the origin of their strong NIR absorbance band to be a LSPR and studied its dependence on the vacancy state, refractive index of the environment, plasmon coupling, etc.^{23,24,28-33} A special case is covellite ($\text{Cu}_{1.1}\text{S}$) as it is a stoichiometric compound with lattice constitutional free holes.

While their highly adjustable properties are advantageous, on the one side, it also raises concerns with respect to future applications. Even though the application of this material was shown to be usable in a laboratory environment (*e.g.* for photothermal therapy³⁴ and pet sterilization³⁵) strong concerns are the long term stability of their

optical properties. Therefore, in this thesis various chemical approaches to tune the LSPR of Cu_{2-x}Se and $\text{Cu}_{1,1}\text{S}$ are investigated with a special focus on increasing the chemical and optical stability of the particles while retaining their accessibility for *e.g.* sensing applications and their strong LSPR for *e.g.* photothermal therapy.

The high sensitivity of copper chalcogenide NPs LSPRs towards oxygen of ambient air has been described in literature.^{23,24} Attaining higher stability of the as needed tuned LSPR should therefore be studied to facilitate applications beyond laboratory conditions. Hence, chapter 2.2 of this thesis compares the temporal stability of the changes induced to the LSPR of Cu_{2-x}Se berzelianite and $\text{Cu}_{1,1}\text{S}$ covellite NPs by reduction with Cu(I) ions to the effects that result from Ag(I) and Au(I) ion treatment.

So far in literature mainly the exciton – plasmon coupling in intrinsic semiconductor – metal hybrids (especially Au-CdSe and Au-CdS hybrids)³⁶⁻³⁹ has been studied. However, the interactions of metal domains with heavily doped plasmonic semiconductor NPs have been subject of only few recent articles.⁴⁰⁻⁴² In order to further the understanding of the interactions between highly p-type doped semiconductor and metal domains in hybrid NPs synthesis protocols for respective hybrids need to be developed, and their optical changes because of the metal domain be investigated. This is done in chapter 2. Specifically, in chapter 2.2 the growth of an Au domain, in a mild reaction condition, onto an existing Cu_{2-x}Se NP is developed. Subsequently, the interactions of the two LSPRs of the synthesized Cu_{2-x}Se -Au hybrid NP are characterized. Additionally, the strong influence of Pt containing metal domains on the LSPR of a copper chalcogenide NP is presented in chapter 2.3, by synthesizing and characterizing Cu_{2-x}Se -CuPt and in $\text{Cu}_{1,1}\text{S}$ -Pt hybrid structures.

Whereas enhancing the LSPR stability by cation exchange is one approach, the physical protection of the plasmonic LSPR is another. A classic approach in nanoscience is the separation of the optical active core from the environment by an inert inorganic shell. Protecting the Cu_{2-x}Se NPs from the environment is important in bio-applications, to avoid uncontrolled alteration of the optical properties or even fast disintegration of the whole Cu_{2-x}Se NPs. In order to study the effect of an inorganic shell on plasmonic Cu_{2-x}Se NPs, Cu_{2-x}Se @ZnS core@shell particles are fabricated. The thickness controlled synthesis procedure of such a homogeneous ZnS shells is

presented in chapter 3. The protective properties and the effect on the core NP LSPR is then compared to the uncoated NPs when exposed to air and reducing agents.

The complete encapsulation with a closed, inorganic shell is especially interesting for applications as photothermal agent, as these do not require direct access to the plasmonic core. For applications in sensing this is an unsuitable approach, as for this the shell needs to allow the penetration of the analyte, while ideally protecting the plasmonic NPs from the matrix. With a defined pore size zeolitic imidazolate framework-8 (ZIF-8) offers these properties. Accordingly, the encapsulation procedure of multiple plasmonic semiconductor NPs in a nanoporous ZIF-8 crystal is shown in chapter 4. The fixation of p-type doped Cu_{2-x}Se , as well as n-type doped indium tin oxide (ITO) NPs in the metal-organic framework prevents agglomeration under preservation of their individual plasmonic properties in the resulting $\text{Cu}_{2-x}\text{Se}@ZIF-8$ and $\text{ITO}@ZIF-8$ composite particles. Moreover, the *in situ* cation exchange of the encapsulated Cu_{2-x}Se NPs is shown, resulting in $\text{Ag}_2\text{Se}@ZIF-8$ and $\text{HgSe}@ZIF-8$ composites.

1.2 Nanoparticle Synthesis

1.2.1 Direct NP Synthesis

The development in semiconductor nanocrystal syntheses since the 1980s^{5,6} resulted in a vast amount of synthesis protocols that enable high control during synthesis. Today, the nanocrystal community is able to specifically fabricate colloidal nanoparticles with defined sizes, morphologies and aspect ratios for many chemical compositions.^{1,3,43-45} While the focus of research was first on the development of colloidal semiconductor materials, synthesis concepts have been transferred to the synthesis of other materials (*e.g.* metals and metal oxides).⁴⁶

From the various approaches, the surfactant controlled growth in hot organic solvents especially results in high quality semiconductor nanoparticles (NPs). Generally, for this strategy the synthesis is controlled by the precursor(s), organic ligands(s), solvent(s) and the temperature program. At sufficiently high temperatures the precursors decompose yielding the atomic or molecular reactant, which later form the nanocrystals. The formation generally occurs in two steps: the nucleation and the subsequent growth of the NPs.⁴⁶ The importance of the separation of nucleation and growth for a small size distribution was already discussed by LaMer *et al.* in the 1950s.⁴⁷

One method, resulting in high quality semiconductor NPs with a small size distribution, is the *hot-injection* approach and was originally developed by Murray *et al.*^{44,48} The “cold” solution of precursors are rapidly injected in the reaction solution at high temperatures causing a sudden decomposition of the precursors resulting in a supersaturation of the reactive monomers, followed by a discrete nucleation burst. The monomer consumption, and the accompanying temperature drop cause a rapid decrease of the reactant concentration below the nucleation limit preventing further nucleation during the subsequent growth of the initially formed seeds. The surfactants in the reaction medium attach to the surfaces of the growing NCs, stabilize them, slowing the growth rate and hence allowing the NCs to anneal.^{44,46,49}

The *heat up* approach was developed later. For this purpose the precursors are mixed at low temperatures. The nucleation and the following growth process are initiated through a fast heating of the complete reaction mixture. While comparably giving less

control over the separation of nucleation and growth stage, the advantage of this method is that it is potentially more scalable and gives a higher reproducibility.⁴⁹

Stopping the reaction after depletion of the monomers is essential, as the critical size will become larger than the size of the formed NCs, resulting in a wider size distribution due to Ostwald ripening.⁴⁶

These methods often use a kinetic control, achieved by fast growth rates to limit size distribution and realize shape control. The growth rate of a crystal facet is exponentially increasing with its surface energy.⁴⁶ Hence, crystal facets with larger surface energy grow faster in a kinetically controlled synthesis, enabling the fabrication of non-spherical, non-equilibrium NCs, such as: platelets, disks, rods and multipods.⁵⁰⁻⁵⁷ This can be further directed through the choice of ligand(s) that selectively coordinate only to certain crystal facets, reducing their surface energy.⁴⁶

1.2.2 Core@Shell NP Synthesis

Since the late 1980s, research showed that the properties of colloidal nanoparticles can be modified and improved by being covered with an inorganic shell material.^{5,58} For example the growth of a shell on semiconductor NPs enables the trapping of the excited electron and the electron hole of an exciton in specific parts of the core@shell particle, depending on the energy levels of the chosen material combination. Type I structures (energy gap of the core lies within the energy gap of the shell) for example enable the confinement of the exciton in the core, the passivation of the core surface and the core's separation from the surrounding medium.⁵⁸⁻⁶¹ Additional to enhanced optical properties,^{59,61,62} the core protection with a shell can also result in a better core stability and a higher biocompatibility through the choice of a less toxic shell material.^{63,64}

The optical properties of plasmonic metal core NPs are as well strongly depending on the shell material. Coating a metal NP with different dielectric materials is changing its dielectric environment, which results in a shift of its LSPR (as will be discussed in detail in chapter 1.3.1).⁶⁵⁻⁷⁰

Multiple approaches are available for the synthesis, and they can be grouped into two types. The one batch approach: firstly the core NP is synthesized, and without an

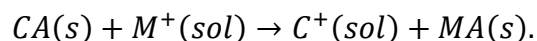
intermediate cleaning step, the shell is grown by the subsequent addition of the shell-precursors. Contrary, in the second approach the core particles are synthesized, cleaned, and in a second step brought into the reaction medium for the shell growth. While the one batch is less tedious, the separation of core and shell growth avoids impurities and gives a higher control of the reaction conditions.⁷¹

A key factor for the successful growth of the shell is the inhibiting of homogeneous nucleation of separated shell material NPs. This fact, and the controlled thickness of the shell deposited can be realized similarly to the homogeneous nucleation of NPs, by the core accessibility (*e.g.* through suitable ligands), precursor reactivity, addition sequence, addition rate, and temperature program.³⁹

1.2.3 Cation Exchange in Ionic NPs

As discussed before, the fabrication of NPs of various sizes, shapes and compositions can be achieved through a diverse range of direct synthesis approaches. However, many other NP compositions are still not realizable. The development of synthesis protocols especially for multi element alloys can be an extremely challenging, and in some cases an impossible task due to the different reaction kinetics of the employed precursors. Cation exchange (CE) enables the access to these previously not available NCs. *Via* CE NCs of the intensely studied II-VI and IV-VI compounds, which can be readily synthesized in various sizes and shapes, can be transformed in a simple step.⁷²⁻⁷⁶ For example, it was used to synthesize sphalerite CdSe NC from cubic Cu_{2-x}Se NCs, which subsequently were used in a seeded growth approach resulting in octapod shaped CdSe NPs.⁵³ Although this technique was known from bulk material for decades, it only started to get into focus of NP synthesis in the last decade after a work from Son *et al.*⁷⁷ Even so, first works have been already presented in the early 1990s.⁷⁸⁻⁸⁰ The advantage for the reaction with NCs is the reaction speed, as a full exchange at room temperature can often be achieved within seconds (compared to several weeks at high temperature for bulk materials) due to their large surface area, much shorter diffusion length and lower activation barriers for diffusing ions.⁷²

A CE process can be illustrated as followed (for a simplified case of an isovalent CE):



To understand the overall energy balance, and thermodynamic driving force of the process Rivest *et al.* proposed to split it into 4 steps: dissociation of CA , desolvation of M^+ , association of M and A and solvation of C . Association and dissociation steps are defined by the lattice and surface energies. The solvation and desolvation energies of the cations are defined by the involved ions, solvents and possible ligands. Furthermore, for non-isovalent CEs the entropy has to be taken into account. In addition, also reaction kinetics, such as activation barriers and mobility of ions have to be considered.^{72,73}

Full CE allows the synthesis of NPs with a homogeneous composition that might not be directly accessible, on the other hand partial CE enables the fabrication of hetero structures. Depending on the miscibility of the starting and exchanged material, a partial cation exchange can lead to alloyed, segmented or core@shell structures.⁷³

Particularly, copper chalcogenides have been found to be an efficient starting point^{53,81-87} (respectively intermediate and final product)^{76,88-94} for CE reactions. Their suitability for CE protocols is partially due to the high mobility of Cu(I) ions, originating from their small size and charge.²⁷ However, the cation mobility (Cu(I) and guest cations) is also enhanced because of the high amount of copper vacancies in the nanocrystals, which further boost the cation exchange.^{73,82,95,96} An interesting recent work on a partial cation exchange with covellite NPs by Xi *et al.* examined why divalent ions could only be exchanged into the particle in a reducing environment. They authors showed that an reducing agent aided in the braking of the, for covellite typical, S-S bonds, allowing the bivalent ions to push out Cu(I) ions either to solution or to other regions of the NP. Hence forming CdS or HgS domains in a copper sulfide particle, but not allowing a full cation exchange.

1.3 LSPR Theory in Metals

1.3.1 Drude-Sommerfeld Theory

The Drude-Lorentz-Sommerfeld model is a simplified approach to model the dielectric function of metals. It explains the optical properties of metals by treating the conduction band electrons as quasi-free electrons that form an electron gas and move against the immobile positive ion cores.⁸⁻¹⁰ The contributions of valence band electrons (*e.g.* through interband transitions) to the spectra are however neglected in the Drude theory. Due to the neglect of these effects, considerable deviations are observed in the visible and ultraviolet spectral range, as photons have enough energy to excite interband transitions. Nonetheless, for the near-infrared spectral region it models well the optical behavior of free-electron metals.^{8,9} The Drude model further assumes that the electrons in a metal particle behave coherent upon excitation, and treats the macroscopic response as a multiple of the behavior of an individual electron with the electron density.⁸

The motion of a free electron with the elementary charge e and the effective optical mass m_{eff} (to account for the interactions of the electrons with the ion cores) can be described as follow:

$$m_{eff} \frac{\partial^2 r}{\partial t^2} + m_{eff} \gamma \frac{\partial r}{\partial t} = e E_0 e^{-i\omega t}. \quad 1$$

Where $E = E_0 e^{-i\omega t}$ is the electrical component of the exciting electromagnetic field that leads to the displacement r of an electron.⁸ γ denotes the phenomenological damping constant of the oscillation of the free electrons due to collisions with phonons, electrons, lattice defects, and impurities. Additionally it is related by $\gamma = \frac{1}{\tau} = \frac{v_F}{l}$ to τ the mean time between two subsequent collision events of an electron. l denotes the mean free path of an electron and v_F the Fermi velocity. As a result of the displacement of the electron, a charge separation is created, which causes the dipole moment p .^{8,9} By multiplying this by N , the number of electrons per unit volume, one obtains the polarization P :

$$P = Np = Ner_0. \quad 2$$

Furthermore, we assume an isotropic media ($P \parallel E$). The frequency dependent dielectric function $\varepsilon(\omega)$ relates to the polarization by:

$$\varepsilon(\omega) = 1 + \frac{P}{\varepsilon_0 E(\omega)}, \quad 3$$

with ε_0 being the vacuum permittivity. Furthermore, $\varepsilon(\omega)$ relates to the complex index of refraction by $n(\omega) = n(\omega) + i\kappa(\omega) = \sqrt{\varepsilon(\omega)}$, with $n(\omega)$ being the real part of the refractive index, and $\kappa(\omega)$ the extinction coefficient.^{8,9} Hence, the complex, frequency dependent dielectric function of a system with free electrons is given by:¹⁰

$$\varepsilon(\omega) = \varepsilon_1(\omega) + i\varepsilon_2(\omega) = 1 - \frac{\omega_p^2}{\omega^2 + i\gamma\omega}. \quad 4$$

With ω_p the plasma frequency of the free electrons:¹⁰

$$\omega_p^2 = \frac{Ne^2}{\varepsilon_0 m_{eff}}. \quad 5$$

The real and the imaginary parts of the dielectric function are written as:¹⁰

$$\varepsilon_1(\omega) = n(\omega)^2 - \kappa(\omega)^2 = 1 - \frac{\omega_p^2}{\omega^2 + \gamma^2}, \quad 6$$

$$\varepsilon_2(\omega) = 2n(\omega)\kappa(\omega) = 1 - \frac{\omega_p^2\gamma}{\omega(\omega^2 + \gamma^2)}. \quad 7$$

The polarization of the material is represented in the real part $\varepsilon_1(\omega)$ of the dielectric function, whereas the absorption (*e.g.* due to interband transitions) is represented in the imaginary part $\varepsilon_2(\omega)$.^{8,9}

1.3.2 Quasi-Static Approximation

A plasmon is the density oscillation of the free charge carriers in a conductor. At the interface between a conductor and a dielectric material the so called surface plasmon can propagate along the surface. Due to the spatial confinement in small particles this propagation is not possible. The localized surface plasmon resonance (LSPR) occurs, when the frequency of the exciting electromagnetic field is coherent with the free charge carrier eigenfrequency in the particle and couples resonantly with the oscillation.⁹

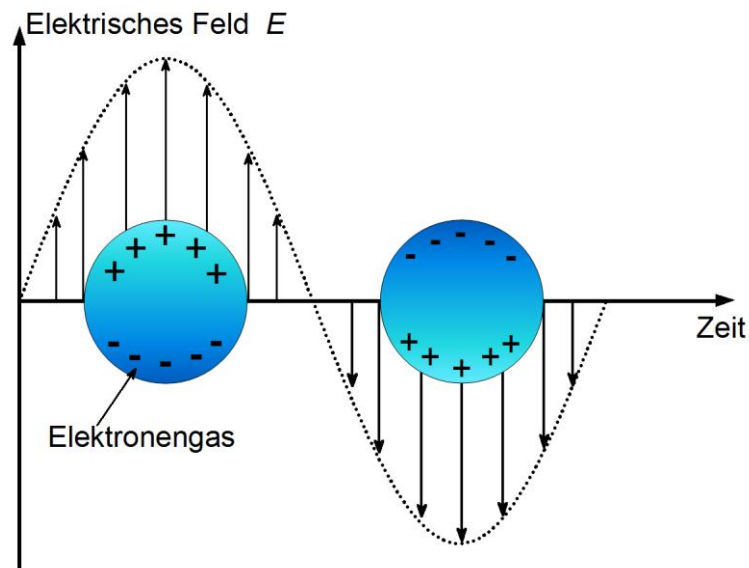


Figure 1: Schematic drawing of a metal nanoparticle in a harmonically oscillating electric field. The charge carriers follow the external excitation, resulting in an oscillation of the surface charge carrier density.

If a small (with respect to the wavelength of the light) conductive nanoparticle is illuminated by the electromagnetic wave of the light, the electrons move with the oscillation of the exciting field while the positive core ions are immobile. This changes the charge carrier density at the surface of the nanoparticle. Hence, it creates an electric dipole that scatters light.

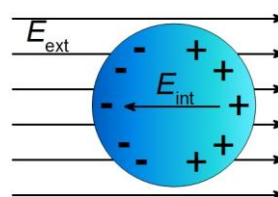


Figure 2: Schematic picture of the quasi-static approximation, a small metal nanoparticle ($2R \ll \lambda$) is placed in an external electric field (E_{ext}). Due to its comparable small size the field is assumed to be spatially homogeneous within the whole particle volume.

An approach for a simplification of this complex matter is the so-called quasi-static approximation. It can be applied for the interaction of a particle which size is much smaller than the wavelength of the exciting light ($2R \ll \lambda$). Under this boundary condition, the oscillating field can be assumed to be spatially constant within the whole

volume of the nanoparticle, and charge carriers to react in coherence. Because of this retardation effects can be neglected.^{8,9}

To understand the optical response of a homogeneous, isotropic spherical nanoparticle (radius R), the field distribution needs to be described. For this purpose the Laplace's equation (Eq. 8), with Φ denoting the electric potential is solved as follows:

$$\nabla^2 \Phi = 0. \quad 8$$

The relation of the potential Φ to the electric field E is given by:

$$E = -\nabla \Phi. \quad 9$$

The field lines of the electrical field that is surrounding the sphere are parallel in z direction in sufficient distance to the particle. The surrounding medium possesses the dielectric constant ε_m and is further non-absorbing and isotropic.⁹ Within these boundary conditions the internal electrical field E_{in} results to:⁸

$$E_{in} = \frac{3\varepsilon_m}{\varepsilon(\omega) + 2\varepsilon_m} E_0. \quad 10$$

$\varepsilon(\omega)$ is denoting the dielectric function of the sphere material. *Via* the dipole moment p , caused through the electron displacement by the exciting field E_0 , the polarizability α of the sphere can be received:⁸

$$p = \varepsilon_m \alpha E_0, \quad 11$$

$$\alpha = 4\pi\varepsilon_0 R^3 \frac{\varepsilon(\omega) - \varepsilon_m}{\varepsilon(\omega) + 2\varepsilon_m}. \quad 12$$

It can be seen in Eq. 10 and Eq. 12 that the internal electrical field E_{in} and the polarizability α , respectively, become resonant when $|\varepsilon(\omega) + 2\varepsilon_m|$ is reaching a minimum. Furthermore, it is apparent that the plasmonic properties (*via* the polarizability α), of the sphere are depending on the material through the dielectric function $\varepsilon(\omega)$, its radius R , and the surrounding medium through its dielectric constant ε_m . For non-spherical shapes the polarizability may vary for different spatial directions, resulting in an optical response that is shape dependent within the boundaries of the quasi-static approximation.⁹⁷ If the imaginary part $\varepsilon_2(\omega) \ll 1$ is very small, or very little frequency dependent the resonant condition simplifies to the Fröhlich condition:^{8,10}

$$\varepsilon_1 = -2\varepsilon_m . \quad 13$$

The polarized charges at the surface of the particle, caused from the displacement of the charge carriers in the electric field, lead to Coulomb restoring forces. When Eq. 13 is satisfied, a collective oscillation of the charge carrier arises (relative to the nuclei) at the frequency ω_{LSPR} , the so called localized surface plasmon resonance (LSPR). It can be calculated when Eq. 6 is combined with Eq.13:^{8,32}

$$\omega_{LSPR} = \sqrt{\frac{\omega_p^2}{1 + 2\varepsilon_m} - \gamma^2} . \quad 14$$

Inserting Eq. 5 for the bulk plasma frequency results in:

$$\omega_{LSPR} = \sqrt{\frac{Ne^2}{\varepsilon_0 m_{eff}(1 + 2\varepsilon_m)} - \gamma^2} . \quad 15$$

For a small damping constant γ with respect to the bulk plasma frequency ω_p ($\gamma \ll \omega_p$) Eq.14 simplifies to:

$$\omega_{LSPR} = \sqrt{\frac{Ne^2}{\varepsilon_0 m_{eff}(1 + 2\varepsilon_m)}} , \quad 16$$

$$\omega_{LSPR} = \frac{\omega_p}{\sqrt{1 + 2\varepsilon_m}} . \quad 17$$

The phenomenological damping constant is represented as the spectral linewidth of the LSPR band.^{84,98}

Naturally Eq. 16 can be converted to the LSPR wavelength λ_{LSPR} :

$$\lambda_{LSPR} = \frac{2\pi c}{\omega_{LSPR}} = \sqrt{\frac{4\pi^2 c^2 \varepsilon_0 m_{eff}(1 + 2\varepsilon_m)}{Ne^2}} , \quad 18$$

It is apparent that within the quasi static approximations the particle size does not influence the position of the LSPR, and that the frequency is lower than the bulk plasma frequency ω_p . As evident in Eq. 10 and Eq. 12, an unlimited increase of the inner field E_{in} and the polarizability α are not possible due to the imaginary part of the dielectric function $\varepsilon_2(\omega)$.⁹ As a consequence of the enhanced polarizability, the absorption and scattering intensity are enhanced at the resonance wavelength, when the

denominator $|\varepsilon(\omega) + 2\varepsilon_m|$ is passing through a minimum. The wavenumber is denoted with $= \frac{2\pi}{\lambda}$.

$$\sigma_{sca} = \frac{k^4}{6\pi\varepsilon_0^2} |\alpha|^2 = \frac{8\pi}{3} k^4 R^6 \left| \frac{\varepsilon(\omega) - \varepsilon_m}{\varepsilon(\omega) + 2\varepsilon_m} \right|^2, \quad 19$$

$$\sigma_{abs} = \frac{k}{\varepsilon_0} \text{Im}(\alpha) = 4\pi k R^3 \text{Im} \left[\frac{\varepsilon(\omega) - \varepsilon_m}{\varepsilon(\omega) + 2\varepsilon_m} \right]. \quad 20$$

For a sphere the extinction cross section (σ_{ext}) is the sum of the absorption (σ_{abs}) and the scattering cross section (σ_{sca}):⁹

$$\sigma_{ext} = \sigma_{sca} + \sigma_{abs} \quad 21$$

In summary, the surrounding medium (ε_m) has a strong influence on the resonance frequency as it is apparent in Eq. 14. As an increase of the dielectric constant of the surrounding ε_m causes a bathochromic shift of the resonance frequency (lower frequency ω_{LSPR} and longer wavelength λ_{LSPR}). It further influences the absorption, and scattering cross-section. Furthermore, the LSPR depends on the material itself through the charge carrier density (which is related to the doping degree for semiconductors), its dielectric function, lattice structure, etc. Within the boundaries of the quasi-static approximation, the position of the localized surface plasmon resonance frequency of a metallic sphere is independent of its size. However, the intensity of absorption is dependent on the particle radius to the power of three, and the scattering intensity by the radius to the power of six. Hence, the extinction of smaller particles is dominated by their absorption and for larger particles by their scattering. As an example, the change from absorption to scattering dominated gold NP occurs at a size of roughly 20 nm (in a medium with $n=1.52$). The consequence is that smaller Au NPs are primarily absorbing green light, while larger NPs are predominantly scattering green light and appear in a red color or a green color respectively.^{97,99} For larger particles the quasi-static approximation is not valid, as the electrical field can no longer be assumed to be constant within the whole volume of the plasmonic particle. As consequence of this inhomogeneity retardation effects have to be accounted for.

Experiments on plasmonic particles observed that the LSPR band broadens and bathochromically shifts with decreasing size when the particles are smaller than the mean free path of the charge carrier. The deviation from the damping constant γ of the

free Drude electron gas was attributed to surface scattering effects of the free charge carriers. Following this, the above introduced damping constant is expanded by a size depend term:^{23,100}

$$\gamma(R) = \gamma + \frac{v_F}{R} \quad 22$$

1.3.3 Mie Theory

In larger sized particles retardation effects, as well as higher mode resonances are present. Hence, the quasi-static approximation can no longer be applied. In 1908 Gustav Mie developed a theory to understand the extinction and scattering of colloids *via* an electrodynamic approach. He solved Maxwells equation in order to obtain a description of the absorption and scattering properties of gold particles suspended in water. For this purpose he defined boundary conditions (*e.g.* the confinement of the electron density within the radius R of the particle) and used multipole conditions for the exciting electromagnetic field. This complex mathematical approach became later known as Mie theory.^{8,9,101}

Mie calculated the optical response starting from the particle size, and the phenomenological optical functions of the particle material and its surrounding material.⁸ By applying the phenomenological dielectric function $\varepsilon(\omega, R)$, he accounted for deviations with respect to the bulk dielectric function. The extinction and scattering cross sections are given by:

$$\sigma_{ext} = \frac{2\pi}{|k|^2} \sum_{L=1}^{\infty} (2L+1) \text{Re}\{a_L + b_L\}, \quad 23$$

$$\sigma_{sca} = \frac{2\pi}{|k|^2} \sum_{L=1}^{\infty} (2L+1) (|a_L|^2 + |b_L|^2). \quad 24$$

a_L and b_L denoting the scattering coefficient, x the size parameter ($x = |k|R$) and n the complex index of refraction of the particle material, and n_m the real index of refraction of the surrounding medium. $\psi_L(z)$, and $\eta'_L(z)$ being the Riccati-Bessel functions.^{8,10}

$$a_L = \frac{\left[\frac{n}{n_m}\right] \psi_L\left(\left[\frac{n}{n_m}\right]x\right) \psi'_L(x) - \psi'_L\left(\left[\frac{n}{n_m}\right]x\right) \psi_L(x)}{\left[\frac{n}{n_m}\right] \psi_L\left(\left[\frac{n}{n_m}\right]x\right) \eta'_L(x) - \psi'_L\left(\left[\frac{n}{n_m}\right]x\right) \eta_L(x)}, \quad 25$$

$$b_L = \frac{\psi_L \left(\left[\frac{n}{n_m} \right] x \right) \psi'_L(x) - \left[\frac{n}{n_m} \right] \psi'_L \left(\left[\frac{n}{n_m} \right] x \right) \psi_L(x)}{\psi_L \left(\left[\frac{n}{n_m} \right] x \right) \eta'_L(x) - \left[\frac{n}{n_m} \right] \psi'_L \left(\left[\frac{n}{n_m} \right] x \right) \eta_L(x)}. \quad 26$$

With L , the summation index, the order of the spherical multipole in the particle extension is given. Hence, it gives the electric and magnetic dipole ($L=1$), quadrupole ($L=2$), octupole ($L=3$), etc.⁸

It is important to mention that the particles analyzed in this thesis are small enough, that an analysis *via* the quasi-static approximation gives relative exact result and no Mie theory is applied.

1.4 Plasmonic Semiconductor Nanoparticles

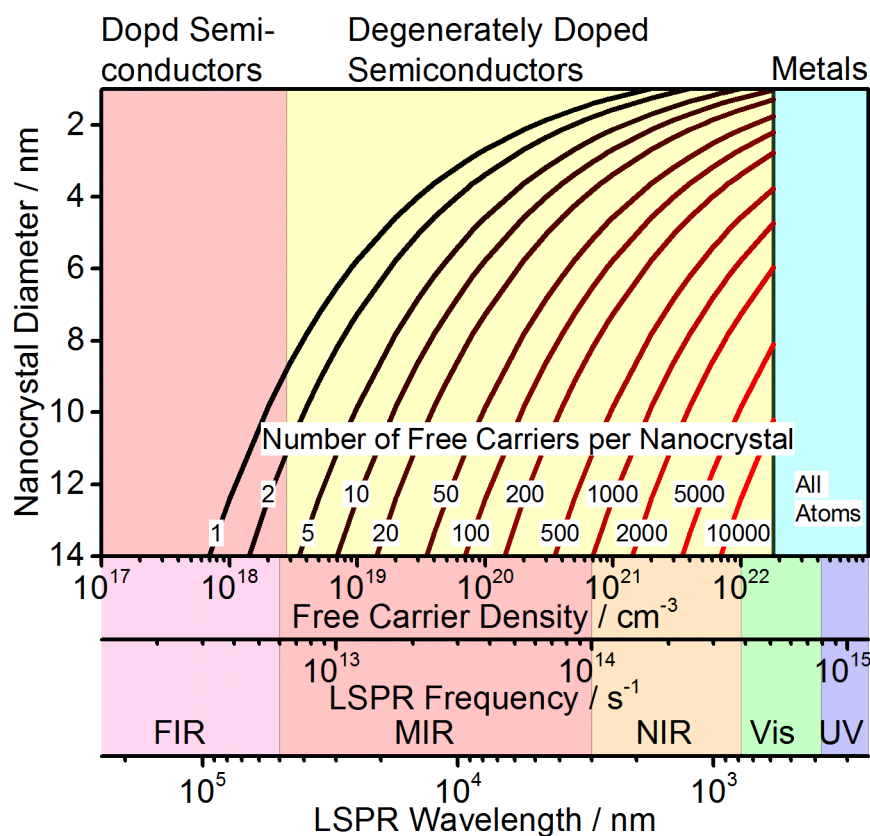


Figure 3: The diagram illustrates the dependence of the LSPR frequency (and wavelength) on the charge carrier density, and the consequential number of free charge carriers per single NC depending on its size. The LSPR wavelength was calculated applying Eq 18. m_{eff} is assumed to be that of a free electron, and toluene is used as medium with $\epsilon_m=2.25$. (Figure adapted by author from reference ²³)

The resonant interaction of the free charge carriers with the electromagnetic field of the exciting light has been observed and studied meticulously for noble metal NPs in the last decades. In particular, the LSPRs of Au NPs, but also from Ag and Cu NPs have been investigated. Due to large charge carrier densities of 10^{22} - 10^{23} cm^{-3} their LSPRs are in the UV/Vis spectral range. While it can be tuned during synthesis by defining material composition, size and shape, changes thereafter are only possible in a very limited magnitude by variations of the dielectric environment. In contrast, semiconductor carrier densities, and thus their LSPR, can be controlled *via* their

doping concentration. With self-doping (*e.g.* Cu_{2-x}Se , Cu_{2-x}S , Cu_{2-x}Te), impurity doping (*e.g.* ITO and Al doped ZnO (AZO)), and structural oxygen- deficiencies (*e.g.* WO_{3-x} , MoO_{3-x}) their charge carrier density can be raised to up to 10^{21} cm^{-3} .^{23-25,31,102-104} For degenerately doped semiconductor NPs, this results in optical properties that correspond rather to a metal than a semiconductor (outside the range of the band gap).^{23-25,56} The compared to noble metals lower charge carrier density, results in a LSPR in the NIR or MIR also for NPs smaller than 15 nm (see Figure 3 for charge carrier density dependence of the LSPR frequency) . The, especially for biological applications, interesting region of 1000 - 1350 nm, can otherwise only be achieved with Au structures larger than 50 nm in at least one dimension.²⁰⁻²² Doped semiconductors further behold the advantage that NP size and number of charge carriers per NP can be controlled independently. For classical extrinsically doped semiconductors, the concentration of charge carriers is defined by the amount of impurities, generally fixed during synthesis. On the other hand, copper chalcogenides (Cu_{2-x}Se , Cu_{2-x}Te and Cu_{2-x}S) allow as self-doped materials the simple post-synthesize charge carrier tuning due to redox reactions. While the stoichiometric compound ($x=0$) has no free charge carriers and behaves like a perfect semiconductor, the charge carrier density is created due to copper vacancies upon oxidation. The resulting material is (depending on x) strongly p-type doped.^{23,24,94} Binary copper chalcogenides have been studied for a diverse range of applications, such as photothermal therapy, bio-imaging, bio-sensing, photo-catalysis, and photovoltaics.^{34,35,40,105-107} Furthermore, they have been used as starting point for cation exchange reactions leading to ternary Cu-In-S and quaternary Cu-In-Zn-S compounds, that are highly promising materials in photovoltaics and lightning.^{27,86}

The LSPR of berzelianite NPs can only be measured after oxidation. This is the case, because the synthesized stoichiometric Cu_2Se cubic berzelianite is an intrinsic semiconductor, whose valence band is completely filled. The origin of the valence band for the lower regions is mostly based on the Se^{2-} 4s orbitals, the bands above have a mainly hybridized and 3d character from the Cu^+ . The top of the valence band arise from the Se^{2-} 4p bands. The conduction band is originating in the 4s and 4p orbitals of Cu^+ .¹⁰⁸ Approximately each chalcogen atom contributes with six 4p electrons and each Cu atom with one 4s electron to the bonding.³¹ Hence, the removal of a copper atom results in the formation of hole in the valence band. As the top of the

valence band has mainly contributions from the chalcogen, this will mostly affect the chalcogen valency.³¹ The XPS study on copper chalcogenides have shown, that during oxidation the Cu^+ state does not change within the crystal structure, but rather the valence of the chalcogen is increased starting from -2.^{56,109} The formation of the corresponding Se-Se bindings was furthermore shown by the presence of the corresponding vibrational mode for sub-stoichiometric samples in Raman analysis.⁹⁵ However, earlier studies have also shown the occurrence of Cu^{2+} in XPS studies, and additionally detected the formation of a copper oxide layer.¹¹⁰ The two observations can be brought into accordance with each other by assuming that within the Cu_{2-x}Se crystal structure, only Cu^+ is present and Se-Se formation compensates the copper deficiency. In contrast, the expelled copper atoms form CuO , either as a surface layer^{94,110} or small homogeneous nucleated CuO nanoparticles,²⁴ which cause the Cu^{2+} XPS signal. The cubic berzelianite crystal structure of Cu_{2-x}Se NPs does not change significantly during the incorporation of the vacancies (for $x \leq 0.2$), resulting in a relatively unperturbed band structure with incorporated vacancies in the valence band.^{24,108}

In the case of the $\text{Cu}_{1.1}\text{S}$ covellite nanoplatelets, reported by Xi *et al.*, a strong LSPR can be already measured for the as synthesized sample before exposure to air. The origin of the free holes in case of this material, are lattice constitutional free holes of the stoichiometric compound, resulting in its strong p-type metallic character.^{56,111} Stoichiometric covellite CuS is composed of triangular CuS_3 units between two layers built up from CuS_4 tetrahedra. This triple layer is connected to its preceding and its subsequent triple layer by disulfide bonds.⁵⁶ Despite the fact that the structure is still under debate, recent studies suggest that copper is only present in monovalent state, and the valence of sulfur equals (-1). However, some studies suggest that all sulfur atoms have a valency of (-1) ($(\text{Cu}^{1+})_3(\text{S}_2^{2-})(\text{S}^{1-})$)¹¹², whereas others suggest only the average is (-1) ($(\text{Cu}^{1+})_3(\text{S}_2^-)(\text{S}^{2-})$)^{113,56}. The addition of Cu^+ ions to covellite nanoplatelets leads to an increase of the copper to sulfur ratio up to 2:1, accompanied by the structural change to a metastable phase and subsequently to (a mixture) of the anilite (Cu_{2-x}S), and finally chalcocite (Cu_2S) phase. Following the increase of the copper content, the disulfide bonds are broken, and the concentration of free holes reduced. The later can be well observed due to the conjunct reduction and bathochromic shift of the LSPR band.⁵⁶

The low number of only a few hundreds of charge carriers per NP (for example around 400 per 9.2 nm Cu_{2-x}Se NP) results also in a (compared to noble metal NPs) larger response due to the addition or removal of only a few electrons for instance achieved by redox reactions or attachment of electron donating or trapping ligands.^{114,115} To illustrate the theoretical sensitivity of such a process: for a 3 nm NP the addition of a single charge carrier equals the increase of the carrier concentration by 10²⁰ cm⁻³. This corresponds to a LSPR shift of roughly 100 nm.¹¹⁶

A further consequence of the increasing doping, for example in degenerately doped Cu_{2-x}Se NPs, is the rise of the observed band gap. It can be measured as a shift to higher energies of the band edge in the absorption spectrum. This so called Burstein-Moss effect is caused because of the increase of copper vacancies, and the consequential reduction of electrons in the top of the valence band. The reduction causes a shift of the Fermi level to lower energies, until it moves below the top of the valence band - this condition is called degenerate. In order to be excited from the highest occupied level to the conduction band, electrons need not only the energy corresponding to the actual band gap, but also the energy of the Burstein-Moss-shift. Consequently, a larger observed band gap is measured.^{117,118} Moreover, in the degenerate state the discrete (for low amount of doping) acceptor levels merge to a continuous band. At some point this band overlaps with the valence band, resulting in the ability to conduct current at T=0 K, as metals do.^{119,120}

Several recent works have shown that the LSPRs of copper chalcogenides behave relatively similar to their metallic counterpart. Just as metals¹²¹ their LSPR broadens and bathochromically shifts for very small particles, and is completely damped for NPs smaller than 3 nm, because of an increase in surface scattering events.^{23,28} Furthermore, the bathochromic shift of the maximum position of the semiconductor LSPR upon the increase of the refractive index was studied by several groups.^{23,25,103,122} This opens the possibility for dielectric environment based sensing in the NIR. A further effect on the metal LSPR is achieved by shape control.⁹⁸ Comparable LSPR modifications have been observed for copper chalcogenide rods, platelets and sheets.^{41,54,76,94,123,124} Even so, some works found a lower than expected dependence of the LSPR on the shape in copper chalcogenides, which was assigned to a partial localization of the free charge carriers.^{93,94} Plasmon coupling occurs when metal NPs are in close proximity to each other, resulting a bathochromic shift of their

LSPR (when parallel to the interparticle axis).^{12,125} The same effect was also observed by Kriegel *et al.* upon the aggregation of plasmonic Cu_{1.97}S particles.³⁰

While copper chalcogenides are one of the most fiercely studied plasmonic material groups in the recent years, and within this thesis, other degenerately doped semiconductors are also under continuous investigation. Different doped tin oxides for example; especially ITO, which is widely used as thin film in transparent electrodes, because of its high conductivity, and high transparency in the visible region. Whereas most of these metal oxides cannot be tuned post synthetically (by reduction or oxidation), their charge carrier concentration can be defined during synthesis independently of size, for instance by defining the tin concentration in ITO NPs.^{25,126} Further examples are the aluminum or gallium doped ZnO, antimony-doped tin oxide, indium cadmium oxide, but also several oxygen deficient metal oxides, such as tungsten oxide (WO_{3-x}) or molybdenum oxide.^{31,127}

1.5 Metal Organic Framework Composites

1.5.1 Metal Organic Frameworks

Metal organic frameworks (MOFs) are crystalline structures composed of organic linkers that are connected *via* metal ions. The metal ions strongly bind with the organic molecules forming secondary building units (SBUs), which then connect with each other to form 3D-frameworks. The resulting structures are highly porous and exhibit an open crystalline framework. Due to their modular nature a vast amount of more than 20 000 different MOFs with a broad range of functionalities have been reported over the last decades. The achieved materials can exhibit enormous internal surface areas of 1 000 to 10 000 m²/g and possess a permanent porosity.^{128,129}

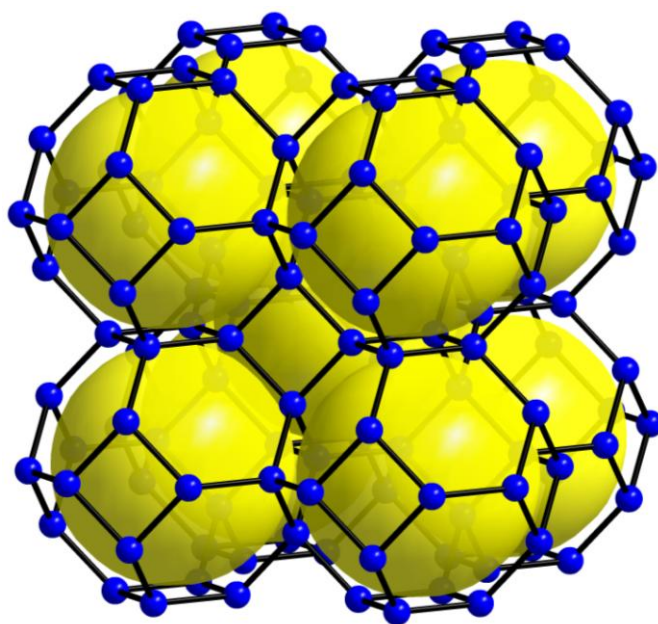


Figure 4: Schematic of the sodalite framework of the cubic ZIF-8, formed by the linker molecule 2-methylimidazole (black sticks) and the tetrahedrally coordinated metal ion: Zn²⁺ ions (blue balls). The yellow spheres represent the cavities of the framework.

A fascinating subgroup of the MOFs is the zeolitic imidazole frameworks (ZIFs). They are characterized by their structural resemblance to zeolites. This originates from the roughly 145° angle of the metal ion-imidazolate-metal ion binding, which is similar to the Si-O-Si bonding angle in zeolites. Due to variation of the metal ion

(Zn^{2+} , Co^{2+} , Cu^{2+} and Fe^{2+}) and the imidazole ligand various ZIF structures have been fabricated in recent years. One of the most predominate ones being the ZIF-8, with the SBU $\text{Zn}(\text{mim})_2$ (mim= 2-methylimidazolate). It shows an outstanding chemical stability to boiling alkaline water and organic solvents as well as high thermal stability up to 550 °C.^{128,130-132} In the ZIF-8 structure one Zn^{2+} ion is always coordinated to four 2-methylimidazolates, forming a cubic sodalite topology (see

Figure 4). Spherical cavities with a diameter of 11.6 Å are formed out of eight six-membered rings and six four-membered rings.¹³⁰ The pores formed by the connection of the six-membered ring exhibit a diameter of 3.4 Å. Furthermore, recent articles showed that due to a gate opening effect also large molecules can jump between cavities.^{130,133} The ZIF-8 structure possesses a surface area of 1947 m²/g.

The high surface areas and defined regular structures fuelled the research for multiple possible applications of MOFs and specifically ZIFs. Particularly, gas storage, gas separation, catalysis as well as sensing are under investigation during the last years.^{128,129,131,132,134,135}

1.5.2 NP@MOF-Composites

In order to enhance the functionalities and properties of MOFs, one approach is the post synthetic modification. Typical approaches are covalent linker modification, covalent SBU modification, as well as linker exchange and transmetalation of the metal based framework nodes.¹³⁶⁻¹⁴⁰ However, a different way that is opening a completely new range of possibilities, is the functionalization of MOFs by incorporating nanoparticles.¹⁴¹⁻¹⁴⁸

The preparation of MOFs with novel properties due to the incorporation of NPs can be grouped into two different routes. The “ship-in-a-bottle” approach, for this one the precursor molecules are immobilized inside the preformed MOF, and are treated in situ to transform to the desired NP. The precursors can be brought into the pores of the MOF by chemical vapor infiltration or by solution impregnation, and are reacted due to reducing agents, heat or radiation in a second step. As the cavities of the MOF are acting as templates, the resulting NPs are generally very small. Even so, this approach is possibly well scalable the “ship-in-a-bottle” method lacks shape and composition control, which can be essential especially for catalytic or sensing applications. The alternative is the “bottle around the ship” approach, where preformed NPs are

encapsulated by the growing MOF. It allows for a full control of NP size, shape, composition (as far as the appropriate synthesis protocols exist), and the positioning inside the framework. A blocking of the pores is avoided (the MOF is growing around the nanoparticles), as well as deposition of the nanoparticles on the surface of the MOF.^{143,144,146-149} Until today, several publications have reported the synthesis of multiple semiconductor NP@MOF (*e.g.* CdS@MIL-101, CdSe/CdS/ZnS@MOF-5, ZnO@ZIF-8, ZnO@MOF-5,...)¹⁴⁸ and of metal NP@MOF composites (*e.g.* Au@MOF-5, Au@ZIF-8, Ag@ZIF-8, Pt@ZIF-8,...).^{141,147} The plasmonic properties of metal NPs embedded in MOFs have been used for example in sensing applications (*e.g.* Au nanorods@MOF-5 composites for size selective surface enhanced Raman scattering sensing).^{145,150} Our report of the fabrication of Cu_{2-x}Se@ZIF-8 and ITO@ZIF-8 composites, however, described for the first time the combination of the versatility of plasmonic semiconductor NPs, with the permanent porosity of MOFs. The access through the pores, allows the development of the LSPR from Cu_{2-x}Se@ZIF-8 composites through oxidation. Furthermore, the ZIF-8 gates are large enough for Hg²⁺ and Ag⁺ ions to diffuse into the structure, enabling an in situ cation exchange to a HgSe@ZIF-8 and Ag₂Se@ZIF-8 composites as will be shown in chapter 4.

1.6 References

1. Goesmann, H.; Feldmann, C. Nanoparticulate Functional Materials. *Angewandte Chemie International Edition* **2010**, *49*, 1362-1395.
2. Xu, G.; Zeng, S.; Zhang, B.; Swihart, M. T.; Yong, K.; Prasad, P. N. New Generation Cadmium-Free Quantum Dots for Biophotonics and Nanomedicine. *Chem. Rev.* **2016**.
3. Kovalenko, M. V.; Manna, L.; Cabot, A.; Hens, Z.; Talapin, D. V.; Kagan, C. R.; Klimov, V. I.; Rogach, A. L.; Reiss, P.; Milliron, D. J.; Guyot-Sionnest, P.; Konstantatos, G.; Parak, W. J.; Hyeon, T.; Korgel, B. A.; Murray, C. B.; Heiss, W. Prospects of Nanoscience with Nanocrystals. *ACS Nano* **2015**, *9*, 1012-1057.
4. Spanhel, L.; Haase, M.; Weller, H.; Henglein, A. Photochemistry of Colloidal Semiconductors. 20. Surface Modification and Stability of Strong Luminescing CdS Particles. *J. Am. Chem. Soc.* **1987**, *109*, 5649-5655.
5. Henglein, A. Small-Particle Research: Physicochemical Properties of Extremely Small Colloidal Metal and Semiconductor Particles. *Chem. Rev.* **1989**, *89*, 1861-73.
6. Weller, H. Colloidal Semiconductor Q-Particles: Chemistry in the Transition Region Between Solid State and Molecules. *Angewandte Chemie International Edition in English* **1993**, *32*, 41-53.
7. Talapin, D. V.; Lee, J.; Kovalenko, M. V.; Shevchenko, E. V. Prospects of Colloidal Nanocrystals for Electronic and Optoelectronic Applications. *Chem. Rev.* **2010**, *110*, 389-458.
8. Kreibig, U.; Vollmer, M. *Optical Properties of Metal Clusters*; Springer Series in Materials Science; Springer-Verlag: Berlin Heidelberg, 1995; Vol. 25, pp 535.
9. Maier, S. A. *Plasmonics: Fundamentals and Applications*; Springer US: Boston, MA ;, 2007; , pp 223.
10. Bohren, C. F.; Huffman, D. R. *Absorption and Scattering of Light by Small Particles*; Wiley-Interscience Publication: New York [u.a.], 1983; , pp 530.
11. Link, S.; El-Sayed, M. Optical Properties and Ultrafast Dynamics of Metallic Nanocrystals. *Annu. Rev. Phys. Chem.* **2003**, *54*, 331-366.
12. Halas, N. J.; Lal, S.; Chang, W. S.; Link, S.; Nordlander, P. Plasmons in Strongly Coupled Metallic Nanostructures. *Chem. Rev.* **2011**, *111*, 3913-3961.
13. Stewart, M. E.; Anderton, C. R.; Thompson, L. B.; Maria, J.; Gray, S. K.; Rogers, J. A.; Nuzzo, R. G. Nanostructured Plasmonic Sensors. *Chem. Rev.* **2008**, *108*, 494-521.

14. Sau, T. K.; Rogach, A. L.; Jaeckel, F.; Klar, T. A.; Feldmann, J. Properties and Applications of Colloidal Nonspherical Noble Metal Nanoparticles. *Adv. Mater.* **2010**, *22*, 1805-1825.
15. Sepulveda, B.; Angelome, P. C.; Lechuga, L. M.; Liz-Marzan, L. LSPR-Based Nanobiosensors. *Nano Today* **2009**, *4*, 244-251.
16. Rosi, N. L.; Mirkin, C. A. Nanostructures in Biodiagnostics. *Chem. Rev.* **2005**, *105*, 1547-1562.
17. Jain, P. K.; Huang, X.; El-Sayed, I.; El-Sayed, M. Noble Metals on the Nanoscale: Optical and Photothermal Properties and Some Applications in Imaging, Sensing, Biology, and Medicine. *Acc. Chem. Res.* **2008**, *41*, 1578-1586.
18. Graham, E. G.; MacNeill, C. M.; Levi-Polyachenko, N. Review of Metal, Carbon and Polymer Nanoparticles for Infrared Photothermal Therapy. *Nano LIFE* **2013**, *3*, 1330002/1-1330002/29.
19. Chen, G.; Seo, J.; Yang, C.; Prasad, P. N. Nanochemistry and Nanomaterials for Photovoltaics. *Chem. Soc. Rev.* **2013**, *42*, 8304-8338.
20. Link, S.; El-Sayed, M. Size and Temperature Dependence of the Plasmon Absorption of Colloidal Gold Nanoparticles. *J Phys Chem B* **1999**, *103*, 4212-4217.
21. Murphy, C. J.; Sau, T. K.; Gole, A. M.; Orendorff, C. J.; Gao, J.; Gou, L.; Hunyadi, S. E.; Li, T. Anisotropic Metal Nanoparticles: Synthesis, Assembly, and Optical Applications. *J. Phys. Chem. B* **2005**, *109*, 13857-13870.
22. Bashkatov, A. N.; Genina, E. A.; Kochubey, V. I.; Tuchin, V. V. Optical Properties of Human Skin, Subcutaneous and Mucous Tissues in the Wavelength Range From 400 to 2000 nm. *J. Phys. D: Appl. Phys.* **2005**, *38*, 2543-2555.
23. Luther, J. M.; Jain, P. K.; Ewers, T.; Alivisatos, A. P. Localized Surface Plasmon Resonances Arising from Free Carriers in Doped Quantum Dots. *Nat Mater* **2011**, *10*, 361-366.
24. Dorfs, D.; Härtling, T.; Miszta, K.; Bigall, N. C.; Kim, M. R.; Genovese, A.; Falqui, A.; Povia, M.; Manna, L. Reversible Tunability of the Near-Infrared Valence Band Plasmon Resonance in Cu_{2-x}Se Nanocrystals. *J. Am. Chem. Soc.* **2011**, *133*, 11175-11180.
25. Kanehara, M.; Koike, H.; Yoshinaga, T.; Teranishi, T. Indium Tin Oxide Nanoparticles with Compositionally Tunable Surface Plasmon Resonance Frequencies in the Near-IR Region. *J. Am. Chem. Soc.* **2009**, *131*, 17736-17737.
26. Zhao, Y.; Burda, C. Development of Plasmonic Semiconductor Nanomaterials with Copper Chalcogenides for a Future with Sustainable Energy Materials. *Energy Environ. Sci.* **2012**, *5*, 5564-5576.

27. van der Stam, W.; Berends, A. C.; Donega, C. d. M. Prospects of Colloidal Copper Chalcogenide Nanocrystals. *ChemPhysChem* **2016**, *17*, 559-581.
28. Kriegel, I.; Jiang, C.; Rodriguez-Fernandez, J.; Schaller, R. D.; Talapin, D. V.; da, C., Enrico; Feldmann, J. Tuning the Excitonic and Plasmonic Properties of Copper Chalcogenide Nanocrystals. *J. Am. Chem. Soc.* **2012**, *134*, 1583-1590.
29. Zhao, Y.; Pan, H.; Lou, Y.; Qiu, X.; Zhu, J.; Burda, C. Plasmonic Cu_{2-x}S Nanocrystals: Optical and Structural Properties of Copper-Deficient Copper(I) Sulfides. *J. Am. Chem. Soc.* **2009**, *131*, 4253-4261.
30. Kriegel, I.; Rodriguez-Fernandez, J.; Da, C., Enrico; Lutich, A. A.; Szeifert, J. M.; Feldmann, J. Tuning the Light Absorption of Cu_{1.97}S Nanocrystals in Supercrystal Structures. *Chem. Mater.* **2011**, *23*, 1830-1834.
31. Comin, A.; Manna, L. New Materials for Tunable Plasmonic Colloidal Nanocrystals. *Chem. Soc. Rev.* **2014**, *43*, 3957-3975.
32. Routzahn, A. L.; White, S. L.; Fong, L.; Jain, P. K. Plasmonics with Doped Quantum Dots. *Isr. J. Chem.* **2012**, *52*, 983-991.
33. Scotognella, F.; Della, V., Giuseppe; Srimath, K., Ajay Ram; Dorfs, D.; Zavelani-Rossi, M.; Conforti, M.; Miszta, K.; Comin, A.; Korobchevskaya, K.; Lanzani, G.; Manna, L.; Tassone, F. Plasmon Dynamics in Colloidal Cu_{2-x}Se Nanocrystals. *Nano Lett.* **2011**, *11*, 4711-4717.
34. Hessel, C. M.; Pattani, V. P.; Rasch, M.; Panthani, M. G.; Koo, B.; Tunnell, J. W.; Korgel, B. A. Copper Selenide Nanocrystals for Photothermal Therapy. *Nano Lett.* **2011**, *11*, 2560-2566.
35. Liu, Z.; Liu, X.; Du, Y.; Ren, J.; Qu, X. Using Plasmonic Copper Sulfide Nanocrystals as Smart Light-Driven Sterilants. *ACS Nano* **2015**, *9*, 10335-10346.
36. Demortiere, A.; Schaller, R. D.; Li, T.; Chattopadhyay, S.; Krylova, G.; Shibata, T.; dos, S. C.; Rowland, C. E.; Miller, J. T.; Cook, R.; Lee, B.; Shevchenko, E. V. In Situ Optical and Structural Studies on Photoluminescence Quenching in CdSe/CdS/Au Heterostructures. *J. Am. Chem. Soc.* **2014**, *136*, 2342-2350.
37. Saunders, A. E.; Popov, I.; Banin, U. Synthesis of hybrid CdS-Au colloidal nanostructures. *J Phys Chem B* **2006**, *110*, 25421-25429.
38. Menagen, G.; Mocatta, D.; Salant, A.; Popov, I.; Dorfs, D.; Banin, U. Selective Gold Growth on CdSe Seeded CdS Nanorods. *Chem. Mater.* **2008**, *20*, 6900-6902.
39. Carbone, L.; Cozzoli, P. D. Colloidal Heterostructured Nanocrystals: Synthesis and Growth Mechanisms. *Nano Today* **2010**, *5*, 449-493.
40. Liu, X.; Lee, C.; Law, W.; Zhu, D.; Liu, M.; Jeon, M.; Kim, J.; Prasad, P. N.; Kim, C.; Swihart, M. T. Au-Cu_{2-x}Se Heterodimer Nanoparticles with Broad Localized

Surface Plasmon Resonance as Contrast Agents for Deep Tissue Imaging. *Nano Lett.* **2013**, *13*, 4333-4339.

41. Muhammed, M. A. H.; Doeblinger, M.; Rodriguez-Fernandez, J. Switching Plasmons: Gold Nanorod-Copper Chalcogenide Core-Shell Nanoparticle Clusters with Selectable Metal/Semiconductor NIR Plasmon Resonances. *J. Am. Chem. Soc.* **2015**, *137*, 11666-11677.
42. Ding, X.; Liow, C. H.; Zhang, M.; Huang, R.; Li, C.; Shen, H.; Liu, M.; Zou, Y.; Gao, N.; Zhang, Z.; Li, Y.; Wang, Q.; Li, S.; Jiang, J. Surface Plasmon Resonance Enhanced Light Absorption and Photothermal Therapy in the Second Near-Infrared Window. *J. Am. Chem. Soc.* **2014**, *136*, 15684-15693.
43. Li, H.; Kanaras, A. G.; Manna, L. Colloidal Branched Semiconductor Nanocrystals: State of the Art and Perspectives. *Acc. Chem. Res.* **2013**, *46*, 1387-1396.
44. de, M. D., Celso; Liljeroth, P.; Vanmaekelbergh, D. Physicochemical Evaluation of the Hot-Injection Method, a Synthesis Route for Monodisperse Nanocrystals. *Small* **2005**, *1*, 1152-1162.
45. Park, J.; Joo, J.; Kwon, S. G.; Jang, Y.; Hyeon, T. Synthesis of Monodisperse Spherical Nanocrystals. *Angew. Chem., Int. Ed.* **2007**, *46*, 4630-4660.
46. Yin, Y.; Alivisatos, A. P. Colloidal Nanocrystal Synthesis and the Organic-Inorganic Interface. *Nature (London, U. K.)* **2005**, *437*, 664-670.
47. LaMer, V. K.; Dinegar, R. H. Theory, Production and Mechanism of Formation of Monodispersed Hydrosols. *J. Am. Chem. Soc.* **1950**, *72*, 4847-4854.
48. Murray, C. B.; Norris, D. J.; Bawendi, M. G. Synthesis and Characterization of Nearly Monodisperse CdE (E = Sulfur, Selenium, Tellurium) Semiconductor Nanocrystallites. *J. Am. Chem. Soc.* **1993**, *115*, 8706-15.
49. Kagan, C. R.; Murray, C. B. Charge Transport in Strongly Coupled Quantum Dot Solids. *Nat. Nanotechnol.* **2015**, *10*, 1013-1026.
50. Peng, X.; Manna, L.; Yang, W.; Wickham, J.; Scher, E.; Kadavanich, A.; Alivisatos, A. P. Shape Control of CdSe Nanocrystals. *Nature* **2000**, *404*, 59-61.
51. Manna, L.; Milliron, D. J.; Meisel, A.; Scher, E. C.; Alivisatos, A. P. Controlled Growth of Tetrapod-Branched Inorganic Nanocrystals. *Nat. Mater.* **2003**, *2*, 382-385.
52. Ithurria, S.; Dubertret, B. Quasi 2D Colloidal CdSe Platelets with Thicknesses Controlled at the Atomic Level. *J. Am. Chem. Soc.* **2008**, *130*, 16504-16505.
53. Deka, S.; Miszta, K.; Dorfs, D.; Genovese, A.; Bertoni, G.; Manna, L. Octapod-Shaped Colloidal Nanocrystals of Cadmium Chalcogenides via "One-Pot" Cation Exchange and Seeded Growth. *Nano Lett.* **2010**, *10*, 3770-3776.

54. Li, W.; Zamani, R.; Gil, P. R.; Pelaz, B.; Ibanez, M.; Cadavid, D.; Shavel, A.; Alvarez-Puebla, R. A.; Parak, W. J.; Arbiol, J.; Cabot, A. CuTe Nanocrystals: Shape and Size Control, Plasmonic Properties, and Use as SERS Probes and Photothermal Agents. *J. Am. Chem. Soc.* **2013**, *135*, 7098-7101.
55. Kruszynska, M.; Borchert, H.; Bachmatiuk, A.; Ruemmel, M. H.; Buechner, B.; Parisi, J.; Kolny-Olesiak, J. Size and Shape Control of Colloidal Copper(I) Sulfide Nanorods. *ACS Nano* **2012**, *6*, 5889-5896.
56. Xie, Y.; Riedinger, A.; Prato, M.; Casu, A.; Genovese, A.; Guardia, P.; Sottini, S.; Sangregorio, C.; Miszta, K.; Ghosh, S.; Pellegrino, T.; Manna, L. Copper Sulfide Nanocrystals with Tunable Composition by Reduction of Covellite Nanocrystals with Cu⁺ Ions. *J. Am. Chem. Soc.* **2013**, *135*, 17630-17637.
57. Wu, X.; Huang, X.; Liu, J.; Li, H.; Yang, J.; Li, B.; Huang, W.; Zhang, H. Two-Dimensional CuSe Nanosheets with Microscale Lateral Size: Synthesis and Template-Assisted Phase Transformation. *Angew. Chem., Int. Ed.* **2014**, *53*, 5083-5087.
58. Hoener, C. F.; Allan, K. A.; Bard, A. J.; Campion, A.; Fox, M. A.; Mallouk, T. E.; Webber, S. E.; White, J. M. Demonstration of a Shell-Core Structure in Layered Cadmium Selenide-Zinc Selenide Small Particles by x-Ray Photoelectron and Auger Spectroscopies. *J. Phys. Chem.* **1992**, *96*, 3812-17.
59. Dabbousi, B. O.; Rodriguez-Viejo, J.; Mikulec, F. V.; Heine, J. R.; Mattoussi, H.; Ober, R.; Jensen, K. F.; Bawendi, M. G. (CdSe)ZnS Core-Shell Quantum Dots: Synthesis and Optical and Structural Characterization of a Size Series of Highly Luminescent Materials. *J Phys Chem B* **1997**, *101*, 9463-9475.
60. Dorfs, D.; Franzl, T.; Osovsky, R.; Brumer, M.; Lifshitz, E.; Klar, T. A.; Eychmüller, A. Type-I and Type-II Nanoscale Heterostructures Based on CdTe Nanocrystals: A Comparative Study. *Small* **2008**, *4*, 1148-1152.
61. Hines, M. A.; Guyot-Sionnest, P. Synthesis and Characterization of Strongly Luminescing ZnS-Capped CdSe Nanocrystals. *J. Phys. Chem.* **1996**, *100*, 468-471.
62. Battaglia, D.; Li, J. J.; Wang, Y.; Peng, X. Colloidal Two-Dimensional Systems: CdSe Quantum Shells and Wells. *Angew. Chem., Int. Ed.* **2003**, *42*, 5035-5039.
63. Zimmer, J. P.; Kim, S.; Ohnishi, S.; Tanaka, E.; Frangioni, J. V.; Bawendi, M. G. Size Series of Small Indium Arsenide-Zinc Selenide Core-Shell Nanocrystals and Their Application to In Vivo Imaging. *J. Am. Chem. Soc.* **2006**, *128*, 2526-2527.
64. Kirchner, C.; Liedl, T.; Kudera, S.; Pellegrino, T.; Munoz Javier, A.; Gaub, H. E.; Stolzle, S.; Fertig, N.; Parak, W. J. Cytotoxicity of Colloidal CdSe and CdSe/ZnS Nanoparticles. *Nano Letters* **2005**, *5*, 331-338.
65. Chanana, M.; Liz-Marzan, L. Coating Matters: the Influence of Coating Materials on the Optical Properties of Gold Nanoparticles. *Nanophotonics* **2012**, *1*, 199-220.

66. Liu, D.; Ding, S.; Lin, H.; Liu, B.; Ye, Z.; Fan, F.; Ren, B.; Tian, Z. Distinctive Enhanced and Tunable Plasmon Resonant Absorption from Controllable Au@Cu₂O Nanoparticles: Experimental and Theoretical Modeling. *J. Phys. Chem. C* **2012**, *116*, 4477-4483.
67. Wolf, A.; Haertling, T.; Hinrichs, D.; Dorfs, D. Synthesis of Plasmonic Cu_{2-x}Se@ZnS Core@Shell Nanoparticles. *ChemPhysChem* **2016**, *17*, 717-723.
68. Lee, J.; Shevchenko, E. V.; Talapin, D. V. Au-PbS Core-Shell Nanocrystals: Plasmonic Absorption Enhancement and Electrical Doping via Intra-particle Charge Transfer. *J. Am. Chem. Soc.* **2008**, *130*, 9673-9675.
69. Banholzer, M. J.; Harris, N.; Millstone, J. E.; Schatz, G. C.; Mirkin, C. A. Abnormally Large Plasmonic Shifts in Silica-Protected Gold Triangular Nanoprisms. *J. Phys. Chem. C* **2010**, *114*, 7521-7526.
70. Shi, W.; Zeng, H.; Sahoo, Y.; Ohulchanskyy, T. Y.; Ding, Y.; Wang, Z. L.; Swihart, M.; Prasad, P. N. A General Approach to Binary and Ternary Hybrid Nanocrystals. *Nano Lett.* **2006**, *6*, 875-881.
71. Ghosh, C., Rajib; Paria, S. Core/Shell Nanoparticles: Classes, Properties, Synthesis Mechanisms, Characterization, and Applications. *Chem. Rev.* **2012**, *112*, 2373-2433.
72. Rivest, J. B.; Jain, P. K. Cation Exchange on the Nanoscale: an Emerging Technique for New Material Synthesis, Device Fabrication, and Chemical Sensing. *Chem. Soc. Rev.* **2013**, *42*, 89-96.
73. De Trizio, L.; Manna, L. Forging Colloidal Nanostructures via Cation Exchange Reactions. *Chem. Rev. (Washington, DC, U. S.)* **2016**, Ahead of Print.
74. Gupta, S.; Kershaw, S. V.; Rogach, A. L. 25th Anniversary Article: Ion Exchange in Colloidal Nanocrystals. *Adv. Mater. (Weinheim, Ger.)* **2013**, *25*, 6923-6944.
75. Beberwyck, B. J.; Surendranath, Y.; Alivisatos, A. P. Cation Exchange: A Versatile Tool for Nanomaterials Synthesis. *J. Phys. Chem. C* **2013**, *117*, 19759-19770.
76. Wang, Y.; Zhukovskiy, M.; Tongying, P.; Tian, Y.; Kuno, M. Synthesis of Ultrathin and Thickness-Controlled Cu_{2-x}Se Nanosheets via Cation Exchange. *J. Phys. Chem. Lett.* **2014**, *5*, 3608-3613.
77. Son, D. H.; Hughes, S. M.; Yin, Y.; Paul Alivisatos, A. Cation Exchange Reactions in Ionic Nanocrystals. *Science* **2004**, *306*, 1009-1012.
78. Eychmueller, A.; Mews, A.; Weller, H. A Quantum Dot Quantum Well: Cadmium Sulfide/Mercuric Sulfide/Cadmium Sulfide. *Chem. Phys. Lett.* **1993**, *208*, 59-62.

79. Haesselbarth, A.; Eychmueller, A.; Eichberger, R.; Giersig, M.; Mews, A.; Weller, H. Chemistry and Photophysics of Mixed Cadmium Sulfide/Mercury Sulfide Colloids. *J. Phys. Chem.* **1993**, *97*, 5333-40.
80. Zhou, H. S.; Sasahara, H.; Honma, I.; Komiyama, H.; Haus, J. W. Coated Semiconductor Nanoparticles: The CdS/PbS System's Photoluminescence Properties. *Chem. Mater.* **1994**, *6*, 1534-41.
81. Wolf, A.; Kodanek, T.; Dorfs, D. Tuning the LSPR in Copper Chalcogenide Nanoparticles by Cation Intercalation, Cation Exchange and Metal Growth. *Nanoscale* **2015**, *7*, 19519-19527.
82. Miszta, K.; Gariano, G.; Brescia, R.; Marras, S.; De Donato, F.; Ghosh, S.; De Trizio, L.; Manna, L. Selective Cation Exchange in the Core Region of $\text{Cu}_2\text{-xSe/Cu}_{2\text{-x}}\text{S}$ Core/Shell Nanocrystals. *J. Am. Chem. Soc.* **2015**, *137*, 12195-12198.
83. Han, S.; Gong, M.; Wang, Z.; Gu, C.; Yu, S. Colloidal Synthesis of $\text{Cu}_2\text{S}_x\text{Se}_{1-x}$ Hexagonal Nanoplates and Their Transformation to $\text{CdS}_x\text{Se}_{1-x}$ and $\text{ZnS}_x\text{Se}_{1-x}$ by the Cation-Exchange Reaction. *Part. Part. Syst. Charact.* **2013**, *30*, 1024-1029.
84. Xie, Y.; Bertoni, G.; Riedinger, A.; Sathya, A.; Prato, M.; Marras, S.; Tu, R.; Pellegrino, T.; Manna, L. Nanoscale Transformations in Covellite (CuS) Nanocrystals in the Presence of Divalent Metal Cations in a Mild Reducing Environment. *Chem. Mater.* **2015**, *27*, 7531-7537.
85. Luther, J. M.; Zheng, H.; Sadtler, B.; Alivisatos, A. P. Synthesis of PbS Nanorods and Other Ionic Nanocrystals of Complex Morphology by Sequential Cation Exchange Reactions. *J. Am. Chem. Soc.* **2009**, *131*, 16851-16857.
86. Akkerman, Q. A.; Genovese, A.; George, C.; Prato, M.; Moreels, I.; Casu, A.; Marras, S.; Curcio, A.; Scarpellini, A.; Pellegrino, T.; Manna, L.; Lesnyak, V. From Binary Cu_2S to Ternary Cu-In-S and Quaternary Cu-In-Zn-S Nanocrystals with Tunable Composition via Partial Cation Exchange. *ACS Nano* **2015**, *9*, 521-531.
87. Lesnyak, V.; George, C.; Genovese, A.; Prato, M.; Casu, A.; Ayyappan, S.; Scarpellini, A.; Manna, L. Alloyed Copper Chalcogenide Nanoplatelets via Partial Cation Exchange Reactions. *ACS Nano* **2014**, *8*, 8407-8418.
88. Jen-La Plante, I.; Teitelboim, A.; Pinkas, I.; Oron, D.; Mokari, T. Exciton Quenching Due to Copper Diffusion Limits the Photocatalytic Activity of CdS/ Cu_2S Nanorod Heterostructures. *J. Phys. Chem. Lett.* **2014**, *5*, 590-596.
89. Tan, C.; Hsiao, C.; Wang, S.; Liu, P.; Lu, M.; Huang, M. H.; Ouyang, H.; Chen, L. Sequential Cation Exchange Generated Superlattice Nanowires Forming Multiple p-n Heterojunctions. *ACS Nano* **2014**, *8*, 9422-9426.
90. Sadtler, B.; Demchenko, D. O.; Zheng, H.; Hughes, S. M.; Merkle, M. G.; Dahmen, U.; Wang, L.; Alivisatos, A. P. Selective Facet Reactivity during Cation

- Exchange in Cadmium Sulfide Nanorods. *J. Am. Chem. Soc.* **2009**, *131*, 5285-5293.
91. Adel, P.; Wolf, A.; Kodanek, T.; Dorfs, D. Segmented CdSe@CdS/ZnS Nanorods Synthesized via a Partial Ion Exchange Sequence. *Chem. Mater.* **2014**, *26*, 3121-3127.
92. Li, H.; Brescia, R.; Krahne, R.; Bertoni, G.; Alcocer, M. J. P.; D'Andrea, C.; Scotognella, F.; Tassone, F.; Zanella, M.; De, G., Milena; Manna, L. Blue-UV-Emitting ZnSe(Dot)/ZnS(Rod) Core/Shell Nanocrystals Prepared from CdSe/CdS Nanocrystals by Sequential Cation Exchange. *ACS Nano* **2012**, *6*, 1637-1647.
93. Kriegel, I.; Wisnet, A.; Srimath Kandada, A. R.; Scotognella, F.; Tassone, F.; Scheu, C.; Zhang, H.; Govorov, A. O.; Rodriguez-Fernandez, J.; Feldmann, J. Cation Exchange Synthesis and Optoelectronic Properties of Type II CdTe-Cu_{2-x}Te Nano-Heterostructures. *J. Mater. Chem. C* **2014**, *2*, 3189-3198.
94. Kriegel, I.; Rodríguez-Fernández, J.; Wisnet, A.; Zhang, H.; Waurisch, C.; Eychmüller, A.; Dubavik, A.; Govorov, A. O.; Feldmann, J. Shedding Light on Vacancy-Doped Copper Chalcogenides: Shape-Controlled Synthesis, Optical Properties, and Modeling of Copper Telluride Nanocrystals with Near-Infrared Plasmon Resonances. *ACS Nano* **2013**, *7*, 4367-4377.
95. Lesnyak, V.; Brescia, R.; Messina, G. C.; Manna, L. Cu Vacancies Boost Cation Exchange Reactions in Copper Selenide Nanocrystals. *J. Am. Chem. Soc.* **2015**, *137*, 9315-9323.
96. De Trizio, L.; Li, H.; Casu, A.; Genovese, A.; Sathya, A.; Messina, G. C.; Manna, L. Sn Cation Valency Dependence in Cation Exchange Reactions Involving Cu_{2-x}Se Nanocrystals. *J. Am. Chem. Soc.* **2014**, *136*, 16277-16284.
97. Haertling, T. Photochemical Tuning of Surface Plasmon Resonances in Metal Nanoparticles, 2009.
98. Link, S.; El-Sayed, M. Spectral Properties and Relaxation Dynamics of Surface Plasmon Electronic Oscillations in Gold and Silver Nano-dots and Nano-rods. *J Phys Chem B* **1999**, *103*, 8410-8426.
99. Wagner, F. E.; Haslbeck, S.; Stievano, L.; Calogero, S.; Pankhurst, Q. A.; Martinek, K. P. Before Striking Gold in Gold-Ruby Glass. *Nature* **2000**, *407*, 691-692.
100. Kreibig, U.; Fragstein, C. The Limitation of Electron Mean Free Path in Small Silver Particles. *Zeitschrift für Physik* **1969**, *224*, 307-323.
101. Mie, G. Beiträge zur Optik trüber Medien, speziell kolloidaler Metallösungen. *Ann. Phys.* **1908**, *330*, 377-445.

102. Buonsanti, R.; Llordes, A.; Aloni, S.; Helms, B. A.; Milliron, D. J. Tunable Infrared Absorption and Visible Transparency of Colloidal Aluminum-Doped Zinc Oxide Nanocrystals. *Nano Lett.* **2011**, *11*, 4706-4710.
103. Manthiram, K.; Alivisatos, A. P. Tunable Localized Surface Plasmon Resonances in Tungsten Oxide Nanocrystals. *J. Am. Chem. Soc.* **2012**, *134*, 3995-3998.
104. Huang, Q.; Hu, S.; Zhuang, J.; Wang, X. MoO_{3-x}-Based Hybrids with Tunable Localized Surface Plasmon Resonances: Chemical Oxidation Driving Transformation from Ultrathin Nanosheets to Nanotubes. *Chem. - Eur. J.* **2012**, *18*, 15283-15287, S15283/1-S15283/6.
105. Wang, S.; Riedinger, A.; Li, H.; Fu, C.; Liu, H.; Li, L.; Liu, T.; Tan, L.; Barthel, M. J.; Pugliese, G.; De Donato, F.; Scotto D'Abbusco, M.; Meng, X.; Manna, L.; Meng, H.; Pellegrino, T. Plasmonic Copper Sulfide Nanocrystals Exhibiting Near-Infrared Photothermal and Photodynamic Therapeutic Effects. *ACS Nano* **2015**, *9*, 1788-1800.
106. Liu, Y.; Deng, Y.; Sun, Z.; Wei, J.; Zheng, G.; Asiri, A. M.; Khan, S. B.; Rahman, M. M.; Zhao, D. Hierarchical Cu₂S Microsponges Constructed from Nanosheets for Efficient Photocatalysis. *Small* **2013**, *9*, 2702-2708.
107. Page, M.; Niitsoo, O.; Itzhaik, Y.; Cahen, D.; Hodes, G. Copper Sulfide as a Light Absorber in Wet-Chemical Synthesized Extremely Thin Absorber (ETA) Solar Cells. *Energy Environ. Sci.* **2009**, *2*, 220-223.
108. Garba, E. J. D.; Jacobs, R. L. The Electronic Structure of Copper Selenide Cu_{2-x}Se. *Physica B+C (Amsterdam)* **1986**, *138*, 253-60.
109. Saldanha, P. L.; Brescia, R.; Prato, M.; Li, H.; Povia, M.; Manna, L.; Lesnyak, V. Generalized One-Pot Synthesis of Copper Sulfide, Selenide-Sulfide, and Telluride-Sulfide Nanoparticles. *Chem. Mater.* **2014**, *26*, 1442-1449.
110. Riha, S. C.; Johnson, D. C.; Prieto, A. L. Cu₂Se Nanoparticles with Tunable Electronic Properties Due to a Controlled Solid-State Phase Transition Driven by Copper Oxidation and Cationic Conduction. *J. Am. Chem. Soc.* **2011**, *133*, 1383-1390.
111. Xie, Y.; Carbone, L.; Nobile, C.; Grillo, V.; D'Agostino, S.; Della Sala, F.; Giannini, C.; Altamura, D.; Oelsner, C.; Kryschi, C.; Cozzoli, P. D. Metallic-like Stoichiometric Copper Sulfide Nanocrystals: Phase- and Shape-Selective Synthesis, Near-Infrared Surface Plasmon Resonance Properties, and Their Modeling. *ACS Nano* **2013**, *7*, 7352-7369.
112. Fjellvåg, H.; Grønvold, F.; Stølen, S.; Andresen, A. F.; Müller-Käfer, R.; Simon, A. Low-Temperature Structural Distortion in CuS. *Zeitschrift für Kristallographie* **2010**, *184*, 111.
113. Liang, W.; Whangbo, M. -. Conductivity Anisotropy and Structural Phase Transition in Covellite CuS. *Solid State Commun.* **1993**, *85*, 405-408.

114. Jain, P. K.; Manthiram, K.; Engel, J. H.; White, S. L.; Faucheaux, J. A.; Alivisatos, A. P. Doped Nanocrystals as Plasmonic Probes of Redox Chemistry. *Angew. Chem., Int. Ed.* **2013**, *52*, 13671-13675.
115. Balitskii, O. A.; Sytnyk, M.; Stangl, J.; Primetzhofer, D.; Groiss, H.; Heiss, W. Tuning the Localized Surface Plasmon Resonance in Cu_{2-x}Se Nanocrystals by Postsynthetic Ligand Exchange. *ACS Appl. Mater. Interfaces* **2014**, *6*, 17770-17775.
116. Faucheaux, J. A.; Stanton, A. L. D.; Jain, P. K. Plasmon Resonances of Semiconductor Nanocrystals: Physical Principles and New Opportunities. *J. Phys. Chem. Lett.* **2014**, *5*, 976-985.
117. Burstein, E. Anomalous Optical Absorption Limit in InSb. *Phys. Rev.* **1954**, *93*, 632-3.
118. Moss, T. S. The Interpretation of the Properties of Indium Antimonide. *Proc. Phys. Soc., London* **1954**, *67B*, 775-82.
119. Mocatta, D.; Cohen, G.; Schattner, J.; Millo, O.; Rabani, E.; Banin, U. Heavily Doped Semiconductor Nanocrystal Quantum Dots. *Science (Washington, DC, U. S.)* **2011**, *332*, 77-81.
120. Abram, R. A.; Rees, G. J.; Wilson, B. L. H. Heavily Doped Semiconductors and Devices. *Adv. Phys.* **1978**, *27*, 799-892.
121. Mulvaney, P. Surface Plasmon Spectroscopy of Nanosized Metal Particles. *Langmuir* **1996**, *12*, 788-800.
122. Liu, X.; Wang, X.; Swihart, M. T. Cu_{2-x}S_{1-y}Se_y Alloy Nanocrystals with Broadly Tunable Near-Infrared Localized Surface Plasmon Resonance. *Chem. Mater.* **2013**, *25*, 4402-4408.
123. Hsu, S.; On, K.; Tao, A. R. Localized Surface Plasmon Resonances of Anisotropic Semiconductor Nanocrystals. *J. Am. Chem. Soc.* **2011**, *133*, 19072-19075.
124. Hsu, S.; Bryks, W.; Tao, A. R. Effects of Carrier Density and Shape on the Localized Surface Plasmon Resonances of Cu_{2-x}S Nanodisks. *Chem. Mater.* **2012**, *24*, 3765-3771.
125. Jain, P. K.; Huang, W.; El-Sayed, M. On the Universal Scaling Behavior of the Distance Decay of Plasmon Coupling in Metal Nanoparticle Pairs: A Plasmon Ruler Equation. *Nano Lett.* **2007**, *7*, 2080-2088.
126. Garcia, G.; Buonsanti, R.; Runnerstrom, E. L.; Mendelsberg, R. J.; Llodes, A.; Anders, A.; Richardson, T. J.; Milliron, D. J. Dynamically Modulating the Surface Plasmon Resonance of Doped Semiconductor Nanocrystals. *Nano Lett.* **2011**, *11*, 4415-4420.

127. Liu, X.; Swihart, M. T. Heavily-Doped Colloidal Semiconductor and Metal Oxide Nanocrystals: an Emerging New Class of Plasmonic Nanomaterials. *Chem. Soc. Rev.* **2014**, *43*, 3908-3920.
128. Furukawa, H.; Cordova, K. E.; O'Keeffe, M.; Yaghi, O. M. The Chemistry and Applications of Metal-Organic Frameworks. *Science* **2013**, *341*.
129. Gangu, K. K.; Maddila, S.; Mukkamala, S. B.; Jonnalagadda, S. B. A Review on Contemporary Metal-Organic Framework Materials. *Inorg. Chim. Acta* **2016**, *446*, 61-74.
130. Park, K. S.; Ni, Z.; Cote, A. P.; Choi, J. Y.; Huang, R.; Uribe-Romo, F.; Chae, H. K.; O'Keeffe, M.; Yaghi, O. M. Exceptional Chemical and Thermal Stability of Zeolitic Imidazolate Frameworks. *Proc. Natl. Acad. Sci. U. S. A.* **2006**, *103*, 10186-10191.
131. Pimentel, B. R.; Parulkar, A.; Zhou, E.; Brunelli, N. A.; Lively, R. P. Zeolitic Imidazolate Frameworks: Next-Generation Materials for Energy-Efficient Gas Separations. *ChemSusChem* **2014**, *7*, 3202-3240.
132. Chen, B.; Yang, Z.; Zhu, Y.; Xia, Y. Zeolitic Imidazolate Framework Materials: Recent Progress in Synthesis and Applications. *J. Mater. Chem. A* **2014**, *2*, 16811-16831.
133. Diestel, L.; Bux, H.; Wachsmuth, D.; Caro, J. Pervaporation Studies of n-Hexane, Benzene, Mesitylene and their Mixtures on Zeolitic Imidazolate Framework-8 Membranes. *Microporous Mesoporous Mater.* **2012**, *164*, 288-293.
134. Kreno, L. E.; Leong, K.; Farha, O. K.; Allendorf, M.; Van Duyne, R. P.; Hupp, J. T. Metal-Organic Framework Materials as Chemical Sensors. *Chem. Rev.* **2012**, *112*, 1105-1125.
135. Eddaoudi, M.; Sava, D. F.; Eubank, J. F.; Adil, K.; Guillerm, V. Zeolite-Like Metal-Organic Frameworks (ZMOFs): Design, Synthesis, and Properties. *Chem. Soc. Rev.* **2015**, *44*, 228-249.
136. Lalonde, M.; Bury, W.; Karagiari, O.; Brown, Z.; Hupp, J. T.; Farha, O. K. Transmetalation: Routes to Metal Exchange within Metal-Organic Frameworks. *J. Mater. Chem. A* **2013**, *1*, 5453-5468.
137. Brozek, C. K.; Dinca, M. Cation Exchange at the Secondary Building Units of Metal-Organic Frameworks. *Chem. Soc. Rev.* **2014**, *43*, 5456-5467.
138. Deria, P.; Mondloch, J. E.; Karagiari, O.; Bury, W.; Hupp, J. T.; Farha, O. K. Beyond Post-Synthesis Modification: Evolution of Metal-Organic Frameworks via Building Block Replacement. *Chem. Soc. Rev.* **2014**, *43*, 5896-5912.
139. Cohen, S. M. Postsynthetic Methods for the Functionalization of Metal-Organic Frameworks. *Chem. Rev.* **2012**, *112*, 970-1000.

140. Tanabe, K. K.; Cohen, S. M. Postsynthetic Modification of Metal-Organic Frameworks-a Progress Report. *Chem. Soc. Rev.* **2011**, *40*, 498-519.
141. Hermes, S.; Schroeter, M.; Schmid, R.; Khodeir, L.; Muhler, M.; Tissler, A.; Fischer, R. W.; Fischer, R. A. Metal@MOF: Loading of Highly Porous Coordination Polymers Host Lattices by Metal Organic Chemical Vapor Deposition. *Angew. Chem., Int. Ed.* **2005**, *44*, 6237-6241.
142. Lu, G.; Li, S.; Guo, Z.; Farha, O. K.; Hauser, B. G.; Qi, X.; Wang, Y.; Wang, X.; Han, S.; Liu, X.; DuChene, J. S.; Zhang, H.; Zhang, Q.; Chen, X.; Ma, J.; Loo, S. C. J.; Wei, W. D.; Yang, Y.; Hupp, J. T.; Huo, F. Imparting Functionality to a Metal-Organic Framework Material by Controlled Nanoparticle Encapsulation. *Nat Chem* **2012**, *4*, 310-316.
143. Meilikhov, M.; Yussenko, K.; Esken, D.; Turner, S.; Van Tendeloo, G.; Fischer, R. A. Metals@MOFs - Loading MOFs with Metal Nanoparticles for Hybrid Functions. *Eur. J. Inorg. Chem.* **2010**, 3701-3714.
144. Doherty, C. M.; Buso, D.; Hill, A. J.; Furukawa, S.; Kitagawa, S.; Falcaro, P. Using Functional Nano- and Microparticles for the Preparation of Metal-Organic Framework Composites with Novel Properties. *Acc. Chem. Res.* **2014**, *47*, 396-405.
145. Falcaro, P.; Ricco, R.; Yazdi, A.; Imaz, I.; Furukawa, S.; MasPOCH, D.; Ameloot, R.; Evans, J. D.; Doonan, C. J. Application of Metal and Metal Oxide Nanoparticles @ MOFs. *Coord. Chem. Rev.* **2016**, *307*, 237-254.
146. Hu, P.; Morabito, J. V.; Tsung, C. Core-Shell Catalysts of Metal Nanoparticle Core and Metal-Organic Framework Shell. *ACS Catal.* **2014**, *4*, 4409-4419.
147. Roesler, C.; Fischer, R. A. Metal-Organic Frameworks as Hosts for Nanoparticles. *CrystEngComm* **2015**, *17*, 199-217.
148. Aguilera-Sigalat, J.; Bradshaw, D. Synthesis and Applications of Metal-Organic Framework-Quantum Dot (QD@MOF) Composites. *Coord. Chem. Rev.* **2016**, *307*, 267-291.
149. Moon, H. R.; Lim, D.; Suh, M. P. Fabrication of Metal Nanoparticles in Metal-Organic Frameworks. *Chem. Soc. Rev.* **2013**, *42*, 1807-1824.
150. Sugikawa, K.; Nagata, S.; Furukawa, Y.; Kokado, K.; Sada, K. Stable and Functional Gold Nanorod Composites with a Metal-Organic Framework Crystalline Shell. *Chem. Mater.* **2013**, *25*, 2565-2570.

2 Tuning the LSPR by Metal Growth, Cation Intercalation & Exchange

2.1 Summary

As described in section 1.4, Cu_{2-x}Se as well as $\text{Cu}_{1.1}\text{S}$ are exhibiting an LSPR caused by valence band holes. Even though their origin differs, as in berzelianite they originate from copper vacancies, while in covellite the free electron holes are lattice constitutional, they both can be tuned postsynthetically. The LSPR of Cu_{2-x}Se can be tuned reversibly by oxidation and respectively by addition of reducing agents or Cu(I) ions. On the other hand, the Cu(I) addition to $\text{Cu}_{1.1}\text{S}$ NPs leads to structural changes that are accompanied by the reduction of free charge carriers, and the subsequent shift and damping of the resonance band. However, both systems are still very sensitive to the exposure to air, making the achieved changes non-permanent. Hence, this chapter explores and compares cation exchange, and cation intercalation experiments to achieve a tunable LSPR which is stable under ambient conditions. Furthermore, copper chalcogenide- metal hybrids are grown, and the effect of the interaction of the metal LSPR with the LSPR of the copper chalcogenide is studied.

Chapter 2.2 compares the effects of the treatment of the two copper chalcogenide systems with Cu(I) ions and the effects of their treatment with Ag(I) ions. Although the treatment of both plasmonic samples with Cu(I) lead to a hypsochromic shift and damping, the same behavior was only observed for the $\text{Cu}_{1.1}\text{S}$ system when Ag(I) was intercalated. The treatment of Cu_{2-x}Se system with Ag(I) resulted in a cation exchange with Ag(I) that resulted in a LSPR damping without an accompanying hypsochromic shift. This was assigned to the emergence of charge carrier scattering centers within the NPs. On the other hand, the observations for Ag(I) treatment of the covellite system are assigned to cation intercalation as the Ag(I) ions break the S-S bonds

2 Tuning the LSPR by Metal Growth, Cation Intercalation & Exchange

between the layers in a similar way that Cu(I) does. Hence, for Cu_{2-x}Se NPs an increasing damping constant was measured for an increasing silver concentration. This was not observed for the $\text{Cu}_{1.1}\text{S}$ NPs. The changes induced by the Ag(I) treatment in both systems are furthermore non-reversible upon oxygen exposure. The partial cation exchange of $\text{Cu}_{1.1}\text{S}$ with Au(I) in a reducing environment is leading to a similar optical response, and is forming $\text{Au}_2\text{S-Cu}_{1.1}\text{S}$ core-crown NP, which is rather comparable to observations in a later work by Xie *et al.*, as discussed in chapter 1.2.3.

The growth of Au domains on Cu_{2-x}Se NPs, resulting in a dual plasmonic hybrid NPs ($\text{Au-Cu}_{2-x}\text{Se}$) is reported in chapter 2.2 as well. The resulting particles exhibit a clear absorption band of the Au LSPR, as well as of the Cu_{2-x}Se LSPR. The later can furthermore be tuned by Cu(I) and Ag(I) addition, as previously described for pure Cu_{2-x}Se NPs. The two LSPRs, especially for Au domains up to 8.0 nm, are only weakly coupled, which is apparent by the small changes of the Au LSPR position during the reduction experiments of the Cu_{2-x}Se domain with Cu(I). This unexpected observation is in contrast to some previous reports, which observed a merge of the two plasmon bands in the absorption spectra due to charge redistribution between the two domains. The observed difference was assumed to be caused by a charge carrier barrier between the domains, possibly due to the reverse growth strategy at room temperature that was applied in this work.

Chapter 2.3 examines two other metal-semiconductor hybrids. Starting from Cu_{2-x}Se and $\text{Cu}_{1.1}\text{S}$ NPs, the growth of a CuPt respectively Pt domains is presented, and the resulting hybrid NP are characterized. In contrast to the $\text{Au-Cu}_{2-x}\text{Se}$ NPs, the formation of a cubic CuPt alloy domain is observed on the Cu_{2-x}Se NPs, whose formation is accompanied with a strong bathochromic shift, and full damping of the LSPR for Se:Pt ratios larger than 1:0.25. The rapid damping cannot fully be explained by crystallographic changes. Hence, the strong damping, observed even for small Pt amounts was assigned to electron injection into the Cu_{2-x}Se domain, causing a reduction of the electron holes in the valence band. The Pt domains on $\text{Cu}_{1.1}\text{S}$ NPs (one to multiple, 2-3 nm in size each), result in a comparable (complete) damping and bathochromic shift of the copper chalcogenide LSPR. As the structural characterizations (XPS, EDX and XRD) did not show any signs of cation exchange or intercalation, this fact was assigned to a combination of electron injection from the

2 Tuning the LSPR by Metal Growth, Cation Intercalation & Exchange

metallic Pt into the copper chalcogenide domain, as well as a crystallographic phase change of the copper chalcogenide domain.

2.2 Tuning the LSPR in Copper Chalcogenide Nanoparticles by Cation Intercalation, Cation Exchange and Metal Growth

Andreas Wolf, Torben Kodanek and Dirk Dorfs

Nanoscale, 2015, 7, 19519-19527.

Reproduced from Nanoscale with permission from The Royal Society of Chemistry.

Article DOI: [10.1039/c5nr05425g](https://doi.org/10.1039/c5nr05425g)

Supporting Information is also available online on the journal's website.

Cite this: *Nanoscale*, 2015, 7, 19519

Tuning the LSPR in copper chalcogenide nanoparticles by cation intercalation, cation exchange and metal growth†

Andreas Wolf, Torben Kodanek and Dirk Dorfs*

Localized surface plasmon resonances (LSPRs) of degenerately doped copper chalcogenide nanoparticles (NPs) (Cu_{2-x}Se berzelianite and $\text{Cu}_{1.1}\text{S}$ covellite) have been modified applying different methods. The comparison of the cation exchange (Cu_{2-x}Se) and intercalation ($\text{Cu}_{1.1}\text{S}$) of $\text{Ag}(\text{I})$ and $\text{Cu}(\text{I})$ has shown that $\text{Ag}(\text{I})$ causes a non reversible, air stable shift of the LSPR. This was compared to the influence of $\text{Au}(\text{I})$ cation exchange into $\text{Cu}_{1.1}\text{S}$ platelets under the formation of $\text{Cu}_{1.1}\text{S}-\text{Au}_2\text{S}$ mixed nanoplatelets. Furthermore, we show the growth of Au domains on Cu_{2-x}Se , and discuss the interaction of the two plasmonic parts of the obtained dual plasmonic $\text{Cu}_{2-x}\text{Se}-\text{Au}$ hybrid particles.

Received 11th August 2015,
Accepted 28th October 2015
DOI: 10.1039/c5nr05425g

www.rsc.org/nanoscale

Introduction

Localized surface plasmon resonances (LSPRs) are typically known for nanosized metals like *e.g.* gold and silver. In recent years the near infrared (NIR) absorption band in several degenerately doped copper chalcogenide NPs (Cu_{2-x}Se ,^{1–3} Cu_{2-x}S ,^{4–7} Cu_{2-x}Te ,^{8,9} and their alloys^{10–12}) was also discovered to be of plasmonic origin. The use of LSPRs in a broad range of applications has been shown extensively.^{13–16} However, tuning LSPRs of metals into the NIR region is only possible with very large particles^{17,18} or *via* shape control^{13,19,20} (*e.g.* nanorods, core-shell structures, *etc.*). Doped semiconductors enable tuning of the plasmon band in the NIR for particles with a size as small as 3 nm.⁴ This enables additional applications in the second biological window (1000–1350 nm) which even has a larger penetration depth and a higher maximum permissible exposure to lasers than the first biological window (700–950 nm).^{21,22} The post synthesis and reversible change of the dopant concentration and hence the spectral positioning of the LSPR makes these degenerately doped quantum dots specifically interesting for nanophotonics, as this enables the possibility to switch resonances ON/OFF.²³ An extensive overview of the properties of these new plasmonic materials can be found in several recent reviews to this topic.^{24–27}

In this article we analyze different approaches to modify and stabilize the LSPR of copper chalcogenide NCs in an

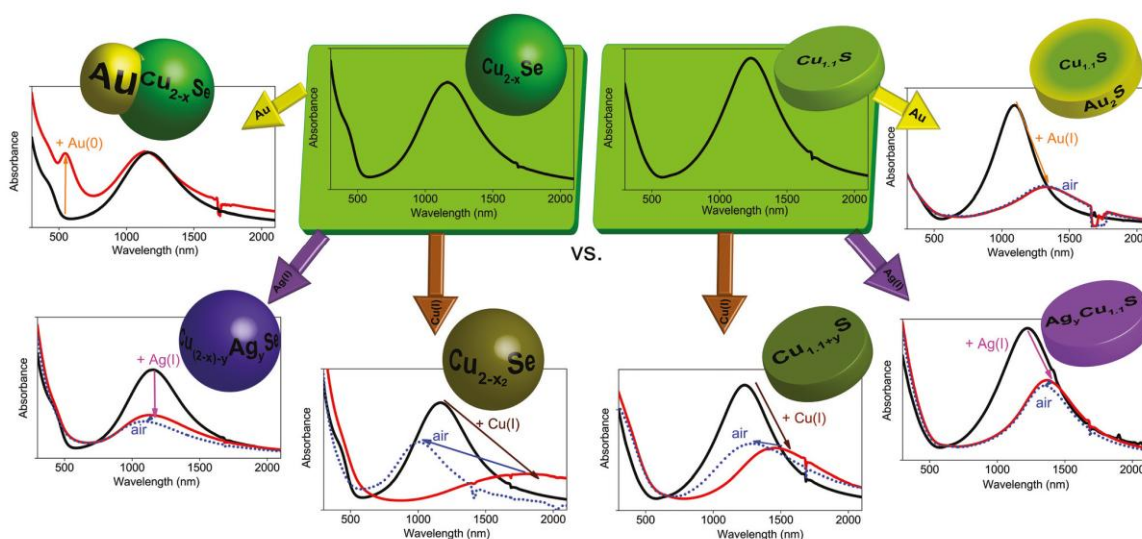
attempt to increase their controlled flexibility for future applications: ion intercalation, ion exchange and metal growth. First, we explore the LSPR response of $\text{Cu}_{1.1}\text{S}$ vs. Cu_{2-x}Se NCs to the addition of univalent ions. We compare the different behavior of the Cu_{2-x}Se LSPR and the $\text{Cu}_{1.1}\text{S}$ LSPR, specifically the different shifting, damping and temporal stability of the LSPR after the integration of $\text{Cu}(\text{I})$ ions vs. $\text{Ag}(\text{I})$ ions (Scheme 1). Second, we present to the best of our knowledge for the first time growth of Au domains on pre-synthesized Cu_{2-x}Se NPs (Scheme 1). The few previous reports on $\text{Au}-\text{Cu}_{2-x}\text{Se}$ ²⁸ and $\text{Au}-\text{Cu}_{2-x}\text{S}$ ^{22,29–34} heterodimers have been either growing the copper chalcogenide onto a readily existing gold seed^{22,32–34} or by first synthesizing $\text{Au}-\text{Cu}$ ^{29–31,35} alloy NPs, which were subsequently converted by sulfidation to $\text{Au}-\text{Cu}_{2-x}\text{S}$. The here presented synthesis approach enables us to grow Au on readily existing berzelianite Cu_{2-x}Se NPs resulting in dual-plasmonic hybrid NPs. This synthesis approach enables us to analyze the change of the chalcogenide LSPR through the interaction with differently sized metal domains on their surface. The same approach, applied to $\text{Cu}_{1.1}\text{S}$ NPs, results in a cation exchange to $\text{Au}_2\text{S}-\text{Cu}_{1.1}\text{S}$ platelet shaped hybrid particles (Scheme 1).

Results and discussion

Chalcogenide starting NPs – Cu_{2-x}Se and $\text{Cu}_{1.1}\text{S}$

In order to study the influence of gold domains and different cations on the LSPR of copper chalcogenides, Cu_{2-x}Se berzelianite and $\text{Cu}_{1.1}\text{S}$ covellite nanoparticles have been synthesized. The Cu_{2-x}Se particles were synthesized by adapting a hot-injection synthesis previously reported resulting in 12.7 ± 1.7 nm

Institute of Physical Chemistry and Electrochemistry, Leibniz Universität Hannover, Callinstr. 3A, 30167 Hannover, Germany. E-mail: dirk.dorfs@pci.uni-hannover.de
† Electronic supplementary information (ESI) available: Further HAADF-STEM images and EDX mappings, further absorbance spectra and the theoretical dependence of the extinction cross section against γ . See DOI: 10.1039/c5nr05425g



Scheme 1 Overview of the presented approaches for tuning the LSPR in spherical Cu_{2-x}Se NPs and $\text{Cu}_{1.1}\text{S}$ nanoplatelets.

mainly spherical nanocrystals.³⁶ The $\text{Cu}_{1.1}\text{S}$ nanoparticles were synthesized by adapting the synthesis from Xie *et al.* resulting in nanoplatelets with the diameter of 13.2 ± 2.9 nm, and a thickness of 5.8 ± 0.9 nm.⁶ Cu_{2-x}Se NPs (after exposure to air) and as-synthesized $\text{Cu}_{1.1}\text{S}$ show a clear LSPR with a maximum around 1155 nm and 1230 nm respectively (see Fig. 1). The LSPRs in the NIR emerge from a high density of free p-type charge carriers in the self-doped NPs.^{1,4,6} The origin of these are the cation vacancies in the Cu_{2-x}Se system and intrinsic valence-band-delocalized holes in the metallic covellite system.^{1,6,37}

Addition of Cu(I) and Ag(I) ions to Cu_{2-x}Se and $\text{Cu}_{1.1}\text{S}$

We compare the influence on the modulation of the Cu_{2-x}Se and $\text{Cu}_{1.1}\text{S}$ LSPRs through the addition of univalent ions. Specifically, we compare the different changes in the absorption spectra after the addition of different amounts of Cu(I) vs. Ag(I) ions. We discuss the spectral shifts of the LSPRs maxima and their oscillator strength as well as the long term stability of these changes under oxidizing conditions. Even though the LSPRs of the Cu_{2-x}Se and the $\text{Cu}_{1.1}\text{S}$ system have a similar origin in the valence-band-delocalized holes, the above mentioned spectral changes are quite opposed for the two systems after the treatment with Cu(I) vs. Ag(I). The origin of this behavior will be discussed in the following section.

Previous reports have shown that for Cu_{2-x}Se and $\text{Cu}_{1.1}\text{S}$ a bathochromic shift accompanied by a decrease of the oscillator strength of the LSPR can be detected after the addition of Cu(I), that finally leads to a complete disappearance of the LSPR for higher Cu(I) amounts.^{1,6} This was shown to be reversible for Cu_{2-x}Se .¹ It was also shown that during the oxidation of Cu_2Se to Cu_{2-x}Se the cubic berzelianite crystal structure does not change.¹ For the $\text{Cu}_{1.1}\text{S}$ covellite system instead, a structural change due to the Cu(I) intercalation was reported;

first to a probably metastable phase and for Cu_2S to either a metastable phase or a mixture of phases.⁶

Adding Cu(I) ions to both systems leads to the same optical response (bathochromic shift and intensity decrease of the LSPR) and ultimately to the complete disappearance of the plasmon band (Fig. 1A/C). Instead, the systems behave contrary to each other when adding an Ag(I) containing solution (Fig. 1B/D). The $\text{Cu}_{1.1}\text{S}$ NPs, whose LSPR have a maximum at 1230 nm, show a decrease of the oscillator strength of the LSPR, which is accompanied by a bathochromic shift until it completely disappears when adding higher Ag(I) amounts. This is similar to the addition of Cu(I). When exposed to air, however, the Ag(I) induced shift is almost irreversible (Fig. 1D) which might be interesting for applications that require specific and stable LSPRs in the NIR. This is remarkable as a Cu(I) induced shift of the LSPR maximum position is reversible (Fig. 1C) when the sample is exposed to air. Cu_{2-x}Se NPs treated with Ag(I) show also a damping of the LSPR intensity, which is, however, not accompanied by a shift to longer wavelength. In this system we rather observe a slight hypsochromic shift of the LSPR maximum (Fig. 1B). Adding 25% Ag(I) ions in relation to the determined copper contents of the NPs leads to a LSPR shift from 1155 nm to 1130 nm after 2 h reaction time. The LSPR shifts and damping stabilizes after a few hours at around 1090 nm. Additionally this shift and the damping are non-reversible under air exposure, which is in contrast to the shift after Cu(I) addition (Fig. 1A). The bathochromic shift for Cu_{2-x}Se after the Cu(I) addition is based on the reduction of the copper deficiencies to zero, resulting in a non plasmonic Cu_2Se system.

Literature lately discusses the stoichiometric changes during reduction as an incorporation of Cu(I) combined with a reduction of the chalcogenide, while a fraction of the Cu(I) is

2 Tuning the LSPR by Metal Growth, Cation Intercalation & Exchange

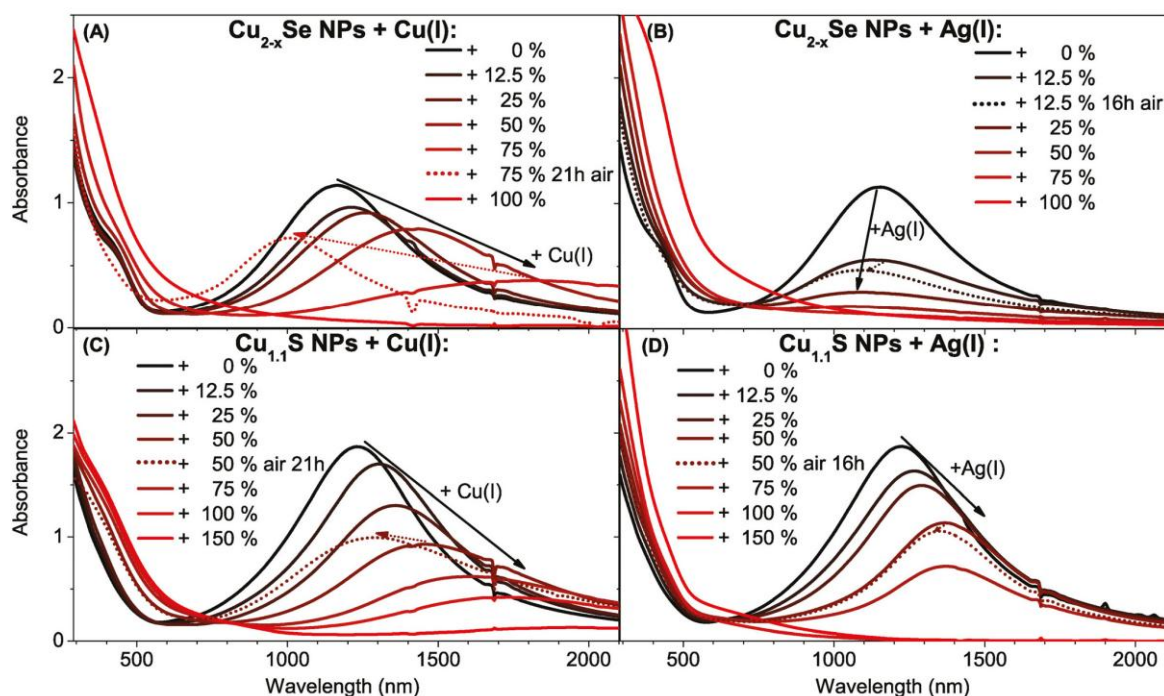


Fig. 1 UV/Vis/NIR absorption spectra of (A, B) Cu_{2-x}Se NPs and (C, D) $\text{Cu}_{1.1}\text{S}$ NPs dissolved in toluene which are treated with different amounts of a (A, C) 0.04 M Cu(I) solution or (B, D) different amounts of a 0.16 M Ag(I) solution. The spectra of the so treated particles after storing under air (dotted lines) for (A, C) 21 hours and (B, D) 16 hours are also shown.

oxidized in solution to Cu(II) in order to provide the required electrons. In fact, the Manna group showed that no Cu(II) can be detected inside copper chalcogenide NPs before or after the reduction.^{6,11}

The LSPR frequency of both self-doped systems can be described by the Drude model.⁴ From eqn (S5) in the ESI† it can be seen, that at a given plasma frequency the increase of the damping factor (γ) leads to an increase of the imaginary part of the dielectric function and hence, according to eqn (S3) in the ESI† to a decrease of the extinction cross section. Following this we suggest, that the reduction of the LSPR band in Cu_{2-x}Se through the Ag(I) addition is caused by a continuous increase of the damping in the system. This damping could be caused by Ag(I) ions that serve as charge carrier scattering centers. An increase of the silver content would hence cause an increased damping. This would cause a decrease of the extinction cross section. As the carrier density does not change significantly it is likely that Ag(I) preferentially exchanges Cu(I) instead of intercalating, as this would not significantly influence the hole density. This is supported by the significant increase of the amount of small Cu_2O NPs that can be seen in the TEM (see Fig. 2A) and HAADF-STEM (see Fig. S1 in the ESI†) images in comparison to samples of the seed particles.

Comparing γ of the Cu_{2-x}Se system, extracted as the full width half maximum from the absorbance plotted against the energy (eV) (see Fig. S2 in the ESI†), it can be seen that γ

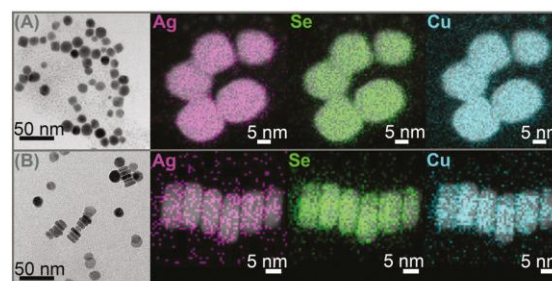


Fig. 2 TEM images and EDX mappings of Ag, Se respectively S and Cu averaged with the corresponding HAADF-STEM images, of Cu_{2-x}Se (A) and $\text{Cu}_{1.1}\text{S}$ (B) NPs after addition of 25% Ag(I) .

increases from 0.43 eV (0% Ag) to 0.53 (12.5% Ag) to 0.57 eV (25% Ag). In contrast to this γ stays constant within the margin of error when Cu(I) ions are added, from 0.43 eV (0% Cu-I-) to 0.42 eV (12.5% & 25% Ag) to 0.41 eV (50% Ag). The increase in γ supports the theory that incorporated Ag(I) ions act as charge carrier scattering centers for the plasmon resonance.

STEM-EDX analysis of a Cu_{2-x}Se sample treated with 25% Ag(I) ions relative to the copper content shows that silver is evenly distributed over a whole NP and does not form Ag_2Se islands (Fig. 2A). This behavior is supported by literature that

shows ternary mixed silver-copper-selenide compounds.³⁸ Additionally we can also exclude the formation of a Ag_2Se shell, as this would have led to a strong bathochromic shift of the plasmon band, due to the high frequency dielectric constant of Ag_2Se ($\epsilon_\infty = 11 \pm 1$ (ref. 39)). This finding is different to the formation of Janus-like NPs that was recently reported for the exchange with divalent cations in Cu_{2-x}Se .⁴⁰ However some EDX mappings of the same sample showed variations in the silver content between different particles (see Fig. S1 in the ESI†). Combining these findings two different mechanisms for the LSPR damping in Cu_{2-x}Se are possible. One theory is that $\text{Ag}(i)$ is forming charge carrier scattering centers in the NPs and hence would increase γ , which would lead to a decrease in the plasmon band intensity. The second theory is that $\text{Cu}(i)$ is exchanged to $\text{Ag}(i)$ preferentially in some particles and in such a high ratio that they lose their LSPR completely. Hence, in that case the weakened LSPR would be caused by Cu_{2-x}Se NPs that do not show any $\text{Ag}(i)$ incorporation after a total addition of 25% $\text{Ag}(i)$.

The $\text{Cu}_{1.1}\text{S}$ system shows a behavior very different to the above described Cu_{2-x}Se when $\text{Ag}(i)$ is added (Fig. 1D). While the LSPR intensity is decreasing it additionally shifts strongly to longer wavelengths. This behavior is quite similar to the one upon addition of $\text{Cu}(i)$ (Fig. 1C), however not reversible upon O_2 exposure. This correlates with a decrease in the charge carrier density (hole density) in the NPs. γ does not increase with the addition of $\text{Ag}(i)$ and $\text{Cu}(i)$. Hence neither of these ions incorporation does create new charge carrier scattering centers.

Elemental mapping of the $\text{Cu}_{1.1}\text{S}$ NPs treated with $\text{Ag}(i)$, does not show island or shell formation (Fig. 2B). Again the silver seems to be homogeneously distributed over each particle, and also no significant variations of the silver content between different particles can be detected.

In the above mentioned analysis it could be shown that the two copper chalcogenide systems behave optically quite opposed. The reason for this could be the different crystal systems. $\text{Cu}_{1.1}\text{S}$ is a hexagonal system with layers, where the reduction of the sulfur in the NCs is accompanied by the intercalation of $\text{Cu}(i)$ between the layers of the original covellite lattice under braking of S-S bonds. At high intercalation levels a structural change to a metastable phase or a mixture between an orthorhombic and a monoclinic phase occurs.⁶ We suggest a similar intercalation of $\text{Ag}(i)$ ions into the pristine covellite (00-006-0464) starting NPs. The XRD patterns show the continuous formation of a second phase due to the intercalation, the orthorhombic AgCuS (00-044-1436) (Fig. 3B). Upon further $\text{Ag}(i)$ addition a third body-centered tetragonal Ag_3CuS_2 (00-012-0207) phase starts to form. This is in line with the optical observations, as this would cause a continuous shift due to an increase of the cation content in the NPs and hence a decrease of the charge carrier density. The better LSPR stability when exposed to oxygen further shows that the incorporation of the $\text{Ag}(i)$ is not reversible under oxygen exposure, in contrast to added $\text{Cu}(i)$ ions. This is most likely due to more oxygen stable $\text{Cu}(i)$ - $\text{Ag}(i)$ -S phases in comparison

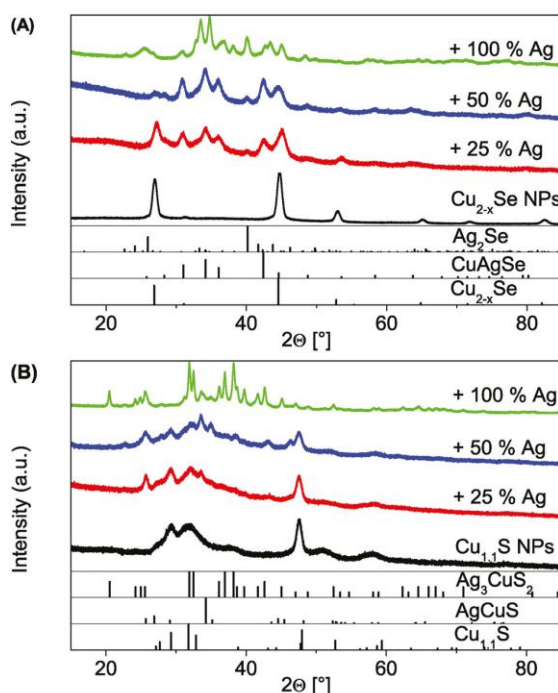


Fig. 3 XRD patterns of the evolution of crystal phases from the pristine copper chalcogenide NPs to mixed silver copper chalcogenide phases. The reference structural data shows fcc Cu_{2-x}Se berzelianite (PDF card #: 01-072-7490), orthorhombic CuAgSe eucairite (PDF card #: 00-010-0451), orthorhombic Ag_2Se naumannite (PDF card #: 01-089-2591), hexagonal $\text{Cu}_{1.1}\text{S}$ covellite (PDF card #: 00-006-0464), base-centered orthorhombic AgCuS stromeyerite (PDF card #: 00-044-1436), body-centered tetragonal Ag_3CuS_2 jalpaitite (PDF card #: 00-012-0207).

to the metastable $\text{Cu}(i)$ -S phases that occur during the $\text{Cu}(i)$ intercalation.

The XRD patterns of the cubic berzelianite Cu_{2-x}Se (01-072-7490) NPs and 25% $\text{Ag}(i)$ sample show the formation of an orthorhombic CuAgSe (00-010-0451) phase (Fig. 3A). If the $\text{Ag}(i)$ content is increased further (to 100%) a full exchange can be observed, as the orthorhombic Ag_2Se phase (01-089-2591) is forming. This shows a clear difference to the $\text{Cu}_{1.1}\text{S}$ system.

To recap the results in this paragraph, it can be seen that due to a controlled exchange (Cu_{2-x}Se) or intercalation ($\text{Cu}_{1.1}\text{S}$) with univalent ions it is possible to damp and shift the LSPR maximum of copper chalcogenides. While both systems show the same, under O_2 exposure reversible, optical trend for the addition of $\text{Cu}(i)$, their behavior varies significantly for the addition of $\text{Ag}(i)$. The Cu_{2-x}Se NPs show a strong, non-reversible damping after $\text{Ag}(i)$ addition. The LSPR of the $\text{Cu}_{1.1}\text{S}$ however can be almost non-reversibly bathochromically shifted by the $\text{Ag}(i)$ addition. This allows a new way to permanently tune the position of the LSPR maximum for degenerately doped chalcogenides. The use in applications that require a stable and specific LSPR under ambient conditions is hence enabled.

Growth of Au domains on Cu_{2-x}Se

In the following paragraph we will show the synthesis of dual-plasmonic Au- Cu_{2-x}Se hybrid NPs and the manipulation of the LSPR of the semiconductor domain due to the addition of different amounts of univalent ions. For this approach differently sized Au domains are grown on the same starting berzelianite seed particles. Furthermore the formation of $\text{Cu}_{1.1}\text{S-Au}_2\text{S}$ hybrids is shown when the same Au growth approach is applied to covellite NPs.

The growth of Au on Cu_{2-x}Se can be controlled by changing the amount of Au-precursor added to the same amount of Cu_{2-x}Se NP solution. $\text{Cu}_2\text{Se}:\text{Au}$ ratios between 1:0.24 and 1:1.89 have been achieved. The TEM bright field images (Fig. 4) show that high contrast Au domains have been grown on the Cu_{2-x}Se seed NPs (lower contrast domains). For the 1:0.24 sample 76% of the Cu_{2-x}Se seed particles have been covered with a $5.6 \text{ nm} \pm 1.3 \text{ nm}$ Au domain. For the 1:0.56 sample $8.0 \text{ nm} \pm 1.6 \text{ nm}$ domains have been grown on 73% of the seed particles (no separately nucleated gold particles were observed). This corresponds roughly to the calculated size of the Au domain per particle assuming 100% reaction yield, which is 6 nm for the 1:0.24 sample and 8 nm for the 1:0.56 sample. The size of the sample with the largest Au amount (1:1.89) could not be determined due to its strong tendency to agglomerate. The XRD patterns (Fig. 5) show a continuous intensity growth of the reflexes that can be assigned to fcc Au (PDF card #: 00-004-0784) while the relative intensity of the

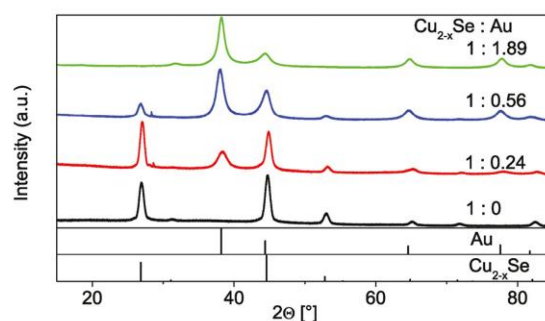


Fig. 5 XRD patterns of the original Cu_{2-x}Se seed particles (1:0) and of the $\text{Cu}_{2-x}\text{Se-Au}$ hybrid structures with different $\text{Cu}_{2-x}\text{Se}:\text{Au}$ ratios (1:0.24, 1:0.56 and 1:1.89). The reference structural data shows fcc Cu_{2-x}Se berzelianite (PDF card #: 01-072-7490) and fcc Au (PDF card #: 00-004-0784).

berzelianite reflexes is decreasing at the same time until they can hardly be detected for the 1:1.86 sample. The relative decrease can be explained by the higher X-ray atomic scattering factor for gold.

With increasing Au content, the absorption spectra (measured with an integrating sphere) of the as-prepared samples show a more pronounced absorption peak centered at 550–600 nm which originates from an LSPR in the Au

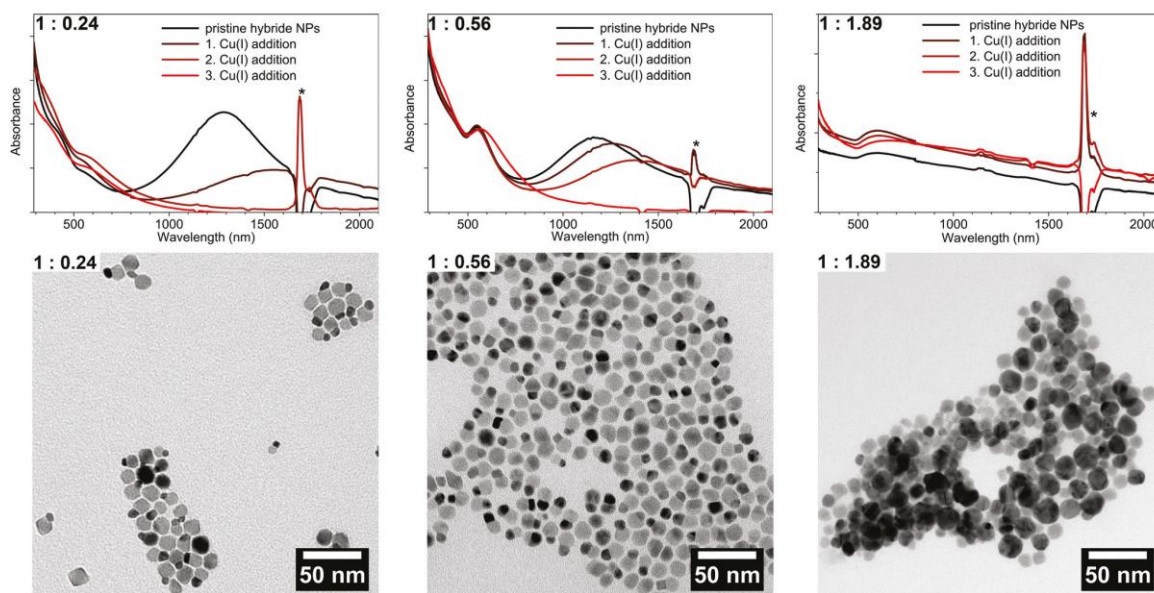


Fig. 4 UV/Vis/NIR absorption spectra (measured with an integrating sphere) and TEM images of Au growth on Cu_{2-x}Se NCs with different amounts of Au precursor ($\text{Cu}_{2-x}\text{Se}:\text{Au} = 1:0.24$, $1:0.56$ and $1:1.89$). As synthesized (black lines) and tuning of the LSPR by addition of $\text{Cu}(\text{i})$. Each step from black to red corresponds to an addition of $5 \mu\text{l}$ of a 0.4 M $\text{Cu}(\text{i})$ solution. *The sharp peaks (around 1700 nm) in the absorption are due to solvent absorption.

domains of the hybrid NPs (Fig. 4). The intensity of the absorption band of the Cu_{2-x}Se LSPR on the other hand decreases with an increasing amount of Au and shows a small hypsochromic shift of about 100 nm from the 1 : 0.24 to 1 : 0.56 sample. A further increase of the Au amount (1 : 1.89 sample) leads to a broad absorption band where no distinct Cu_{2-x}Se LSPR absorption can be distinguished. The broad absorption band rather shows a maximum around 600 nm, however with an absorption onset above 2000 nm. It cannot be excluded that the difference in absorption behavior in comparison to the other samples originates in the strong agglomeration that occurred for this high Au contents.

The as-prepared samples show a LSPR in the NIR region due to the copper deficiency in the Cu_{2-x}Se part. By the addition of Cu(I) ions to this hybrid system, additional Cu(I) is built into the Cu_{2-x}Se , and partially in solution oxidized to Cu(II) (in order to reduce the selenium in the NPs). Hence, the free charge carrier concentration (holes) in the semiconductor domain is reduced. This, as has been discussed in literature^{1,4,6} and previously in this publication, leads to a bathochromic shift and decreased intensity of the copper chalcogenide LSPR as can be seen in Fig. 4.

In contrast to the two distinct and separate LSPR maxima that can be observed for our 1 : 0.24 and 1 : 0.56 sample (Fig. 4), Liu *et al.* described for Cu_{2-x}Se grown on Au seed particles a broad LSPR across visible and NIR wavelengths. They qualitatively analyzed this using a so called quantum model.²⁸ As Cu_{2-x}Se NPs are strongly p-doped, the Fermi level is close to the valence band. In order to achieve thermal equilibrium at the interface, electrons of the metal will diffuse into the semiconductor. The consequence will be an electron density reduction in the Au part, and hence a bathochromic shift of its LSPR. The semiconductor LSPR should show a broadening and reduced intensity, due to a lower charge carrier density.²⁸ Following this model a decrease of p-doping would lead to less electrons being able to diffuse from the metal to the semiconductor part, as to the decrease of p-doping. This, however, would be expected to result in a hypsochromic shift for the Au LSPR for higher Cu(I) amounts being added. No such shift can be observed (Fig. 4). In fact the metal LSPR shifts bathochromically for about 20–30 nm for the 1 : 0.24 and the 1 : 0.56 sample and around 50–60 nm for the 1 : 0.89 sample. One explanation for this shift is the bathochromic shift of the Cu_{2-x}Se band gap absorption, due to its reduction according to the reverse Burstein–Moss effect.

It is worth to note that the position of the plasmon maximum above 550 nm would require a pure Au NP to have a size well above 50 nm. As no such Au particles could be found in any sample the LSPR maximum must hence be explained differently. Another reason for the absorption maximum at relatively long wavelengths is the high frequency dielectric constant of Cu_{2-x}Se ($\epsilon_{\infty} = 11.0\text{--}11.6$)⁴¹ compared to toluene. This approach also explains why no hypsochromic shift of the Au related LSPR is observed during the addition of Cu(I).

Adding Ag(I) ions to the Au– Cu_{2-x}Se hybrid NPs the semiconductor LSPR can be non reversible, bathochromically

shifted as we showed for the pristine Cu_{2-x}Se particles (see Fig. S3 in the ESI†).

We showed here by Au growth experiments that with our synthesis strategy we received dual-plasmonic hybrid Au– Cu_{2-x}Se NPs which exhibit two surprisingly little interacting LSPRs. This is, to the best of our knowledge, the first report of weakly coupled LSPRs in Au–copper chalcogenide hybrid systems. The difference to previous reported hybrid systems might be the reverse growth strategy that allows the coupling of the two domains at room temperature.

Cation exchange of Au(I) into $\text{Cu}_{1.1}\text{S}$

In contrary to the Cu_{2-x}Se –Au hybrid structures, a $\text{Cu}_{1.1}\text{S}$ –Au hybrid structure cannot be observed following our synthetic conditions (Fig. 6). Instead a continuous cation exchange from $\text{Cu}_{1.1}\text{S}$ to Au_2S starting from the edges of the $\text{Cu}_{1.1}\text{S}$ discs resulting in a $\text{Cu}_{1.1}\text{S}$ – Au_2S structure takes place. This is accompanied with a bathochromic shift and an intensity decrease of the LSPR, and was reported so far only for quasi-spherical Cu_{2-x}S NPs.⁴²

The absorbance spectra show a LSPR maximum shift from 1100 nm to 1365 nm from no Au added to a $\text{Cu}_{1.1}\text{S}$: Au ratio of 1 : 11.2 (Fig. 6). The shift of the LSPR is highly stable under air exposure over several days and only shows slight variations in the oscillator strength. The LSPR shift behaves very similar to the one observed for the addition of Ag(I), however due to the slower reaction kinetics an even better control of the exact maximum position can be achieved. The high stability of the LSPR shift under oxygen exposure can be explained due to the

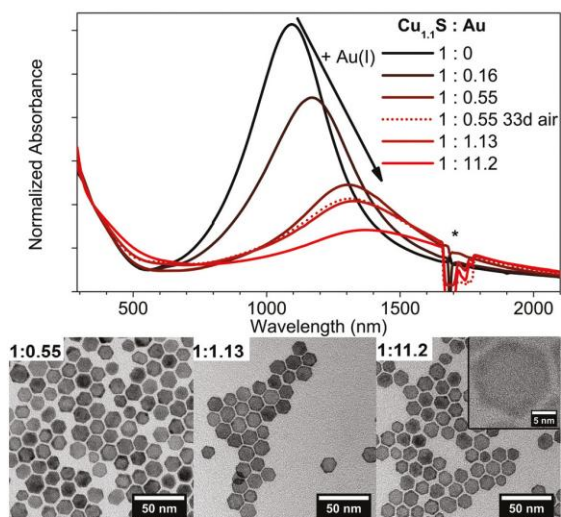


Fig. 6 Normalized absorption spectra and TEM images of covellite $\text{Cu}_{1.1}\text{S}$ NPs treated with different AuCl_3 amounts ($\text{Cu}_{1.1}\text{S}$: Au = 1 : 0.16, 1 : 0.55, 1 : 1.13, 1 : 11.2). The spectra of the 1 : 0.55 sample stored under air for 33 d (dotted line) is also shown. *The peaks around 1700 nm are due to solvent absorption.

formation of the stable Au₂S phase. The increasing formation of Au₂S can be clearly seen in the provided TEM images in Fig. 6. In comparison to pure covellite NPs (see Fig. S4 in the ESI†) these samples show a high contrast crown, due to the higher contrast of elements with a higher atomic number in bright field imaging, which is increasing with higher Au amounts added. By controlling the amount of Au added this technique gives an additional method to shift and stabilize the LSPR maximum at a desired wavelength.

A possible reason for the different behavior of the two systems are their different redox potentials. These result in the reduction of the Au(III) precursor to Au(0) for the Cu_{2-x}Se system but only to Au(I) for the Cu_{1.1}S system.

In summary the growth of Au domains on Cu_{2-x}Se with size control can be achieved with the here presented method. This leads to Au-Cu_{2-x}Se dual-plasmonic hybrid particles with two LSPRs originating from the two domains of the particles. It was shown for the first time that the LSPRs of such Au-copper chalcogenide hybrids influence each other little. Applying the same strategy to grow Au on the Cu_{1.1}S NPs does not result in the growth of Au domains but rather in a cation exchange and the formation of Au₂S-Cu_{1.1}S NPs (see Fig. 6). As with the presented method the exchange is not complete, the LSPR can still be detected; even though it is strongly bathochromically shifted. Additionally the shift is stable also under air exposure for several days.

Conclusions

We have presented different methods to tune the LSPR of degenerately doped Cu_{2-x}Se berzelianite and Cu_{1.1}S covellite NPs. We showed and compared different strategies to change in a controlled manner the LSPR maximum position and its oscillator strength intensity. Specifically we compared the temporal stability of these changes for the ion exchange respectively intercalation of Ag(I) in comparison to the changes with Cu(I). We could show that the intercalation of Ag(I) and the ion exchange of Au(I) into covellite Cu_{1.1}S NPs causes a LSPR bathochromic shift that is more stable also under exposure to air. This reduced air sensitivity enables us to stabilize the LSPR band for possible applications in different wavelength regions than those accessible by the pristine NPs. In comparison the Ag(I) ion exchange in the berzelianite system leads to a damping of the LSPR without a significant shift. We assigned this observation to an increased damping due to the additional Ag(I) in the NPs. Furthermore, we presented a new strategy to synthesize Au-Cu_{2-x}Se dual-plasmonic hybrid nanoparticles. We were able to show with Au growth experiments that the two LSPRs, originating from the different domains of the hybrid NPs, interact surprisingly little with each other.

Overall, the post-synthetic treatment of plasmonic copper chalcogenides gives, despite of its complexity, a manifold way to tune the LSPR of these particles and especially to stabilize the LSPR position also under ambient conditions.

Experimental section

Materials

Copper(I) chloride (CuCl, 99.99% extra pure), ethanol (EtOH, 99.5%, extra dry) and silver nitrate (99.85%) were purchased from Acros Organics. Selenium (Se, 99.999%, 200 mesh), methanol (MeOH, 99.9%, anhydrous), toluene (99.8%, anhydrous packed under argon) and *n*-butanol (99.9% packed under argon) were purchased from Alfa Aesar. Sulfur (S, 99.98%), tetrakis (acetonitrile)copper(I) hexafluorophosphate ([Cu(CH₃CN)₄]PF₆, 97%), dodecylamine (DDA, 98%), didodecyl-dimethylammonium bromide (DDAB, 98%), octadecene (ODE, 90%) and oleylamine (OLA, >70%) were purchased from Sigma Aldrich. Gold(III) chloride (99%) was purchased from ABCR. Hydrochloric acid (>37%, for trace analysis) and nitric acid (>69%, for trace analysis) were purchased from Fluka.

Pre-degassed OLA and ODE were prepared by placing each solvent in a separate flask and heating them under reflux ($\leq 1 \times 10^{-3}$ mbar, 115 °C) for 6 h, while purging them multiple times with argon. Afterwards they are transferred and stored inside the glove box under inert gas.

All other chemicals were used without further purification.

If not otherwise mentioned all experiments have been done under argon using standard Schlenk line techniques or were done inside a nitrogen filled glove box.

Synthesis of Cu_{2-x}Se nanoparticles

The Cu_{2-x}Se spherical nanoparticles have been synthesized adapting a procedure from Deka *et al.*³⁶ 15 ml ODE and 15 ml OLA were degassed for 3 h under vacuum ($\leq 1 \times 10^{-3}$ mbar) at 115 °C in a 100 ml 3-neck flask heated by a heating mantle. After cooling the mixture to room temperature CuCl (297 mg, 3 mmol) is added under a strong argon flow. The mixture was again set under vacuum and heated to 115 °C for an additional 15 min. After setting the flask under a constant argon flow the mixture was rapidly heated in 5–6 min to 300 °C. During that heating the color changed from first yellowish hazy to clear yellow to black. The selenium precursor solution was prepared by mixing Se (117 mg, 1.5 mmol) with pre-degassed 9 ml OLA and evacuating it for 30 min at 115 °C. After setting the flask under a constant argon flow the temperature was left at 190–200 °C. When all Se was dissolved the temperature was raised to 230 °C for 20 min before it was cooled down to 150 °C. At this temperature the solution was transferred into a glass syringe and rapidly injected into the copper precursor solution. Following this, the reaction mixture's temperature dropped to 270 °C and was allowed to recover to 290 °C. 15 min after the injection the solution was rapidly cooled down to room temperature at 150 °C 20 ml toluene were injected into the flask to prevent agglomeration. The particles have been precipitated by addition of 20 ml EtOH and 10 ml MeOH and centrifuged at 3700 g for 20 min. The precipitate was redispersed in 20 ml toluene by ultrasonication for 5 min. After leaving the particles for 12 h they were again centrifuged for 20 min at 3700 g and the supernatant used for all further experiments.

A typical Cu_{2-x}Se NP solution in toluene contains 0.053 mmol per ml Cu_{2-x}Se , this corresponds to roughly 2.5×10^{-6} mmol NPs per ml.

Synthesis of $\text{Cu}_{1.1}\text{S}$ nanoplatelets

The $\text{Cu}_{1.1}\text{S}$ nanoplatelets have been synthesized by up-scaling a method previously reported by Y. Xie *et al.*⁶ A mixture of 40 ml OLA, 40 ml ODE and sulfur (256.5 mg; 8 mmol) were degassed for 30 min under vacuum ($\leq 1 \times 10^{-3}$ mbar) at 120 °C in a 100 ml 3-neck flask. Under argon the temperature was raised to 130 °C and held at this temperature for 5 min. The solution was cooled to room temperature and CuCl (400 mg; 4 mmol) was added to the solution. At addition the solution turns black starting from a clear yellow-orange solution. The flask was again set to vacuum for 60 min at room temperature. The temperature was raised with a ramp of 8 °C min^{-1} to 200 °C and kept there for 30 min. The reaction solution was rapidly cooled to room temperature. After the addition of 40 ml EtOH the particles have been centrifuged for 20 min at 3700g. The precipitate was redissolved in 28 ml toluene. The resulting dark green particle solution was centrifuged at 100g for 5 min to remove larger side products. The supernatant was used for all further experiments. A typical $\text{Cu}_{1.1}\text{S}$ NP solution in toluene contains 0.049 mmol per ml $\text{Cu}_{1.1}\text{S}$, this corresponds to roughly 1.6×10^{-6} mmol NPs per ml.

Cu(i) cation exchange

$[\text{Cu}(\text{CH}_3\text{CN})_4]\text{PF}_6$ (74.5 mg; 0.200 mmol) was dissolved in 5 ml MeOH to receive a 0.04 M Cu(i) solution. A diluted solution of copper chalcogenide particles (oxidized Cu_{2-x}Se respectively $\text{Cu}_{1.1}\text{S}$) was prepared. 3 ml of that solution were given inside a cuvette together with the calculated amount of Cu(i) solution and shaken vigorously. The samples were measured 1 h after preparation.

Ag(i) cation exchange

$\text{AgNO}_3 \cdot 6\text{H}_2\text{O}$ (25 mg; 0.147 mmol) was dissolved in 0.9 ml MeOH to receive a 0.164 M Ag(i) solution. A diluted solution of copper chalcogenide particles ($\text{Cu}_{1.1}\text{S}$ respectively oxidized Cu_{2-x}Se) was prepared. 3 ml of that solution were given inside a cuvette together with the calculated amount of Ag(i) solution and shaken vigorously. The samples were measured 2 h after preparation.

Au growth on Cu_{2-x}Se and Au cation exchange in $\text{Cu}_{1.1}\text{S}$ NPs

The growth of Au on chalcogenide NPs was adapted from the Banin synthesis of Au on CdSe particles.⁴³

An Au-precursor stock solution was freshly prepared with an Au : DDAB : DDA ratio of 1 : 5.5 : 22 and an Au concentration of 0.006 mmol per ml toluene. For that AuCl_3 (72.9 mg; 0.24 mmol), DDAB (611.7 mg; 1.32 mmol) and DDA (980.3 mg; 5.29 mmol) were dissolved in 40 ml toluene. 1.7 ml of a diluted Cu_{2-x}Se solution ($c_{\text{Cu}_{2-x}\text{Se}} = 0.033$ mmol ml^{-1}) and 25 μl OLA are placed in a sample vial and under stirring calculated amounts of the Au-precursor solution are added slowly. The solution is left stirring for 30 min. The particles are separ-

ated by adding MeOH and centrifugation at 3700g. The NPs are redispersed in 4 ml toluene.

For $\text{Cu}_{1.1}\text{S}$ 2 ml of a diluted solution ($c_{\text{Cu}_{1.1}\text{S}} = 0.009$ mmol ml^{-1}) were placed in a sample vial. All further steps have been done like for the Au growth on Cu_{2-x}Se .

UV/Vis/NIR absorption spectroscopy

All spectra were measured on an Agilent Cary 5000 UV/Vis/NIR spectrophotometer. Absorption spectra for Cu_{2-x}Se -Au hybrid NPs were recorded with the spectrophotometer being equipped with an Agilent DRA-2500 Ulbricht sphere to account for slight light scattering of the sample. Samples were prepared by dispersing the NPs in 3 ml of toluene in a 10 mm path length quartz glass cuvette.

Elemental analysis

Quantitative copper elemental analysis was done by atomic absorption spectroscopy (AAS) using a Varian AA 140 spectrometer. The samples were dissolved in aqua regia (1 part HNO_3 and 3 parts HCL) and diluted after several hours with deionized water. The measurements were carried out at a wavelength of 324.8 nm and an acetylene air flame.

Electron microscopy

Conventional TEM and HRTEM measurements were carried out using a FEI Tecnai G2 F20, equipped with a field emission gun operated at 200 kV. EDX measurements were conducted in scanning TEM mode using a JEOL JEM-2100F, operated at 200 kV and equipped with a field emission gun. Sample preparation was done by placing a QUANTIFOIL carbon coated copper grid on a filter paper and dropping 10 μl of a diluted particle solution on it.

Powder X-ray diffraction analysis

XRD analysis was carried out using a Bruker D8 Advance in reflection mode with a Cu source operating at 40 kV and 40 mA. Samples have been prepared by drying a concentrated NP solution on a single crystalline silicon sample holder.

Acknowledgements

D.D. wants to thank the German research foundation (DFG, research grants DO1580/2-1 and DO1580/3-1) and the Volkswagen foundation (lower Saxony/Israel cooperation, Grant ZN2916) for funding. The authors are grateful to N. C. Bigall for helpful discussions. The authors thank the Laboratory of Nano and Quantum Engineering of the Leibniz Universität Hannover for support. T. K. is grateful to the Hannover School for Nanotechnology (HSN) for funding.

References

- 1 D. Dorfs, T. Hartling, K. Miszta, N. C. Bigall, M. R. Kim, A. Genovese, A. Falqui, M. Povia and L. Manna, *J. Am. Chem. Soc.*, 2011, **133**, 11175–11180.

- 2 O. A. Balitskii, M. Sytnyk, J. Stangl, D. Primetzhofer, H. Groiss and W. Heiss, *ACS Appl. Mater. Interfaces*, 2014, **6**, 17770–17775.
- 3 Y. Wang, M. Zhukovskiy, P. Tongying, Y. Tian and M. Kuno, *J. Phys. Chem. Lett.*, 2014, **5**, 3608–3613.
- 4 J. M. Luther, P. K. Jain, T. Ewers and A. P. Alivisatos, *Nat. Mater.*, 2011, **10**, 361–366.
- 5 Y. Zhao, H. Pan, Y. Lou, X. Qiu, J. Zhu and C. Burda, *J. Am. Chem. Soc.*, 2009, **131**, 4253–4261.
- 6 Y. Xie, A. Riedinger, M. Prato, A. Casu, A. Genovese, P. Guardia, S. Sottini, C. Sangregorio, K. Miszta, S. Ghosh, T. Pellegrino and L. Manna, *J. Am. Chem. Soc.*, 2013, **135**, 17630–17637.
- 7 M. Kruszynska, H. Borchert, A. Bachmatiuk, M. H. Ruemmeli, B. Buechner, J. Parisi and J. Kolny-Olesiak, *ACS Nano*, 2012, **6**, 5889–5896.
- 8 I. Kriegel, J. Rodríguez-Fernández, A. Wisnet, H. Zhang, C. Waurisch, A. Eychmüller, A. Dubavik, A. O. Govorov and J. Feldmann, *ACS Nano*, 2013, **7**, 4367–4377.
- 9 W. Li, R. Zamani, G. Rivera Pilar, B. Pelaz, M. Ibanez, D. Cadavid, A. Shavel, R. A. Alvarez-Puebla, W. J. Parak, J. Arbiol and A. Cabot, *J. Am. Chem. Soc.*, 2013, **135**, 7098–7101.
- 10 E. Dilena, D. Dorfs, C. George, K. Miszta, M. Povia, A. Genovese, A. Casu, M. Prato and L. Manna, *J. Mater. Chem.*, 2012, **22**, 13023–13031.
- 11 P. L. Saldanha, R. Brescia, M. Prato, H. Li, M. Povia, L. Manna and V. Lesnyak, *Chem. Mater.*, 2014, **26**, 1442–1449.
- 12 X. Liu, X. Wang and M. T. Swihart, *Chem. Mater.*, 2013, **25**, 4402–4408.
- 13 T. K. Sau, A. L. Rogach, F. Jaeckel, T. A. Klar and J. Feldmann, *Adv. Mater.*, 2010, **22**, 1805–1825.
- 14 P. K. Jain, X. Huang, I. El-Sayed and M. El-Sayed, *Acc. Chem. Res.*, 2008, **41**, 1578–1586.
- 15 N. J. Halas, S. Lal, W. S. Chang, S. Link and P. Nordlander, *Chem. Rev.*, 2011, **111**, 3913–3961.
- 16 B. Sepulveda, P. C. Angelome, L. M. Lechuga and L. Liz-Marzan, *Nano Today*, 2009, **4**, 244–251.
- 17 S. Link and M. El-Sayed, *J. Phys. Chem. B*, 1999, **103**, 4212–4217.
- 18 C. Ziegler and A. Eychmüller, *J. Phys. Chem. C*, 2011, **115**, 4502–4506.
- 19 S. J. Oldenburg, R. D. Averitt, S. L. Westcott and N. J. Halas, *Chem. Phys. Lett.*, 1998, **288**, 243–247.
- 20 C. J. Murphy, T. K. Sau, A. M. Gole, C. J. Orendorff, J. Gao, L. Gou, S. E. Hunyadi and T. Li, *J. Phys. Chem. B*, 2005, **109**, 13857–13870.
- 21 A. N. Bashkatov, E. A. Genina, V. I. Kochubey and V. V. Tuchin, *J. Phys. D: Appl. Phys.*, 2005, **38**, 2543–2555.
- 22 X. Ding, C. H. Liow, M. Zhang, R. Huang, C. Li, H. Shen, M. Liu, Y. Zou, N. Gao, Z. Zhang, Y. Li, Q. Wang, S. Li and J. Jiang, *J. Am. Chem. Soc.*, 2014, **136**, 15684–15693.
- 23 G. Garcia, R. Buonsanti, E. L. Runnerstrom, R. J. Mendelsberg, A. Llordes, A. Anders, T. J. Richardson and D. J. Milliron, *Nano Lett.*, 2011, **11**, 4415–4420.
- 24 Y. Zhao and C. Burda, *Energy Environ. Sci.*, 2012, **5**, 5564–5576.
- 25 J. A. Faucheaux, A. L. D. Stanton and P. K. Jain, *J. Phys. Chem. Lett.*, 2014, **5**, 976–985.
- 26 X. Liu and M. T. Swihart, *Chem. Soc. Rev.*, 2014, **43**, 3908–3920.
- 27 A. Comin and L. Manna, *Chem. Soc. Rev.*, 2014, **43**, 3957–3975.
- 28 X. Liu, C. Lee, W. Law, D. Zhu, M. Liu, M. Jeon, J. Kim, P. N. Prasad, C. Kim and M. T. Swihart, *Nano Lett.*, 2013, **13**, 4333–4339.
- 29 X. Ding, Y. Zou and J. Jiang, *J. Mater. Chem.*, 2012, **22**, 23169–23174.
- 30 N. E. Motl, J. F. Bondi and R. E. Schaak, *Chem. Mater.*, 2012, **24**, 1552–1554.
- 31 S. Shen, Z. Tang, Q. Liu and X. Wang, *Inorg. Chem.*, 2010, **49**, 7799–7807.
- 32 Y. Kim, K. Y. Park, D. M. Jang, Y. M. Song, H. S. Kim, Y. J. Cho, Y. Myung and J. Park, *J. Phys. Chem. C*, 2010, **114**, 22141–22146.
- 33 S. Khanal, G. Casillas, N. Bhattarai, J. Velazquez-Salazar, U. Santiago, A. Ponce, S. Mejia-Rosales and M. Jose-Yacamán, *Langmuir*, 2013, **29**, 9231–9239.
- 34 Z. Sun, Z. Yang, J. Zhou, M. H. Yeung, W. Ni, H. Wu and J. Wang, *Angew. Chem., Int. Ed.*, 2009, **48**, 2881–2885.
- 35 W. Sang, T. Zheng, Y. Wang, X. Li, X. Zhao, J. Zeng and J. G. Hou, *Nano Lett.*, 2014, **14**, 6666–6671.
- 36 S. Deka, A. Genovese, Y. Zhang, K. Miszta, G. Bertoni, R. Krahn, C. Giannini and L. Manna, *J. Am. Chem. Soc.*, 2010, **132**, 8912–8914.
- 37 Y. Xie, L. Carbone, C. Nobile, V. Grillo, S. D'Agostino, F. Della Sala, C. Giannini, D. Altamura, C. Oelsner, C. Kryschi and P. D. Cozzoli, *ACS Nano*, 2013, **7**, 7352–7369.
- 38 D. M. Trots, *Structure and Lattice Dynamics of Copper- and Silver-based Superionic Conducting Chalcogenides*, TU Darmstadt, Darmstadt, 2007.
- 39 V. V. Gorbachev and I. M. Putilin, *Phys. Status Solidi B*, 1975, **69**, K153–K156.
- 40 V. Lesnyak, R. Brescia, G. C. Messina and L. Manna, *J. Am. Chem. Soc.*, 2015, **137**, 9315–9323.
- 41 V. V. Gorbachev and I. M. Putilin, *Phys. Status Solidi A*, 1973, **16**, 553–559.
- 42 X. Wang, X. Liu, D. Zhu and M. T. Swihart, *Nanoscale*, 2014, **6**, 8852–8857.
- 43 T. Mokari, E. Rothenberg, I. Popov, R. Costi and U. Banin, *Science*, 2004, **304**, 1787–1790.

Tuning the LSPR in copper chalcogenide nanoparticles by cation intercalation, cation exchange and metal growth

Received,
Accepted

Andreas Wolf,^a Torben Kodanek^a and Dirk Dorfs^{*a}

DOI: 10.1039/

www.rsc.org/nanoscale

Electronic Supplementary Material (ESI)

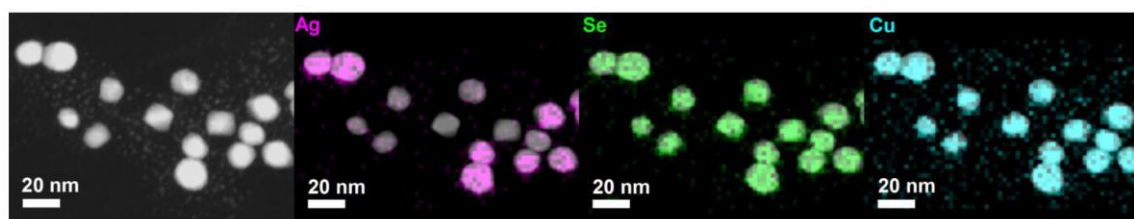


Fig. S1 HAADF-STEM image and EDX mappings of Ag, Se and Cu averaged with the corresponding HAADF-STEM image, of a Cu_{2-x}Se sample after addition of 25 % Ag(I) .

^a Institute of Physical Chemistry and Electrochemistry, Leibniz Universität Hannover, Callinstr. 3A, 30167 Hannover, Germany
E-mail: dirk.dorfs@pci.uni-hannover.de

2 Tuning the LSPR by Metal Growth, Cation Intercalation & Exchange

ARTICLE

Journal Name

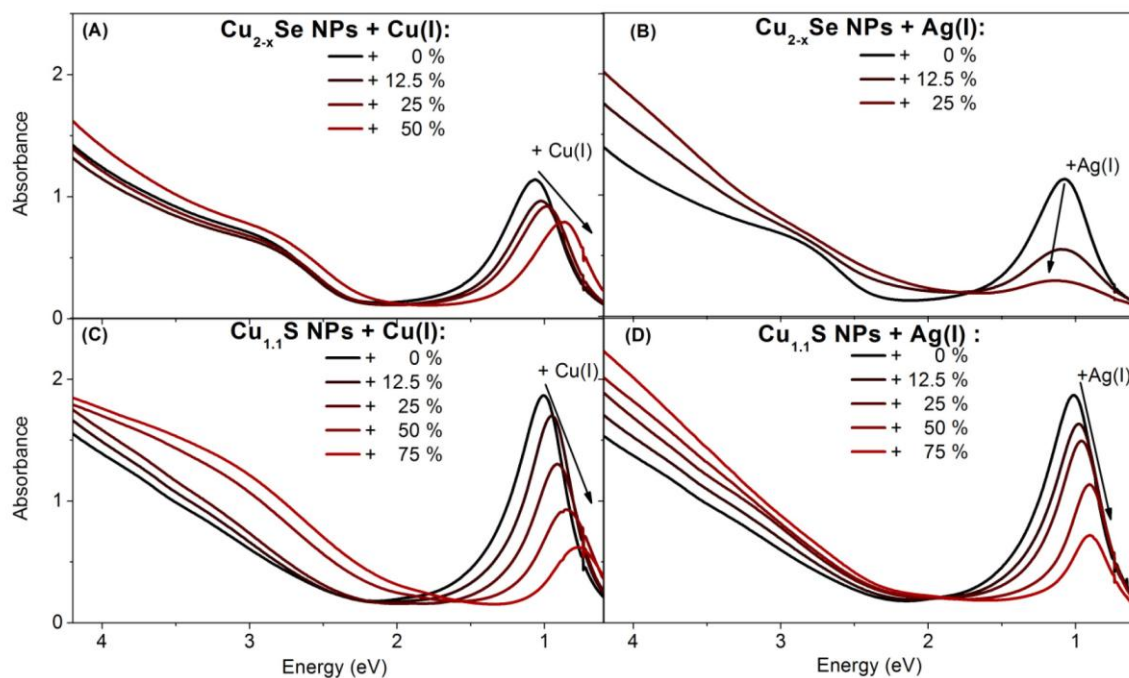


Fig. 52 UV/Vis/NIR absorption measurements plotted against energy (eV) to determine γ as the full width half maximum of the plasmon band. Spectra shown are of (A, B) Cu_{2-x}Se NPs and (C, D) $\text{Cu}_{1.1}\text{S}$ NPs dissolved in toluene which are treated with different amounts of a (A, C) 0.04 M Cu(I) solution or (B, D) different amounts of a 0.16 M Ag(I) solution.

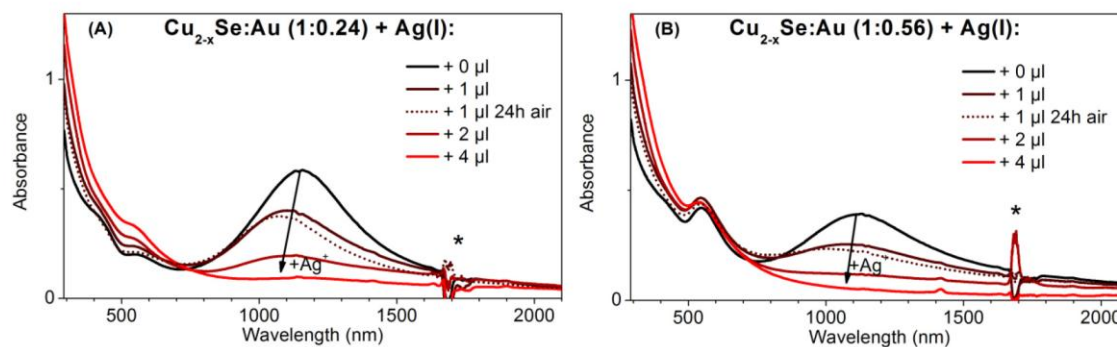


Fig. 53 UV/Vis/NIR absorption spectra of $\text{Cu}_{2-x}\text{Se:Ag}$ hybrids with $\text{Cu}_{2-x}\text{Se:Ag}$ ratios (A) 1:0.24 and (B) 1:0.56 that have been treated with different amounts of an 0.16 M Ag(I) solution. The spectra of the so treated particles after storing under air for 24 h hours (dotted lines) are also shown. * The sharp absorption peaks (around 1700 nm) are due to solvent absorption.

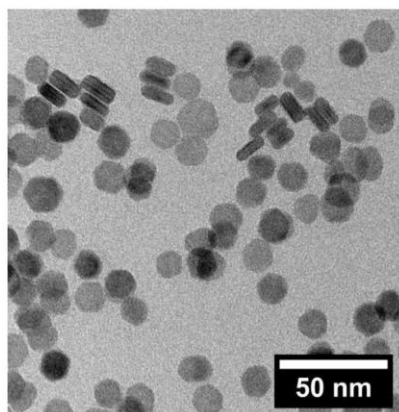


Fig. S4 TEM image of the pure, parent $\text{Cu}_{1.1}\text{S}$ covellite NPs.

Dependence of the extinction cross section on γ

The LSPR frequency (ω_{LSPR}) of both self-doped systems can be described by the Drude model^{1, 2}:

$$\omega_{\text{LSPR}} = \sqrt{\frac{\omega_p^2}{1+2\varepsilon_m} - \gamma^2} \quad (\text{S1})$$

γ is a damping factor that represents the linewidth of the plasmon resonance band and is associated with the frequency of carrier-carrier collisions in the bulk. ε_m is the dielectric constant of the surrounding medium. The bulk plasma frequency (ω_p) can then be derived in relation to the free carrier density (N_h):

$$\omega_p = \sqrt{\frac{N_h e^2}{\varepsilon_0 m_h}} \quad (\text{S2})$$

with m_h being the effective mass of the hole, approximately $0.8 \cdot m_0$. m_0 being the electron mass.^{1, 2} As the LSPR position shifts only slightly, it can be seen that the carrier density, the effective mass of the hole, and the dielectric constant of the surrounding medium are relatively unaltered. For NPs that are small compared to wavelength of the incident light ($\lambda \gg 2R$, R being the NP radius) the extinction cross section (σ_{ext}) of the NPs is only built of the dipole absorption of the Mie equation. Hence the equation is reduced to:

$$\sigma_{\text{ext}}(\omega) = 12\pi \frac{\omega}{c} \varepsilon^{1.5} R^3 \frac{\varepsilon''(\omega)}{[\varepsilon'(\omega) + 2\varepsilon_m]^2 + \varepsilon''(\omega)^2} \quad (\text{S3})$$

$\varepsilon'(\omega)$ and $\varepsilon''(\omega)$ are the real and imaginary part of the dielectric function of the NP. Following equation (S3) the resonance will be at $\varepsilon'(\omega) = -2\varepsilon_m$ if $\varepsilon''(\omega)$ is only weakly dependent on ω or is small.³ Hence the extinction of the plasmon band is mainly dependent on $\varepsilon''(\omega)$, that can be written as:⁴

$$\varepsilon''(\omega) = \frac{\omega_p^2 \gamma}{\omega(\omega^2 + \gamma^2)} \quad (\text{S4})$$

For $\omega \gg \gamma$ this can be approximated with:

$$\varepsilon''(\omega) \approx \frac{\omega_p^2 \gamma}{\omega^3} \quad (\text{S5})$$

From this it can be seen, that at a given plasma frequency the increase of the damping factor leads to an increase of $\varepsilon''(\omega)$ and according to equation (S2) to a decrease of σ_{ext} .

References

- 1 J. M. Luther, P. K. Jain, T. Ewers and A. P. Alivisatos, *Nat Mater*, 2011, **10**, 361-366.
- 2 A. L. Routzahn, S. L. White, L. Fong and P. K. Jain, *Isr. J. Chem.*, 2012, **52**, 983-991.
- 3 S. Link and M. El-Sayed, *J Phys Chem B*, 1999, **103**, 4212-4217.
- 4 C. F. Bohren and D. R. Huffman, *Absorption and scattering of light by small particles*, Wiley, New York [u.a.], 1983.

2.3 Growth of $\text{Cu}_{2-x}\text{Se-CuPt}$ and $\text{Cu}_{1.1}\text{S-Pt}$ Hybrid Nanoparticles

Andreas Wolf, Dominik Hinrichs, Joachim Sann, Jan F. Miethe, Nadja C. Bigall, and Dirk Dorfs

Journal of Physical Chemistry C, 2016, 120, 21925-21931.

Reprinted with permission from Journal of Physical Chemistry C. Copyright 2016 American Chemical Society.

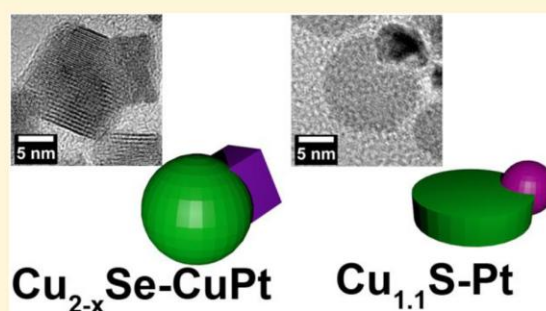
Article DOI: [10.1021/acs.jpcc.6b05574](https://doi.org/10.1021/acs.jpcc.6b05574)

Supporting Information is also available online on the journal's website.

Growth of Cu_{2-x}Se –CuPt and $\text{Cu}_{1.1}\text{S}$ –Pt Hybrid NanoparticlesAndreas Wolf,[†] Dominik Hinrichs,[†] Joachim Sann,[‡] Jan F. Miethel,[†] Nadja C. Bigall,[†] and Dirk Dorfs*[†][†]Institute of Physical Chemistry and Electrochemistry, Leibniz Universität Hannover, Callinstrasse 3A, 30167 Hannover, Germany[‡]Physikalisch-Chemisches Institut, Justus-Liebig-Universität Giessen, Heinrich-Buff-Ring 17, 35392 Giessen, Germany

Supporting Information

ABSTRACT: Copper chalcogenides are the focus of research due to their abundant elements and their low toxicity. In particular, plasmonic Cu_{2-x}Se and $\text{Cu}_{1.1}\text{S}$ NPs represent a main topic of recent research efforts due to the postsynthetic tunability of their localized surface plasmon resonance (LSPR). In this paper, we describe the growth of Cu_{2-x}Se –CuPt and $\text{Cu}_{1.1}\text{S}$ –Pt hybrid nanoparticles. In both systems we investigate the quenching of the LSPR in relation to the Pt ratios. The resulting Cu_{2-x}Se –CuPt hybrid particles form a cubic CuPt domain during the growth process. On the $\text{Cu}_{1.1}\text{S}$ platelets, several, 2–3 nm sized Pt domains are formed. The changes for both systems finally result in a nearly complete damping of the LSPRs. The structural changes of the chalcogenide domain as well as of the metal domain are analyzed in depth and are related to the changes in the LSPRs of the hybrid systems.



1. INTRODUCTION

Localized surface plasmon resonances (LSPRs) in degenerately doped semiconductor nanoparticles (e.g., highly doped metal oxides¹ and several copper chalcogenides^{2–13}) extend the LSPR spectral range known from nanosized metals far into the NIR. Particularly, copper chalcogenides have played an important role in research in the last few years.^{14–18} Nanosized metals (e.g., gold, silver, and platinum) typically exhibit LSPRs in the visible and ultraviolet part of the spectrum. LSPRs with maxima in the NIR can only be achieved with specific shapes,^{19–21} or with very large particles for metals.^{22,23} Also, classical metal based plasmons have been applied in a broad range of applications.^{21,24–26} While the plasmonic properties of classical LSPR NPs are mostly fixed by choice of size, shape, and material, the LSPR in degenerately doped semiconductors can be controlled via the doping degree.^{2,10,27,28} Their small size (as small as 3 nm)¹⁰ compared to classical metals with LSPRs in a similar spectral range allows their potential use in various biological applications, e.g. photothermal therapy²⁹ and male sterilization.³⁰

In recent years, several approaches to modify copper chalcogenide NPs postsynthetically have been reported. Increasing the degree of doping by oxidation and decreasing the degree of doping by Cu(I) or reducing agent addition were just the first steps to tune the LSPR.^{2,10,12,31} Further approaches analyzed the structural and optical changes after the incorporation of miscellaneous cations, such as, e.g. Ag^+ , Zn^{2+} , Cd^{2+} , and Hg^{2+} ,^{27,32,33} or after the growth of Cu_{2-x}Se @ZnS core@shell NPs.³⁴ Furthermore, different approaches to synthesize copper chalcogenide–metal hybrid structures have recently been investigated.^{27,35–39} Several of these structures,

especially various Pt– and CuPt–copper chalcogenide hybrid structures, exhibit enhanced catalytic properties.^{37,40,41}

In this article, we present a simple synthesis method to Cu_{2-x}Se –CuPt and $\text{Cu}_{1.1}\text{S}$ –Pt hybrid NPs. We explore the damping of the LSPR of the pristine copper chalcogenide particles upon the reaction with the platinum precursor, and characterize the morphological and structural changes. Our approach differs from previous copper-chalcogenide–platinum hybrid nanoparticles. Previous reports used Pt–Cu particles that were only subsequently turned to Pt– Cu_{2-x}S by sulfidation.^{37,41} To the best of our knowledge, no Cu_{2-x}Se –CuPt hybrid nanoheterostructures have been reported so far. Additionally, we investigate the changes of the LSPRs of the two starting systems upon formation of the hybrid structures.

2. RESULTS AND DISCUSSION

To obtain quasi-spherical Cu_{2-x}Se starting NPs, we adapted a synthesis previously reported by the Manna group.⁴² The average size of the resulting NPs is 14.7 ± 1.7 nm (Figure S-1). Likewise, the $\text{Cu}_{1.1}\text{S}$ covellite NPs were synthesized by an adapted method from the same group.¹² The resulting nanoplatelets have an average diameter of 12.7 ± 1.7 nm, and a thickness of 5.9 ± 0.7 nm (Figure S-2). Both chalcogenides (Cu_{2-x}Se after 4d exposed to air) exhibit a strong LSPR with a maximum at 1152 nm for Cu_{2-x}Se and 1096 nm for $\text{Cu}_{1.1}\text{S}$. In both systems, the high density of free p-type charge carriers is the cause of the LSPR in the NIR.^{2,10,12}

Received: June 3, 2016

Revised: August 24, 2016

Published: August 24, 2016

In the Cu_{2-x}Se system, the free charge carriers result from copper vacancies, which are created through oxidation.² The metallic covellite system possesses intrinsic valence-band-delocalized holes.^{12,43}

The growth procedure with the Pt precursor leads to the formation of roughly cubic domains on the Cu_{2-x}Se particles, as depicted in Figure 1. For small $\text{Cu}_{2-x}\text{Se}:\text{Pt}$ synthesis-ratios

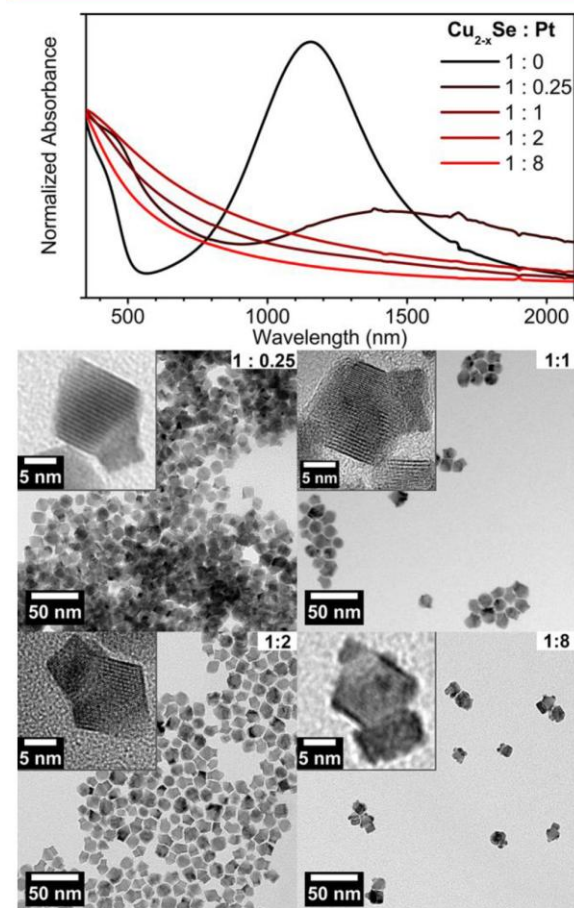


Figure 1. UV/vis/NIR absorption spectra of pristine Cu_{2-x}Se and $\text{Cu}_{2-x}\text{Se}-\text{CuPt}$ samples oxidized under air for 4 d in toluene, and TEM images of the same $\text{Cu}_{2-x}\text{Se}-\text{CuPt}$ samples with Se:Pt ratios of 1:0.25, 1:1, 1:2, and 1:8.

(Se:Pt = 1:0.25, 1:1, and 1:2) most hybrid particles show one cubic domain with higher contrast. A further increase of the platinum amount (1:8) results in the growth of 2–3 small mainly spherical high contrast domains, additional to the larger cubic one. The inset in Figure 1(1:1) shows a typical cubic Pt-containing domain grown on a Cu_{2-x}Se NP. The resulting NPs are stable and can be stored in solution without any changes in morphology.

Contrary to the first expectations, the new domains are not pure Pt but a CuPt alloy, as XRD measurements reveal (Figure 2). The reflex positions at 41.3° (111), 48.1° (200), and 70.5° (222) can be assigned to a fcc CuPt alloy (PDF card #: 01-074-5787). As expected, the relative intensity of these signals increases as the Pt content is increased. Opposed to this trend, the relative intensity of the reflexes which can be assigned to

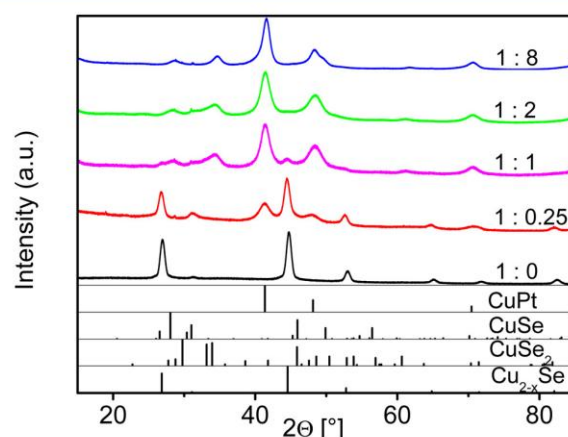


Figure 2. XRD patterns of pristine Cu_{2-x}Se particles (1:0) and of the $\text{Cu}_{2-x}\text{Se}-\text{CuPt}$ hybrid structures with different Se:Pt ratios (1:0.25, 1:1, 1:2, and 1:8). The reference structural data shows fcc Cu_{2-x}Se berzelianite (PDF card #: 01-072-7490), orthorhombic CuSe_2 (PDF card #: 00-019-0400), hexagonal CuSe klockmannite (PDF card #: 03-065-3562), and fcc CuPt (PDF card #: 01-074-5787).

the berzelianite phase (PDF card #: 01-072-7490) decreases. For higher Pt ratios, additional weak reflexes can be detected (especially for 2θ : 28° – 36°). The origin of these is most likely a mixture between an orthorhombic CuSe_2 phase (PDF card #: 00-019-0400) and a hexagonal CuSe klockmannite phase (PDF card #: 03-065-3562). This fact is in agreement with the above-mentioned formation of a CuPt alloy domain, as its formation consumes copper, which reduces the copper content in the starting particles. Hence, we observe a crystallographic change to phases with a lower Cu:Se ratio. Instead of a mixture of these two phases, it is also possible that a metastable phase occurs, which is not uncommon during chemical transformations in nanostructures.¹²

The elemental mapping of these hybrid NPs was done using scanning transmission electron microscopy (STEM) coupled energy dispersive X-ray spectroscopy (EDX) (see Figure 3A). It can be seen that Pt can be found mainly in the higher contrast cubic region, and Se only in the low contrast region of the original NPs. Only low amounts of Pt can be found in the copper selenide part of a few hybrid NPs. This is in agreement

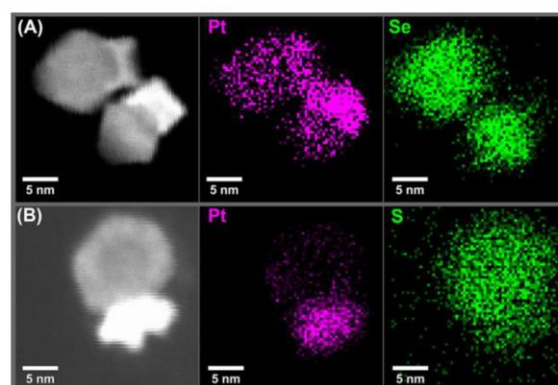


Figure 3. HAADF-STEM images and the corresponding EDX mappings of Pt and Se, respectively S, of $\text{Cu}_{2-x}\text{Se}-\text{CuPt}$ (A) and $\text{Cu}_{1.1}\text{S}-\text{Pt}$ (B).

2 Tuning the LSPR by Metal Growth, Cation Intercalation & Exchange

with the XRD results, which indicate a CuPt phase as well as a mixed copper chalcogenide phase. However, the observed growth behavior is different from the growth of Au domains on Cu_{2-x}Se NPs previously reported by us, where the crystal phase of the original Cu_{2-x}Se NPs was left relatively unaltered.²⁷ We suggest that the reason for this different behavior is harsher reaction conditions at elevated temperatures for the Pt growth, compared to the room temperature growth of Au.

X-ray photoelectron spectroscopy (XPS) analysis of the 1:2 Cu_{2-x}Se -Pt sample is presented in Figure S-5. The Cu 2p spectrum confirms the absence of Cu(II), not only because the Cu 2p_{1/2} and Cu 2p_{3/2} peaks are symmetric and narrow, but also because satellite peaks are absent. Cu(I) and Cu(0) cannot be distinguished with the obtained data. The selenium data indicates that, due to the absence of a signal at higher binding energies, selenium is likely to be present mainly as Se(-II). However, other oxidation states cannot be completely ruled out due to the small expected changes, especially for polyselenides. With the peak being centered at 53.8 eV, the value furthermore is in agreement with literature values for Cu_2Se .⁴⁴ The formation of PtSe_2 would have caused a shift to higher binding energies and can therefore be ruled out. The Pt 4f XPS spectrum shows a split of the Pt 4f_{5/2} and the Pt 4f_{7/2} peaks. These results correlate with the measurements from Han et al. for polyhedral CuPt NPs⁴⁵ and support our interpretation that copper is consumed through the CuPt formation and that the berzelianite structure underwent a phase change to phases with a lower Cu:Se ratio to compensate the copper loss. Especially no indication for Pt intercalation or incorporation in the chalcogenide phases is observed.

The growth of CuPt domains on Cu_{2-x}Se NPs results in a damping of the LSPR (Figure 1). While all samples feature no LSPR before exposure to air (Figure S-3), the pure Cu_{2-x}Se and the 1:0.25 sample develop a LSPR within 4 days after exposure to air. However, the LSPR of the 1:0.25 sample (stored 4 d under air), which is centered at 1450 nm, is weak and bathochromically shifted in comparison to that of the 1:0 sample (Figure 1). Higher Pt amounts completely damp the LSPR. The complete quenching of the LSPR is expected due to the consumption of Cu during the alloy formation, which leads to a complete crystallographic phase change for the hybrid particles with the larger amount of Pt ($\geq 1:1$), as monitored by XRD analysis. For the 1:0.25 sample, however, the reflexes of the berzelianite phase can still be seen in the XRD pattern (Figure 2), which coincides with the still detectable LSPR even though it is already strongly dampened and bathochromically shifted. This damping could be explained either by an already starting crystallographic phase change, or alternatively by electron injecting from the small CuPt domain into the copper selenide part, causing the shift and damping of the free p-type charge carrier based LSPR. Especially the bathochromic shift of the LSPR of the 1:0.25 sample indicates a reduction of free charge carriers in the particles (a simple phase change of parts of the berzelianite to another copper selenide phase should more likely cause only a damping but no shift of the resonance). These findings highlight again the difference of the present system from the previously reported Au- Cu_{2-x}Se hybrid NPs that demonstrated a strong LSPR absorption band caused by the doped semiconductor additional to the gold absorption band.²⁷

The Pt precursor reacts slower with the $\text{Cu}_{1.1}\text{S}$ covellite platelets in comparison to the Cu_{2-x}Se NPs. Only a few small spots of high contrast can be observed on the surface of the

nanoplatelets for smaller Pt amounts (Figure 4(1:0.25)). Only for the highest Pt amount (1:8) after the 150 min reaction time,

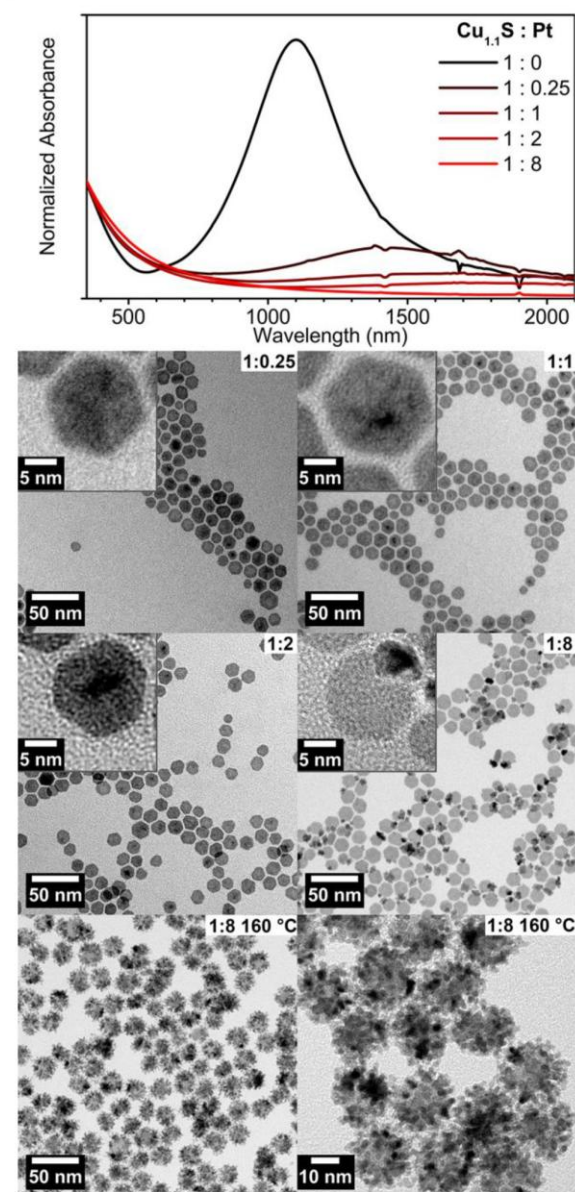


Figure 4. UV/vis/NIR absorption spectra of $\text{Cu}_{1.1}\text{S}$ -Pt samples stored under air for 4 days in toluene and TEM images of $\text{Cu}_{1.1}\text{S}$ -Pt with S:Pt ratios of 1:0.25, 1:1, 1:2, and 1:8 at 130 °C and TEM images of the 1:8 after an additional heating at 160 °C. *The sharp signals at 1400 nm, 1700 nm, and 1900 nm are due to solvent absorption.

can 4–7 nm sized distinct Pt domains be observed (Figure 4(1:8)). These almost exclusively grow on the edge of the platelets. Nearly all platelets exhibit at least one Pt domain. Neither the shape nor size of the $\text{Cu}_{1.1}\text{S}$ starting platelets change significantly during the Pt growth. If the growth temperature of the 1:8 sample is raised after the first growing step at 130–160 °C for an additional 50 min, the shape of the Pt domain changes to form small fringes (Figure 4(1:8) and 4(1:8 at 160 °C)) with a diameter of 2–3 nm. The original

platelet can still be seen in the TEM images under several Pt domains. No sample shows any sign of homogeneous Pt nucleation. These hybrid NPs can be stored in solution without any structural changes. STEM-EDX analysis (Figure 3) of these hybrid NPs demonstrates that Pt can only be found in the high contrast region. Hence, neither significant copper to platinum cation exchange nor a Pt intercalation into the $\text{Cu}_{1.1}\text{S}$ platelets occurs, which is contrary to observations for Au(I) respectively Ag(I).²⁷

The Pt growth on $\text{Cu}_{1.1}\text{S}$ results in a bathochromic shift of the LSPR compared to the starting platelet LSPR (Figure 4), while for the oxidized sample (stored for 4 days under air) with a 1:0.25 Pt ratio a very weak plasmon centered at roughly 1450 nm can be observed, the LSPR decreases and further bathochromically shifts when the Pt ratio is increased. In contrast to the $\text{Cu}_{2-x}\text{Se-CuPt}$ samples (1:0 and 1:2), the $\text{Cu}_{1.1}\text{S-Pt}$ spectra do not significantly change between the absorbance measurement under inert atmosphere (Figure S-4) and after storage under air for 4 days (Figure 4). At a ratio of 1:8, no LSPR can be detected. These changes show a similar tendency to the previously reported changes during cation exchange with Au(I) or the intercalation with Cu(I) and Ag(I).^{12,27} However, in contrast to the previously investigated systems, in the case of Pt(0) growth, a stronger damping is observed already for very small amounts of Pt growth. The near complete LSPR damping for a Pt ratio as small as 1:0.25 is stronger than expected.

XRD analysis shows a difference from the growth of CuPt on Cu_{2-x}Se (Figure 5). The crystallinity of the covellite phase of

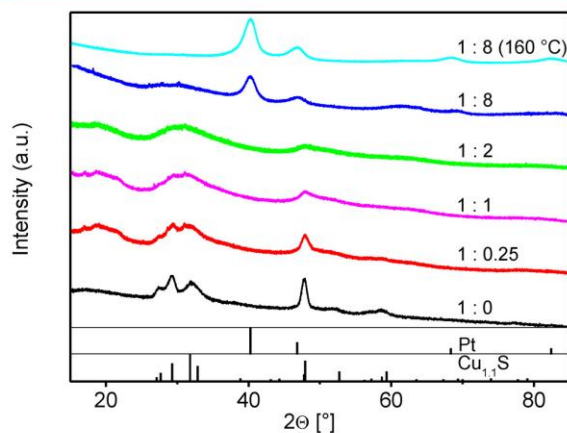


Figure 5. XRD patterns of pristine $\text{Cu}_{1.1}\text{S}$ nanoplatelets (1:0) and of the $\text{Cu}_{1.1}\text{S-Pt}$ hybrid particles with different S:Pt ratios (1:0.25, 1:1, 1:2, 1:8, and 1:8 at 160 °C). The reference structural data shows hexagonal $\text{Cu}_{1.1}\text{S}$ covellite (PDF card #: 00-006-0464) and fcc Pt (PDF card #: 01-087-0647).

the $\text{Cu}_{1.1}\text{S}$ platelets seems to decrease, as no specific reflexes of covellite or other Cu–S phases can be assigned to samples with Pt amounts larger than 0.25 parts. The reflexes rather smear to one broad mixed signal. For the 1:8 sample, new reflexes emerge at 2θ 40.5°, 47°, etc. that can be assigned to pure fcc Pt (PDF card #: 01-087-0647). The fact that no distinct copper sulfide reflexes can be observed for the 1:8 Pt ratio samples, even though they can still be seen in the TEM images (Figure 4(1:8) and (1:8 at 160 °C)), can be explained by the larger

scattering intensity for Pt, and a partial amorphization of the covellite.

XPS data of the 1:2 $\text{Cu}_{1.1}\text{S-Pt}$ sample (Figure S-6) confirms the results of the XRD analysis, where metallic Pt was identified on the $\text{Cu}_{1.1}\text{S}$ platelets. The nonsplit peaks for Pt 4f7/2 and Pt 4f5/2 give no evidence of any Pt–S bonds (as would be expected, if Pt intercalation had occurred). The measured XPS spectrum of the S 2p region does not present significant features that would allow a detailed analysis of the chemical environment of S in this sample. As discussed for the $\text{Cu}_{2-x}\text{Se-CuPt}$ system, no Cu(II) signal can be measured in the Cu 2p region for the $\text{Cu}_{1.1}\text{S-Pt}$ sample either. These results coincide with the findings of a previous report on $\text{Cu}_{1.1}\text{S}$ covellite NPs.¹²

While one could argue that the disappearance of the LSPR for larger Pt amounts is caused by a crystallographic phase change, which would reduce the hole density of the overall particle, this argumentation alone cannot explain the findings for the lower Pt ratios: a drastic, nearly complete damping of the LSPR can be observed, while the covellite structure is mainly unchanged. Combined with the results from XPS (that does not show any signs of Pt intercalation), we suggest that already small amounts of Pt on the nanoplatelets inject electrons into the $\text{Cu}_{1.1}\text{S}$, which causes a reduction of free p-type charge carriers resulting in the observed strong damping of the LSPR. Previous theoretical work on the (0001) covellite surface calculated a work function for the termination with the lowest surface energy of 5.56 eV.⁴⁶ This is in the range of the platinum work function 5.12 eV–5.93 eV (depending on the crystal face).⁴⁷ This strong influence is different from the one observed for the Au– Cu_{2-x}Se system, where we could not see such an electron donation.²⁷ The quenching of the LSPR for larger Pt amounts is therefore most likely a combination of this electron donating effect and the crystallographic change.

In summary, the reactions of the two copper chalcogenide systems with the Pt precursor proceed quite differently. In the berzelianite system an alloy formation takes place, resulting in $\text{Cu}_{2-x}\text{Se-CuPt}$ alloy structures. The covellite system forms $\text{Cu}_{1.1}\text{S-Pt}$ structures. For both systems a continuous disappearance of the starting NPs crystallographic phase can be observed in XRD, which is accompanied by a complete LSPR quenching already for relatively small Pt amounts. For the $\text{Cu}_{1.1}\text{S-Pt}$ system the latter finding allows us to assume that Pt domains can donate a significant amount of electrons to the copper chalcogenide domain, which is contrary to our previous findings of Au domains on Cu_{2-x}Se , which basically did not alter the LSPR in the hybrid nanoparticles.²⁷

3. CONCLUSION

We presented here the growth of Pt containing domains on two copper chalcogenide nanoparticle systems. Particularly, we found that plasmonic quasispherical Cu_{2-x}Se NPs, which were treated with the Pt precursor, kept their original shape, and one or more alloyed CuPt domains grew on the original starting NPs. This growth led to a damping, and, for higher Pt amounts, to a complete disappearance of their LSPR. We assigned this to the complete crystallographic change, which subsequently led to a reduction of the copper vacancies causing the damping of the LSPR. However, especially for the sample with the lowest Pt amounts, we revealed that the crystallographic phase change cannot be the exclusive cause of the strong damping. We assigned this to electron donation from the CuPt domain causing a reduction of free charge carriers in the Cu_{2-x}Se . Additionally we synthesized $\text{Cu}_{1.1}\text{S-Pt}$ hybrid nanoparticles

and observed that the growth was considerably slower. However, solid state characterization showed that no CuPt formed on the original particles, but rather multiple small pure Pt domains. The growth of the Pt domain is also accompanied by a damping, and for larger Pt amounts with a complete loss of the plasmonic properties of the original Cu_{1.1}S platelets. The origin of the damping of this LSPR is most likely a combination of a crystallographic change and of electron injection from the metallic Pt. Overall, we presented a simple approach to synthesize copper chalcogenide platinum hybrid systems.

4. EXPERIMENTAL SECTION

4.1. Materials. Copper(I) chloride (CuCl, 99.99% extra pure) and ethanol (EtOH, 99.5%, extra dry) were purchased from Acros Organics. Selenium (Se, 99.999%, 200 mesh), methanol (MeOH, 99.9%, anhydrous), toluene (99.8%, anhydrous packed under argon), and *n*-butanol (99.9% packed under argon) were purchased from Alfa Aesar. Sulfur (S, 99.98%), octadecene (ODE, 90%), and oleylamine (OLA, > 70%) were purchased from Sigma-Aldrich. Platinum(II) acetylacetonate (Pt(acac)₂, 98%) was purchased from ABCR. Hydrochloric acid (>37%, for trace analysis) and nitric acid (>69%, for trace analysis) were purchased from Fluka.

OLA and ODE are placed each in a separate flask, heated under reflux (115 °C, $\leq 1 \times 10^{-3}$ mbar) for 6 h, while purging several times with argon. The predegassed OLA and ODE are then transferred and stored inside the glovebox under inert gas.

All other chemicals were used without further purification.

All experiments are carried out under argon applying standard Schlenk line techniques, if not stated otherwise.

4.2. Synthesis of Cu_{2-x}Se Nanoparticles. A synthesis method adapted from Deka et al. has been used to produce quasi spherical Cu_{2-x}Se NPs.^{27,42}

The solvent mixture (15 mL ODE and 15 mL OLA) is degassed, under vacuum ($\leq 1 \times 10^{-3}$ mbar), at 115 °C for 3 h. The mixture is cooled to room temperature, and under strong argon flow CuCl (297 mg, 3 mmol) is added. For additional 15 min the mixture is heated to reflux under vacuum. Subsequently, the flask is set under an argon flow, and the temperature is raised rapidly to 300 °C in 5–6 min. The selenium precursor solution is prepared by dispersing Se (117 mg, 1.5 mmol) with predegassed OLA (9 mL), and refluxing it under vacuum for 30 min (115 °C). The mixture is set under a constant argon flow, and is left stirring at 190–200 °C until all Se is dissolved. Upon dissolution, the temperature is raised again to 230 °C for 20 min. To transfer the precursor solution with a glass syringe, the solution is cooled to 150 °C. The Se-solution is then rapidly injected into the copper precursor solution. The reaction mixture is allowed to recover to 290 °C within approximately 2–3 min. The reaction is quenched 15 min after the injection by rapidly cooling it down. At 150 °C toluene (20 mL) is injected to prevent agglomeration. The particles are cleaned by precipitation with EtOH (20 mL) and MeOH (10 mL) and centrifugation (3700g, 20 min). The precipitate is redissolved in toluene (20 mL) by ultrasonication (5 min). After 12 h the solution is centrifuged again (3700g, 20 min), to remove aggregates. The supernatant is collected and used for all further experiments. The final sample has a Cu₂Se concentration of 0.040 mmol/mL according to the elemental analysis (see section 4.6 for details), corresponding to a 53% reaction yield.

4.3. Synthesis of Cu_{1.1}S Nanoplatelets. A method reported by Xie et al. is scaled up to produce Cu_{1.1}S nanoplatelets.^{12,27}

OLA (40 mL), ODE (40 mL), and sulfur (256.5 mg, 8 mL) are placed in a flask and degassed in vacuum ($\leq 1 \times 10^{-3}$ mbar) for 30 min at 120 °C. Subsequently, the flask is set under argon and heated to 130 °C for 5 min. After the solution is cooled to room temperature, CuCl (400 mg, 4 mmol) is added. The flask is evacuated at room temperature for 60 min. With a ramp of 8 °C/min, the temperature is raised to 200 °C and kept at this temperature for 30 min. To quench the reaction, the mixture is rapidly cooled to room temperature. The particles are cleaned by precipitation with EtOH (40 mL) and subsequent centrifugation (3700g, 20 min). The precipitate is redissolved in toluene (28 mL). The solution is centrifuged (100g, 5 min) to remove larger side products. The dark green supernatant is used for all further experiments. The final sample has a Cu_{1.1}S concentration of 0.037 mmol/mL according to the elemental analysis (see section 4.6 for details), corresponding to a 29% reaction yield.

4.4. Growth of Cu_{2-x}Se-CuPt and Cu_{1.1}S-Pt NPs. A typical Se:Pt = 1:8 (respectively S:Pt = 1:8) Pt growth is done inside a 25 mL 3-neck flask. Pt(acac)₂ (50.1 mg, 0.127 mmol), 7.5 mL of predegassed ODE, and 100 μ L of predegassed OLA and chalcogenide NPs in toluene ($n_{\text{Cu}_2\text{Se}} = 0.016$ mmol, respectively, $n_{\text{Cu}_{1.1}\text{S}} = 0.016$ mmol) are mixed together and left stirring under vacuum ($\leq 1 \times 10^{-3}$ mbar) for 30 min at room temperature, and additionally for 30 min at 50 °C. After the flask is set under constant argon flow, the temperature is raised to 130 °C in 7 min. The reaction solution is left stirring for 2.5 h. Samples are taken with a glass syringe, and are quenched directly in a mixture of *n*-butanol (0.5 mL) and EtOH (1.5 mL) per 1.5 mL sample. The particles are precipitated by centrifugation (3700g, 10 min). The particles are redissolved in toluene (1 mL), resulting in a clear, brown solution.

4.5. UV/vis/NIR Absorption Spectroscopy. An Agilent Cary 5000 UV/vis/NIR spectrophotometer was used to record the absorption spectra.

Three milliliters of a diluted sample solution (in toluene) was filled inside the glovebox in a 10 mm path length quartz glass cuvette, sealed, and taken outside the glovebox for measurement. Subsequently, they were left standing exposed to air for 4 days, to measure the oxidized samples.

4.6. Elemental Analysis. Quantitative copper elemental analysis was done by atomic absorption spectroscopy (AAS) using a Varian AA 140 spectrometer. For the sample preparation, the NP solutions were placed in a vial, the toluene was evaporated in vacuum, and the resulting precipitate dissolved in aqua regia (1 part HNO₃ and 3 parts HCl). After several hours, the dissolved sample was diluted with deionized water. The spectrometer was operated at a wavelength of 324.8 nm and with an acetylene air flame.

The NP concentrations were calculated from the determined copper content, assuming a stoichiometric Cu₂Se composition for the unoxidized berzelianite sample (which is reasonable due to the fact that the pristine unoxidized samples were analyzed, which have no LSPR indicating a negligible value of *x*), and a Cu_{1.1}S composition for the covellite system.

4.7. Electron Microscopy. Conventional TEM and HRTEM measurements were carried out using a FEI Tecnai G2 F20, equipped with a field emission gun operated at 200 kV.

For elemental mappings with EDX a JEOL JEM-2100F transmission electron microscope, operated at 200 kV and

equipped with a field emission gun, in scanning electron microscopy mode was used. Copper cannot be reliably mapped due to a high background noise caused by copper pole pieces of the microscope.

Sample preparation was done by placing a carbon coated copper grid (gold grids were used for EDX mappings) purchased from QUANTIFOIL on a filter paper and dropping a diluted particle solution on it.

4.8. Powder X-ray Diffraction Analysis. XRD patterns were recorded at a Bruker D8 Advance, in reflection mode and with a Cu source operating at 40 kV and 40 mA.

Samples were prepared by drying the sample dispersion on a single crystalline silicon sample holder.

4.9. X-ray Photoelectron Spectroscopy. XPS measurements were conducted in a PHI Versaprobe II Scanning ESCA Microprobe (Physical Electronics) using a monochromatized Al K_{α} X-ray source (beam diameter 200 μm , X-ray power of 25 W) equipped with an argon ion gun for sample cleaning and depth profiling. The analyzer pass energy for detail spectra was set to 23.5 eV with a step time of 50 ms and a step size of 0.2 eV. During measurement, the sample was flooded with slow electrons and argon ions using the built-in ion sputter and electron guns in order to compensate surface charging effects. Data evaluation was performed using CasaXPS software. For the charge correction, the energy of the C 1s-line was set to 284.8 eV.

XPS samples were prepared by repeated drop casting (under inert atmosphere) of the sample solutions on a 4×4 mm glass substrate.

■ ASSOCIATED CONTENT

■ Supporting Information

The Supporting Information is available free of charge on the ACS Publications website at DOI: 10.1021/acs.jpcc.6b05574.

TEM images of pristine Cu_{2-x}Se NPs and $\text{Cu}_{1.1}\text{S}$ platelets; UV/vis/NIR absorption spectra of the samples before exposure to air; XPS spectra of the 1:2 Se:Pt Cu_{2-x}Se -CuPt and the 1:2 S:Pt $\text{Cu}_{1.1}\text{S}$ -Pt sample; cyclic voltammograms of the 1:2 Cu_{2-x}Se -CuPt and the 1:2 $\text{Cu}_{1.1}\text{S}$ -Pt sample as well as their discussion and measurement parameters (PDF)

■ AUTHOR INFORMATION

Corresponding Author

*E-mail: dirk.dorfs@pci.uni-hannover.de. Tel.: +49 (511) 762-14440.

Notes

The authors declare no competing financial interest.

■ ACKNOWLEDGMENTS

D.D., A.W., and D.H. are grateful to the German research foundation (DFG) (DFG research Grant DO 1580/3-1 and DO 1580/2-1) and the Volkswagen foundation (lower Saxony/Israel cooperation, Grant ZN2916) for funding. The authors thank the Laboratory of Nano and Quantum Engineering of the Leibniz Universität Hannover. N.C.B. and J.F.M. are grateful for financial support from BMBF NanoMatFutur (support code: 03X5525).

■ REFERENCES

- (1) Lounis, S. D.; Runnerstrom, E. L.; Llordes, A.; Milliron, D. J. Defect Chemistry and Plasmon Physics of Colloidal Metal Oxide Nanocrystals. *J. Phys. Chem. Lett.* **2014**, *5*, 1564–1574.
- (2) Dorfs, D.; Härtling, T.; Miszta, K.; Bigall, N. C.; Kim, M. R.; Genovese, A.; Falqui, A.; Povia, M.; Manna, L. Reversible Tunability of the Near-Infrared Valence Band Plasmon Resonance in Cu_{2-x}Se Nanocrystals. *J. Am. Chem. Soc.* **2011**, *133*, 11175–11180.
- (3) Balitskii, O. A.; Sytnyk, M.; Stangl, J.; Primetzhofer, D.; Groiss, H.; Heiss, W. Tuning the Localized Surface Plasmon Resonance in Cu_{2-x}Se Nanocrystals by Postsynthetic Ligand Exchange. *ACS Appl. Mater. Interfaces* **2014**, *6*, 17770–17775.
- (4) Wang, Y.; Zhukovskiy, M.; Tongying, P.; Tian, Y.; Kuno, M. Synthesis of Ultrathin and Thickness-Controlled Cu_{2-x}Se Nanosheets Via Cation Exchange. *J. Phys. Chem. Lett.* **2014**, *5*, 3608–3613.
- (5) Dilena, E.; Dorfs, D.; George, C.; Miszta, K.; Povia, M.; Genovese, A.; Casu, A.; Prato, M.; Manna, L. Colloidal $\text{Cu}_{2-x}(\text{S}_y\text{Se}_{1-y})$ Alloy Nanocrystals with Controllable Crystal Phase: Synthesis, Plasmonic Properties, Cation Exchange and Electrochemical Lithiation. *J. Mater. Chem.* **2012**, *22*, 13023–13031.
- (6) Saldanha, P. L.; Brescia, R.; Prato, M.; Li, H.; Povia, M.; Manna, L.; Lesnyak, V. Generalized One-Pot Synthesis of Copper Sulfide, Selenide-Sulfide, and Telluride-Sulfide Nanoparticles. *Chem. Mater.* **2014**, *26*, 1442–1449.
- (7) Liu, X.; Wang, X.; Swihart, M. T. $\text{Cu}_{2-x}\text{S}_{1-y}\text{Se}_y$ Alloy Nanocrystals with Broadly Tunable Near-Infrared Localized Surface Plasmon Resonance. *Chem. Mater.* **2013**, *25*, 4402–4408.
- (8) Kriegel, I.; Rodríguez-Fernández, J.; Wisnet, A.; Zhang, H.; Waurisch, C.; Eychmüller, A.; Dubavik, A.; Govorov, A. O.; Feldmann, J. Shedding Light on Vacancy-Doped Copper Chalcogenides: Shape-Controlled Synthesis, Optical Properties, and Modeling of Copper Telluride Nanocrystals with Near-Infrared Plasmon Resonances. *ACS Nano* **2013**, *7*, 4367–4377.
- (9) Li, W.; Zamani, R.; Rivera Gil, P.; Pelaz, B.; Ibanez, M.; Cadavid, D.; Shavel, A.; Alvarez-Puebla, R. A.; Parak, W. J.; Arbiol, J.; et al. CuTe Nanocrystals: Shape and Size Control, Plasmonic Properties, and use as SERS Probes and Photothermal Agents. *J. Am. Chem. Soc.* **2013**, *135*, 7098–7101.
- (10) Luther, J. M.; Jain, P. K.; Ewers, T.; Alivisatos, A. P. Localized Surface Plasmon Resonances Arising from Free Carriers in Doped Quantum Dots. *Nat. Mater.* **2011**, *10*, 361–366.
- (11) Zhao, Y.; Pan, H.; Lou, Y.; Qiu, X.; Zhu, J.; Burda, C. Plasmonic Cu_{2-x}S Nanocrystals: Optical and Structural Properties of Copper-Deficient Copper(I) Sulfides. *J. Am. Chem. Soc.* **2009**, *131*, 4253–4261.
- (12) Xie, Y.; Riedinger, A.; Prato, M.; Casu, A.; Genovese, A.; Guardia, P.; Sottini, S.; Sangregorio, C.; Miszta, K.; Ghosh, S.; et al. Copper Sulfide Nanocrystals with Tunable Composition by Reduction of Covellite Nanocrystals with Cu^+ Ions. *J. Am. Chem. Soc.* **2013**, *135*, 17630–17637.
- (13) Kruszynska, M.; Borchert, H.; Bachmatiuk, A.; Ruemmel, M. H.; Buechner, B.; Parisi, J.; Kolny-Olesiak, J. Size and Shape Control of Colloidal Copper(I) Sulfide Nanorods. *ACS Nano* **2012**, *6*, 5889–5896.
- (14) Comin, A.; Manna, L. New Materials for Tunable Plasmonic Colloidal Nanocrystals. *Chem. Soc. Rev.* **2014**, *43*, 3957–3975.
- (15) Zhao, Y.; Burda, C. Development of Plasmonic Semiconductor Nanomaterials with Copper Chalcogenides for a Future with Sustainable Energy Materials. *Energy Environ. Sci.* **2012**, *5*, 5564–5576.
- (16) Liu, X.; Swihart, M. T. Heavily-Doped Colloidal Semiconductor and Metal Oxide Nanocrystals: An Emerging New Class of Plasmonic Nanomaterials. *Chem. Soc. Rev.* **2014**, *43*, 3908–3920.
- (17) Fauchaux, J. A.; Stanton, A. L. D.; Jain, P. K. Plasmon Resonances of Semiconductor Nanocrystals: Physical Principles and New Opportunities. *J. Phys. Chem. Lett.* **2014**, *5*, 976–985.
- (18) van der Stam, W.; Berends, A. C.; Donega, C. d. M. Prospects of Colloidal Copper Chalcogenide Nanocrystals. *ChemPhysChem* **2016**, *17*, 559–581.

- (19) Murphy, C. J.; Sau, T. K.; Gole, A. M.; Orendorff, C. J.; Gao, J.; Gou, L.; Hunyadi, S. E.; Li, T. Anisotropic Metal Nanoparticles: Synthesis, Assembly, and Optical Applications. *J. Phys. Chem. B* **2005**, *109*, 13857–13870.
- (20) Oldenburg, S. J.; Averitt, R. D.; Westcott, S. L.; Halas, N. J. Nanoengineering of Optical Resonances. *Chem. Phys. Lett.* **1998**, *288*, 243–247.
- (21) Sau, T. K.; Rogach, A. L.; Jaeckel, F.; Klar, T. A.; Feldmann, J. Properties and Applications of Colloidal Nonspherical Noble Metal Nanoparticles. *Adv. Mater.* **2010**, *22*, 1805–1825.
- (22) Zoric, I.; Zaech, M.; Kasemo, B.; Langhammer, C. Gold, Platinum, and Aluminum Nanodisk Plasmons: Material Independence, Subradiance, and Damping Mechanisms. *ACS Nano* **2011**, *5*, 2535–2546.
- (23) Link, S.; El-Sayed, M. Size and Temperature Dependence of the Plasmon Absorption of Colloidal Gold Nanoparticles. *J. Phys. Chem. B* **1999**, *103*, 4212–4217.
- (24) Bardhan, R.; Grady, N. K.; Halas, N. J. Nanoscale Control of Near-Infrared Fluorescence Enhancement using Au Nanoshells. *Small* **2008**, *4*, 1716–1722.
- (25) Sepulveda, B.; Angelome, P. C.; Lechuga, L. M.; Liz-Marzan, L. LSPR-Based Nanobiosensors. *Nano Today* **2009**, *4*, 244–251.
- (26) Jain, P. K.; Huang, X.; El-Sayed, I.; El-Sayed, M. Noble Metals on the Nanoscale: Optical and Photothermal Properties and some Applications in Imaging, Sensing, Biology, and Medicine. *Acc. Chem. Res.* **2008**, *41*, 1578–1586.
- (27) Wolf, A.; Kodanek, T.; Dorfs, D. Tuning the LSPR in Copper Chalcogenide Nanoparticles by Cation Intercalation, Cation Exchange and Metal Growth. *Nanoscale* **2015**, *7*, 19519–19527.
- (28) Kanehara, M.; Koike, H.; Yoshinaga, T.; Teranishi, T. Indium Tin Oxide Nanoparticles with Compositionally Tunable Surface Plasmon Resonance Frequencies in the Near-IR Region. *J. Am. Chem. Soc.* **2009**, *131*, 17736–17737.
- (29) Hessel, C. M.; Pattani, V. P.; Rasch, M.; Panthani, M. G.; Koo, B.; Tunnell, J. W.; Korgel, B. A. Copper Selenide Nanocrystals for Photothermal Therapy. *Nano Lett.* **2011**, *11*, 2560–2566.
- (30) Liu, Z.; Liu, X.; Du, Y.; Ren, J.; Qu, X. Using Plasmonic Copper Sulfide Nanocrystals as Smart Light-Driven Sterilants. *ACS Nano* **2015**, *9*, 10335–10346.
- (31) Krieger, I.; Jiang, C.; Rodriguez-Fernandez, J.; Schaller, R. D.; Talapin, D. V.; da, C.; Enrico, Feldmann, J. Tuning the Excitonic and Plasmonic Properties of Copper Chalcogenide Nanocrystals. *J. Am. Chem. Soc.* **2012**, *134*, 1583–1590.
- (32) Lesnyak, V.; Brescia, R.; Messina, G. C.; Manna, L. Cu Vacancies Boost Cation Exchange Reactions in Copper Selenide Nanocrystals. *J. Am. Chem. Soc.* **2015**, *137*, 9315–9323.
- (33) Xie, Y.; Bertoni, G.; Riedinger, A.; Sathya, A.; Prato, M.; Marras, S.; Tu, R.; Pellegrino, T.; Manna, L. Nanoscale Transformations in Covellite (CuS) Nanocrystals in the Presence of Divalent Metal Cations in a Mild Reducing Environment. *Chem. Mater.* **2015**, *27*, 7531–7537.
- (34) Wolf, A.; Haertling, T.; Hinrichs, D.; Dorfs, D. Synthesis of Plasmonic Cu_{2-x}Se@ZnS Core@Shell Nanoparticles. *ChemPhysChem* **2016**, *17*, 717–723.
- (35) Motl, N. E.; Bondi, J. F.; Schaak, R. E. Synthesis of Colloidal Au-Cu₂S Heterodimers Via Chemically Triggered Phase Segregation of AuCu Nanoparticles. *Chem. Mater.* **2012**, *24*, 1552–1554.
- (36) Ding, X.; Liow, C. H.; Zhang, M.; Huang, R.; Li, C.; Shen, H.; Liu, M.; Zou, Y.; Gao, N.; Zhang, Z.; et al. Surface Plasmon Resonance Enhanced Light Absorption and Photothermal Therapy in the Second Near-Infrared Window. *J. Am. Chem. Soc.* **2014**, *136*, 15684–15693.
- (37) Ding, X.; Zou, Y.; Ye, F.; Yang, J.; Jiang, J. Pt-CuS Heterodimers by Sulfidation of CuPt Alloy Nanoparticles and their Selective Catalytic Activity Toward Methanol Oxidation. *J. Mater. Chem. A* **2013**, *1*, 11880–11886.
- (38) Liu, X.; Lee, C.; Law, W.; Zhu, D.; Liu, M.; Jeon, M.; Kim, J.; Prasad, P. N.; Kim, C.; Swihart, M. T. Au-Cu_{2-x}Se Heterodimer Nanoparticles with Broad Localized Surface Plasmon Resonance as Contrast Agents for Deep Tissue Imaging. *Nano Lett.* **2013**, *13*, 4333–4339.
- (39) Naskar, S.; Schlosser, A.; Miethe, J. F.; Steinbach, F.; Feldhoff, A.; Bigall, N. C. Site-Selective Noble Metal Growth on CdSe Nanoplatelets. *Chem. Mater.* **2015**, *27*, 3159–3166.
- (40) Yu, X.; Shavel, A.; An, X.; Luo, Z.; Ibanez, M.; Cabot, A. Cu₂ZnSnS₄-Pt and Cu₂ZnSnS₄-Au Heterostructured Nanoparticles for Photocatalytic Water Splitting and Pollutant Degradation. *J. Am. Chem. Soc.* **2014**, *136*, 9236–9239.
- (41) Sang, W.; Zheng, T.; Wang, Y.; Li, X.; Zhao, X.; Zeng, J.; Hou, J. G. One-Step Synthesis of Hybrid Nanocrystals with Rational Tuning of the Morphology. *Nano Lett.* **2014**, *14*, 6666–6671.
- (42) Deka, S.; Genovese, A.; Zhang, Y.; Miszta, K.; Bertoni, G.; Krahne, R.; Giannini, C.; Manna, L. Phosphine-Free Synthesis of P-Type Copper(I) Selenide Nanocrystals in Hot Coordinating Solvents. *J. Am. Chem. Soc.* **2010**, *132*, 8912–8914.
- (43) Xie, Y.; Carbone, L.; Nobile, C.; Grillo, V.; D'Agostino, S.; Della Sala, F.; Giannini, C.; Altamura, D.; Oelsner, C.; Kryschi, C.; et al. Metallic-Like Stoichiometric Copper Sulfide Nanocrystals: Phase- and Shape-Selective Synthesis, Near-Infrared Surface Plasmon Resonance Properties, and their Modeling. *ACS Nano* **2013**, *7*, 7352–7369.
- (44) Cahen, D.; Ireland, P. J.; Kazmerski, L. L.; Thiel, F. A. X-Ray Photoelectron and Auger Electron Spectroscopic Analysis of Surface Treatments and Electrochemical Decomposition of Copper Indium Selenide (CuInSe₂) Photoelectrodes. *J. Appl. Phys.* **1985**, *57*, 4761–71.
- (45) Han, L.; Cui, P.; He, H.; Liu, H.; Peng, Z.; Yang, J. A Seed-Mediated Approach to the Morphology-Controlled Synthesis of Bimetallic Copper-Platinum Alloy Nanoparticles with Enhanced Electrocatalytic Performance for the Methanol Oxidation Reaction. *J. Power Sources* **2015**, *286*, 488–494.
- (46) Gaspari, R.; Manna, L.; Cavalli, A. A Theoretical Investigation of the (0001) Covellite Surfaces. *J. Chem. Phys.* **2014**, *141*, 044702/1–044702/9.
- (47) Lide, D. R., Ed. *CRC Handbook of Chemistry and Physics*, Internet Version 2005; CRC Press: Boca Raton, FL, 2005.

Supporting Information

Growth of $\text{Cu}_{2-x}\text{Se-CuPt}$ and $\text{Cu}_{1.1}\text{S-Pt}$ Hybrid

Nanoparticles

Andreas Wolf,[†] Dominik Hinrichs,[†] Joachim Sann,[‡] Jan F. Miethe[†], Nadja C. Bigall[†] and Dirk Dorfs^{*†}

[†] Institute of Physical Chemistry and Electrochemistry, Leibniz Universität Hannover, Callinstr. 3A, 30167 Hannover, Germany

[‡] Physikalisch-Chemisches Institut, Justus-Liebig-Universität Giessen, Heinrich-Buff-Ring 17, 35392 Giessen, Germany

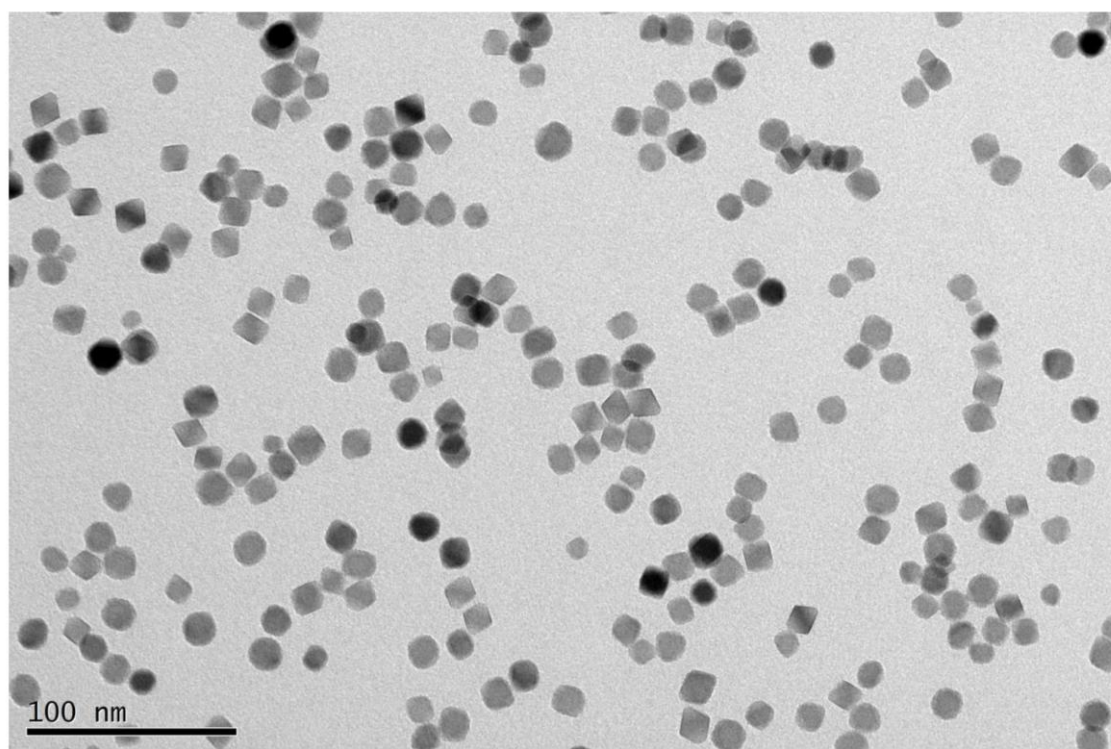


Figure S-1. TEM image of pristine Cu_{2-x}Se NPs.

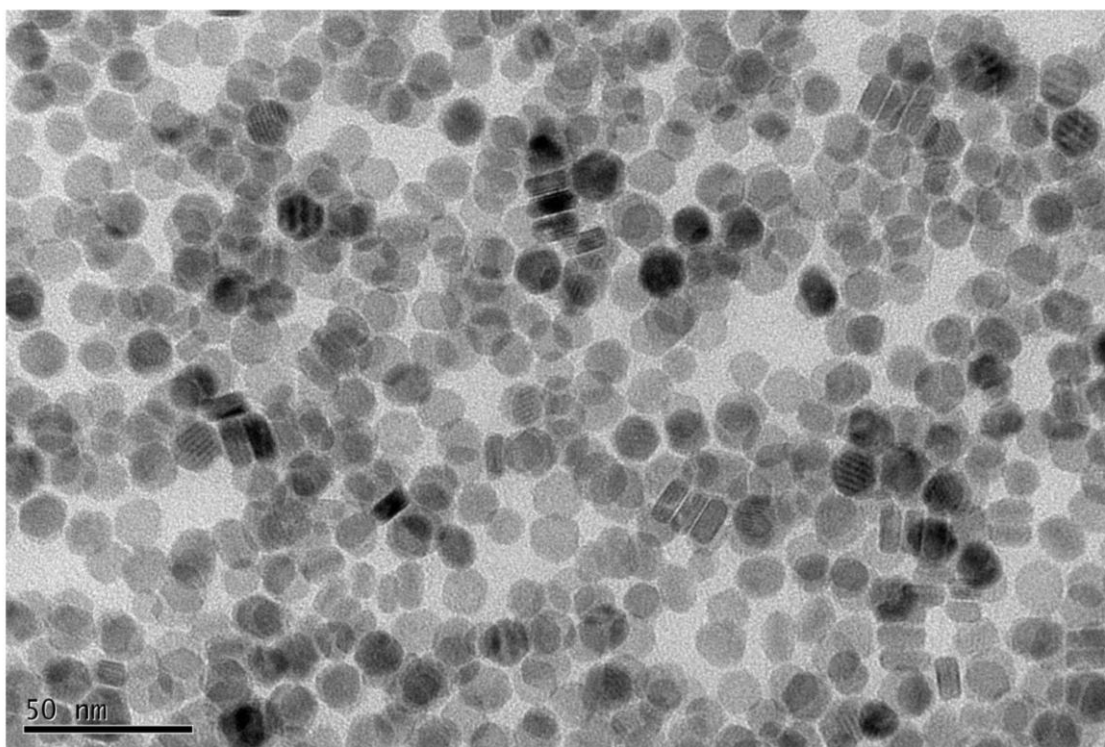


Figure S-2. TEM image of pristine Cu_{1.1}S platelets.

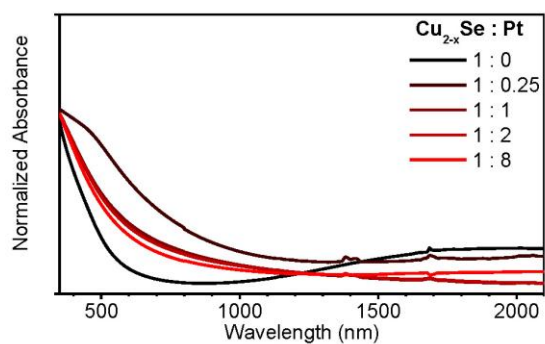


Figure S-3: UV/vis/NIR absorption spectra of pristine Cu_{2-x}Se and Cu_{2-x}Se-CuPt samples before air exposure in toluene, with Se:Pt ratios of 1:0.25, 1:1, 1:2 and 1:8.

2 Tuning the LSPR by Metal Growth, Cation Intercalation & Exchange

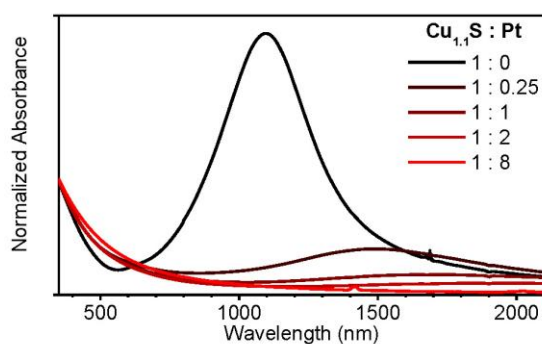


Figure S-4: UV/vis/NIR absorption spectra of Cu_{1.1}S-Pt samples before air exposure in toluene and with S:Pt ratios of 1:0.25, 1:1, 1:2 and 1:8.

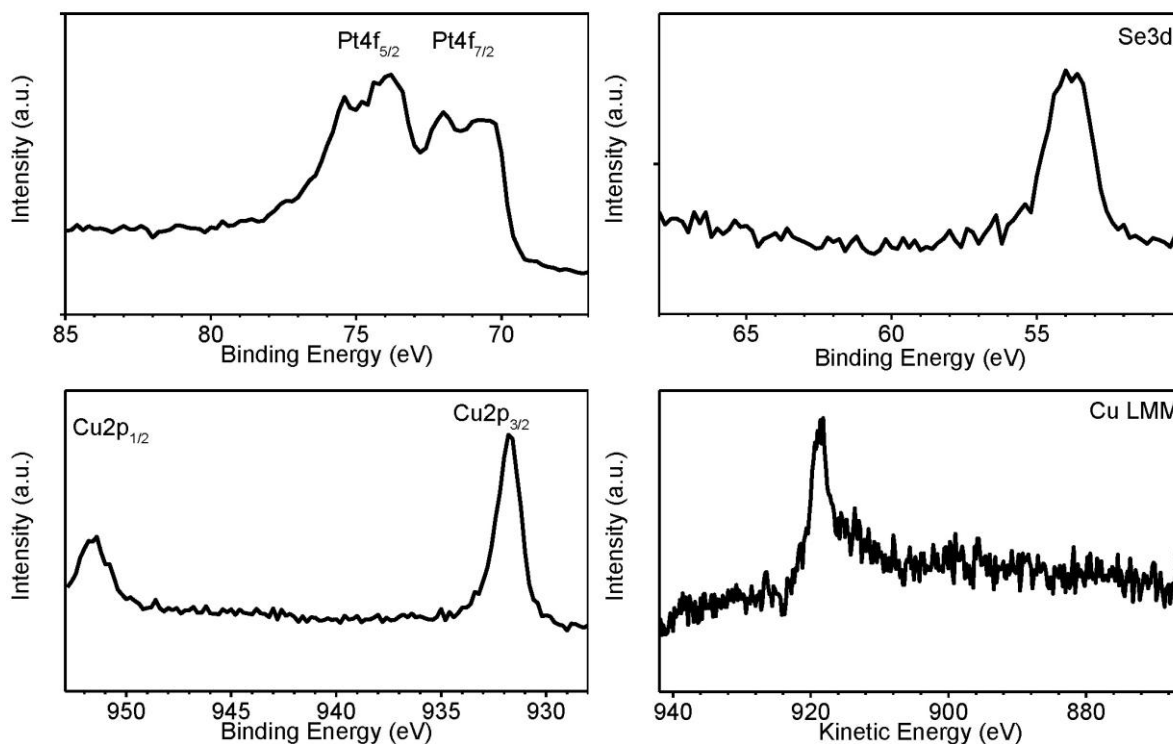


Figure S-5: XPS spectra of the Pt4f, the Se3d and the Cu2p regions from the Cu_{2-x}Se-CuPt sample with a 1:2 Se:Pt ratio. Furthermore the Cu LMM Auger spectrum of the same sample.

2 Tuning the LSPR by Metal Growth, Cation Intercalation & Exchange

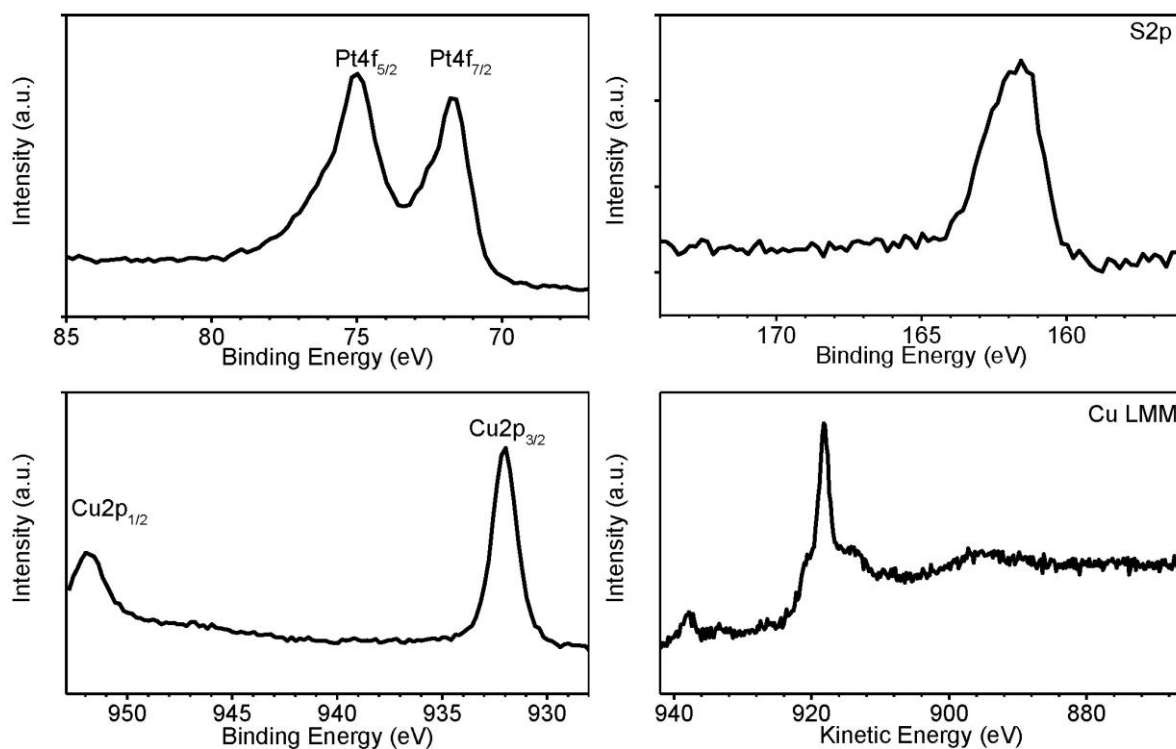


Figure S-6: XPS spectra of the Pt4f, the S2p and the Cu2p regions from the $\text{Cu}_{1.1}\text{S-Pt}$ sample with a 1:2 S:Pt ratio. Furthermore the Cu LMM Auger spectrum of the same sample.

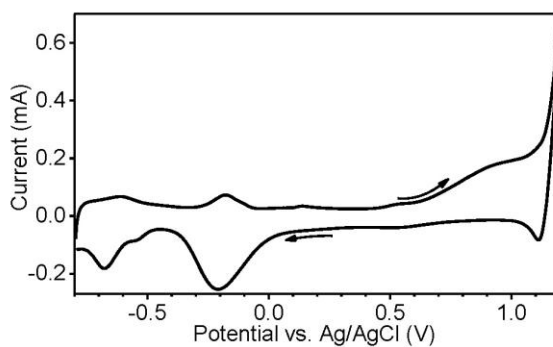


Figure S-7: Cyclic voltammogram of the $1:2 \text{Cu}_{2-x}\text{Se-CuPt}$ sample.

2 Tuning the LSPR by Metal Growth, Cation Intercalation & Exchange

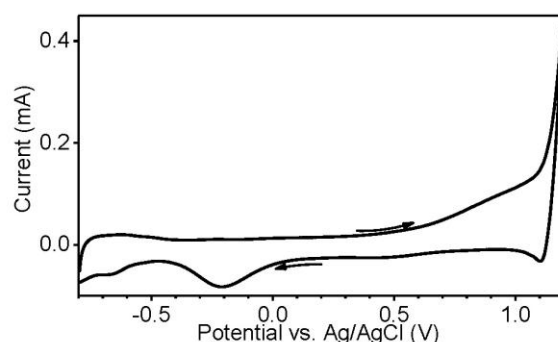


Figure S-8: Cyclic voltammogram of the 1:2 $\text{Cu}_{1.1}\text{S}$ -Pt sample.

The cyclic voltammetry (CV) analysis of the 1:2 Cu_{2-x}Se -CuPt sample in figure S-7 exhibits an anodic peak at -610 mV that is likely due to the oxidation of Cu(I) to Cu(II), and one at -170 mV that originates from the oxidation of Cu(0) to Cu(II). The broad peak for potentials higher than 640 mV can be assigned to the oxidation of the selenide. The weak signal at 460 mV for the back sweep, is likely the response from the PtO_2 reduction to PtO and Pt. Thin layers of PtO_2 can form on Pt electrodes under air. The strong signal at -207 mV can be assigned to the reduction of Cu(II) to Cu(0). The multiple shoulders below -500 mV for the back sweep is probably caused by hydrogen formation on platinum and its desorption. The 1:8 130°C $\text{Cu}_{1.1}\text{S}$ -Pt sample exhibits similar features. However, the Cu(0) oxidation peaks are less pronounced. The broad band above 550 mV for the forward sweep can be attributed to the oxidation of the S(-II). The voltammograms for both samples show the elements that are expected from the sample composition, Cu(I) cannot be detected, because it disproportionates in aqueous solutions.

ESI EXPERIMENTAL SECTION:

Cyclic Voltammetry.

The CV was measured with a ModuLab potentiostat (Solartron Analytical). The voltammograms were recorded with a 100 mV/s sweep speed between -800 mV to 1200mV vs. Ag/AgCl reference electrode. As counter electrode a platinum wire was used. The working electrode was prepared by drop casting the sample on a glassy carbon electrode, and measured in an aqueous 0.1 M potassium nitrate solution.

3 Encapsulation of Cu_{2-x}Se in a Closed ZnS Shell

3.1 Summary

As already discussed, plasmonic Cu_{2-x}Se NPs are considerable sensitive to their environment. On the one hand, this is based on the influence of the dielectric environment on the LSPR (as discussed in chapter 1.3), and on the other hand, on the influence of oxidative and reductive compounds that cause a shift of its resonance band maximum. This fact represents an advantage since the LSPR can be tuned as needed, but at the same time it can be a challenge when stable NPs with a fixed plasmon are needed for example in biological applications such as photo thermal therapy. A typical method in colloidal nanotechnology to achieve the shielding of a core material from its surrounding medium, is the growth of a shell composed of a different material to protect its properties.

Chapter 3.2 explores the growth of protective ZnS shells on Cu_{2-x}Se NPs, and characterizes the properties of the resulting Cu_{2-x}Se@ZnS core@shell particles. The chapter describes the thickness-controlled growth of homogeneous, closed and crystalline ZnS shells. The synthesis was designed with the requirement to avoid Zn²⁺ cation exchange into the core Cu_{2-x}SeNP. This was achieved first, by starting from Cu_{2-x}Se NPs with no or little copper vacancies, and second by choosing a reaction medium free of phosphines. The solid state characterization, comprising high resolution electron microscopy and XRD, showed high crystallinity of the shells, and no changes to the core material. The optical characterization further showed that the core particles can still be oxidized under air. However, this process is considerably slowed down through the ZnS shells from a few hours to several days. In contrast to the oxidation, the ZnS shell successfully suppressed the reduction of the Cu_{2-x}Se core,

3 Encapsulation of Cu_{2-x}Se in a Closed ZnS Shell

even when exposed to strong reducing agents such as BTB and DIBAL. Hence, this is proving the protection of the core NP from the environment by the shell. Moreover, measured absorbance spectra are compared with electrodynamic simulations for the studied core@shell NPs, exhibiting a smaller bathochromic shift for the measurements compared to the simulations. This was explained by deviating oxidation states (values of x) of the Cu_{2-x}Se core for the real samples. The chapter shows a synthetic method enabling the shielding of plasmonic Cu_{2-x}Se NPs from the surrounding environment.

3.2 Synthesis of Plasmonic Cu_{2-x}Se@ZnS Core@Shell Nanoparticles

Andreas Wolf, Thomas Härtling, Dominik Hinrichs and Dirk Dorfs

ChemPhysChem 2016, **17**, 717-723.

Reprinted with permission from ChemPhysChem. Copyright 2016 John Wiley and Sons.

DOI: [10.1002/cphc.201500907](https://doi.org/10.1002/cphc.201500907)

Supporting Information is also available online on the journal's website.

Synthesis of Plasmonic Cu_{2-x}Se@ZnS Core@Shell Nanoparticles

Andreas Wolf,^[a] Thomas Härtling,^[b] Dominik Hinrichs,^[a] and Dirk Dorfs^{*[a]}

We report the synthesis of plasmonic Cu_{2-x}Se@ZnS core@shell nanoparticles (NPs). We used a shell growth approach, starting from Cu_{2-x}Se NPs that have been shown before to exhibit a localized surface plasmon resonance (LSPR). By careful synthesis planning we avoided cation exchange reactions and received core@shell nanoparticles that, after oxidation under air, exhibit a strong LSPR in the NIR. Interestingly, the crystalline, closed

ZnS shell that we grew with variable thickness still allowed a slow oxidation of the core under ambient conditions, while the core was effectively protected from reduction, even in the presence of reducing agents such as borane tert-butylamine complex and diisobutylaluminum hydride, giving rise to a stable particle LSPR, also under strongly reducing conditions.

1. Introduction

The field of nanoplasmonics was enriched in recent years by metal chalcogenide and metal oxide nanoparticles (NPs) that exhibit localized surface plasmon resonances (LSPRs).^[1–5] These materials are specifically interesting, as they add a new method to the control over the LSPR via controlled doping. Typical plasmonic metals (e.g. Au and Ag) can be tuned only in a limited way, and mainly in the synthesis stage by choice of material, size and shape.^[6–10] Nonetheless these particles have found their way into many kinds of applications.^[9,10] However due to the high charge carrier density in metals, LSPRs in the near-infrared (NIR) spectral region can only be reached by very large particles or shape control.^[7,8] For optical-biological applications especially the spectral region 1000–1350 nm, the second biological window, is interesting due to its high maximum permissible exposure to laser and larger penetration depth.^[11] The new classes of plasmonic NP materials show advantages over the classical ones in this spectral region. Plasmon bands in the NIR have been observed for relatively small NPs (as small as 3 nm^[2]) which is important for biological applications that require the particles to be in a size regime of 10–100 nm.^[12] More importantly however they allow the positioning of the LSPR band due to control over the dopant concentration, especially in case of degenerately doped copper chalcogenides also post synthetically.^[1,2] This on the one hand was achieved by self-doping, but also due to controlled, post syn-

thetic, partial cation exchange that enables the positioning of the LSPR maximum to a desired wavelength.^[13]

The growth of shell-on-core nanoparticles is an efficient technique in the design of nanoparticle structures to modify and stabilize their properties.^[14,15] For plasmonic NPs, the shell growth gives a further addition to being only a plain protective coating. Due to the different dielectric constant of the shell medium with respect to the solvent, the LSPR band of metallic NPs can be shifted when a shell is grown due to its high sensitivity to the dielectric environment.^[16,17]

In this work we show the growth of homogeneous, closed and crystalline ZnS shells on plasmonic Cu_{2-x}Se NPs. We characterize the resulting plasmonic core-shell structures structurally and optically. So far, work in this area is limited. One approach to synthesize copper chalcogenide–zinc chalcogenide heterostructures is cation exchange from the plasmonic copper chalcogenides to the corresponding heterostructure. Lesnyak et al. used cation exchange to Janus-like Cu₂Se–ZnSe NPs to show the influence of copper vacancies on cation exchange, however resulting in non-plasmonic structures.^[18] Ha et al. exchanged Cu_{1.81}S NPs to a disc-like Cu_{1.94}S that was “sandwiched” between ZnS, observing a continuous bathochromic shift of the LSPR, accompanied by a strong decrease of the plasmon intensity (due to decrease of carrier concentration and increase of the dielectric constant of the surrounding medium).^[19] Our approach is different to these works, as we avoid cation exchange due to choice of reaction conditions. Other reports use plasmonic Cu_{1.94}S platelets as seeds and grow ZnS in between these particles resulting in a sandwich-like architecture with ZnS growing in between two Cu_{1.94}S discs, resulting in a hypsochromic shift for longer reaction times.^[20] Others however observe a bathochromic shift when growing ZnS antennas out of Cu_{1.94}S NPs^[21] or use a one pot approach to grow Cu_{1.94}S–ZnS and Cu_{1.94}S–ZnS–Cu_{1.94}S heterostructures that however lose all plasmonic features for higher reaction times. Only one work describes the growth of a ZnS shell on photoluminescent, non

[a] A. Wolf, D. Hinrichs, Dr. D. Dorfs
Institute of Physical Chemistry and Electrochemistry
Leibniz University Hannover
Callinstr. 3 A, 30167 Hannover (Germany)
E-mail: dirk.dorfs@pci.uni-hannover.de

[b] Dr. habil. T. Härtling
Fraunhofer Institute for Ceramic Technologies and Systems IKTS
Maria-Reiche-Str. 2, 01109 Dresden (Germany)

Supporting Information for this article is available on the WWW under <http://dx.doi.org/10.1002/cphc.201500907>.

An invited contribution to a Special Issue on Beyond Quantum Dots

plasmonic CuSe core NPs however without any structural characterization of the ZnS shell.^[22]

The work presented here is—to the best of our knowledge—the first approach to grow a closed, crystalline ZnS shell around a plasmonic copper chalcogenide core that furthermore leaves the core unaltered. We analyze the particle properties under oxygen exposure and upon exposure to reducing agents [borane tert-butylamine complex (BTB) and diisobutylaluminum hydride (DIBAL)]. We further compare the observed optical (especially plasmonic) properties to electrodynamic simulations by means of the multiple-multipole (MMP) method. We also show the successful water transfer of the $\text{Cu}_{2-x}\text{Se}@ZnS$ core@shell NPs with polyvinylpyrrolidone (PVP) as well as with 3-mercaptopropionic acid (MPA).

2. Results and Discussion

Quasispherical Cu_{2-x}Se NPs were fabricated adapting a hot-injection synthesis strategy previously reported by Deka et al.^[23] We grew thickness-controlled and homogeneous ZnS shells on these Cu_{2-x}Se core particles, while preserving their plasmonic properties.

The reaction was performed in a reaction medium free of phosphines to avoid cation exchange. Previous studies have shown that phosphines, as a soft base, bind stronger to the Cu^+ cation (a soft acid) than to the Zn^{2+} ion due to the lone pair electrons of P. This promotes the cation exchange from Cu^+ to Zn^{2+} .^[24,25] Choosing oleylamine (OLA) and trioctylphosphine oxide (TOPO; no lone-pair) as solvents and avoiding phosphines in the synthesis is hence necessary to promote the growth of an additional shell while avoiding cation exchange. A further synthesis design approach to suppress cation exchange is the use of Cu_{2-x}Se core particles with a low or no copper vacancies, as Lesnyak et al. have shown that copper va-

cancies are promoting cation exchange to ZnSe at room temperature.^[18] To avoid this, all steps leading to shell growth have been carried out avoiding any exposure to oxygen of the previously synthesized core NPs. The precursor combination, bis(trimethylsilyl) sulfide ($(\text{TMS})_2\text{S}$) and diethyl zinc (ZnEt_2), was selected for their high reactivity, to promote ZnS formation before cation exchange. The precursors were further added in parallel with separate syringes in high dilution (1:40) and slow (7.9 mL h^{-1}) in order to keep the ion concentration in the reaction media low. This avoids homogeneous nucleation of ZnS and reduces the availability of free Zn^{2+} ions for a possible cation exchange.

The precursor is added via a syringe pump to the seed particles in OLA and TOPO at a reaction temperature of 160°C , which was reduced to 90°C after full addition.

Figures 1A,B show transmission electron microscopy (TEM) and high-resolution TEM (HRTEM) images of $\text{Cu}_{2-x}\text{Se}@ZnS$ core@shell particles with two different-sized ZnS shells. In the TEM images, the shells can clearly be distinguished from the core as the lower contrast media. It can be seen that the shell thickness is homogeneous and completely closed. Figure 2 shows the size histogram (analyzing more than 330 NPs for each sample) for the core and both core@shell NPs. The core Cu_{2-x}Se NPs have an average size of 13.1 nm with a standard deviation (SD) of 1.5 nm. The average size increases for the core@shell samples to 16.1 nm (thin shell) and 17.5 nm (thick shells), however accompanied by a small increase of the SD to 1.7 nm (2.0 nm, respectively), which corresponds to the growth of a 1.5 nm (2.2 nm, respectively) shell thickness. These results correlate well with the 1.5 and 2.5 nm shell thicknesses that were calculated for a 100% reaction yield. Increasing the amount of precursor added further did not result in thicker shells. For synthesis with calculated shell thicknesses up to 2.5 nm, no homogeneous nucleation of ZnS NPs was observed

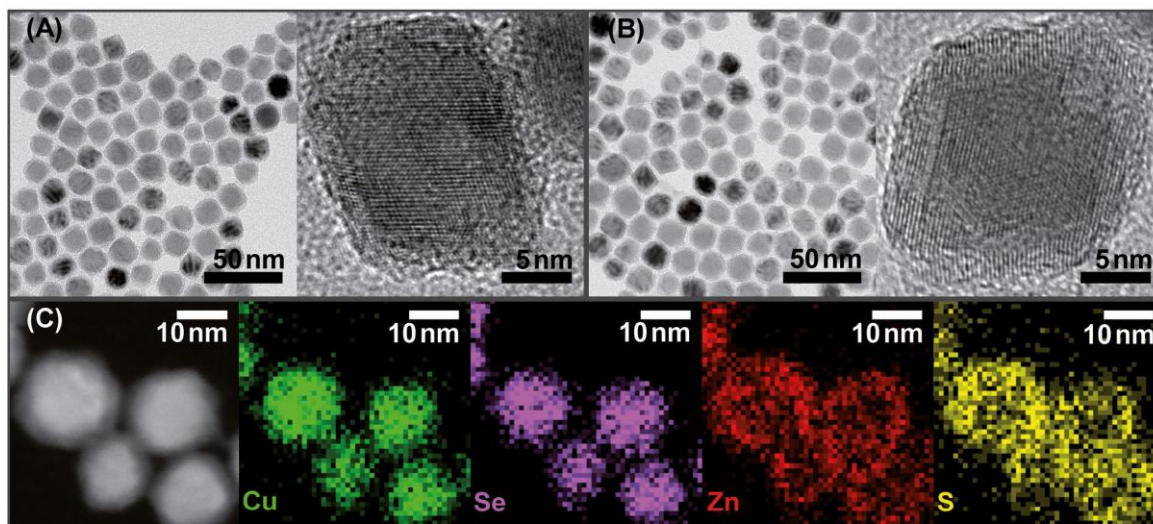


Figure 1. TEM and HRTEM images of the $\text{Cu}_{2-x}\text{Se}@ZnS$ thin-shell (panel A) and $\text{Cu}_{2-x}\text{Se}@ZnS$ thick-shell (panel B) core@shell NPs. Panel C shows HAADF-STEM and corresponding elemental mappings of the same area of the $\text{Cu}_{2-x}\text{Se}@ZnS$ (thick shell) NPs for Cu, Se, Zn, and S.

3 Encapsulation of Cu_{2-x}Se in a Closed ZnS Shell

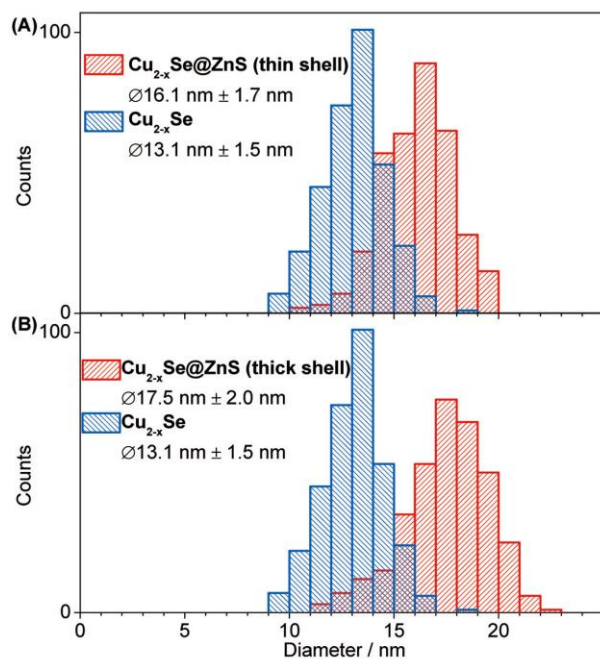


Figure 2. Size histogram from both $\text{Cu}_{2-x}\text{Se}@ZnS$ shell thicknesses compared to plain Cu_{2-x}Se core NPs. For each sample, more than 330 NPs have been analyzed.

(Figure 1A,B). HRTEM images (Figure 1A,B) of the core@shell samples show that the grown ZnS shell is crystalline. Dislocations of the lattice planes can be seen at the phase boundary. It is likely that ZnS did grow non-epitaxially on the core NPs, considering that the lattice mismatch between berzelianite ($a = 5.729 \text{ \AA}$) and ZnS zinc blend ($a = 5.400 \text{ \AA}$) is 5.7%.

Figure 1C shows elemental mapping for the $\text{Cu}_{2-x}\text{Se}@ZnS$ (thick shell) sample. It was measured by energy-dispersive X-ray spectroscopy (EDX) in the scanning mode of the TEM (STEM). It can be seen that copper and selenium are only detected in the higher contrast core of the core@shell NPs. Hence the formation of a Cu–Zn alloy shell cannot be observed. Zinc and sulfur however are found within the boundaries of the entire core@shell NPs. This shows that a shell covering the whole NP was grown and not only a crown. It is important to note that the TEM characterization shows a closed ZnS shell without any holes.

X-ray diffraction (XRD) reveals that during the growth process, the *fcc* berzelianite phase (PDF card #: 01-072-7490) of the Cu_{2-x}Se core does not change (Figure 3). With increasing shell thickness, the appearance of a second phase can be observed, with the most pronounced reflex being at 2θ 47.3° . Due to the low intensity, the high broadening of the reflexes and the similarity between the cubic ZnS zinc blend (PDF card #: 03-065-0309) and the hexagonal ZnS wurtzite (PDF card #: 01-079-2204) XRD patterns for nanostructures, a definite phase identification is not possible for the ZnS shell. However as strong reflexes of the wurtzite phase cannot be detected (e.g. 2θ 51.7°), it is likely that the shell exhibits a zinc blend struc-

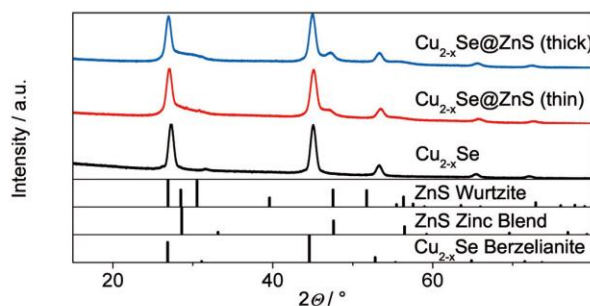


Figure 3. XRD pattern of pristine Cu_{2-x}Se core NPs and $\text{Cu}_{2-x}\text{Se}@ZnS$ core@shell NPs with thin and thick shells. The reference structural data shows *fcc* Cu_{2-x}Se berzelianite (PDF card #: 01-072-7490), *fcc* ZnS zinc blend (PDF card #: 03-065-0309), and hexagonal ZnS wurtzite (PDF card #: 01-079-2204).

ture which would also be reasonable due to the fact that this phase would have the same anion lattice symmetry as the Cu_{2-x}Se host lattice.

Figure 4 shows the absorbance spectra of Cu_{2-x}Se and $\text{Cu}_{2-x}\text{Se}@ZnS$ NPs. The pristine core Cu_{2-x}Se NPs (Figure 4A) exhibit only a very weak absorbance in the NIR, with a maximum above 2000 nm before they are exposed to air. This shows the low amount of copper vacancies in the NPs, corresponding to an x -value close to zero. After oxygen exposure, the maximum shifts hypsochromically, accompanied by a strong increase of the intensity. After seven days exposed to air, the absorbance shows a maximum at around 1040 nm. The absorbance band in the NIR is caused due to a high density of free p-type charge carries in the degenerately self-doped NPs that lead to the development of the LSPR.^[1] The higher x -value indicates a higher number of copper vacancies in the oxidized NPs, which cause the LSPR through the collective oscillation of holes. The as-synthesized $\text{Cu}_{2-x}\text{Se}@ZnS$ core-shell particles also exhibit a very weak LSPR absorbance band with a maximum above 2000 nm before air exposure (Figure 4B,C). This, similar to the core NPs, shifts hypsochromically, and the intensity increases until it shows a maximum at around 1050 nm for the thin ZnS shell NPs (Figure 4B) and at around 1065 nm for the thick ZnS shell NPs (Figure 4C) after seven days. It can be seen that the LSPR of the pristine Cu_{2-x}Se NPs reaches the maximum intensity within one day and changes only slightly thereafter. The development of the LSPRs, and hence the amount of copper vacancies of the core@shell particles, however reaches a relatively stable state only after 5–7 days under air exposure. The small difference in the absolute position and the different time period needed to reach the maximum value is difficult to interpret. The initial oxidation must occur at the ZnS shell with release of Cu^+ ions to the solution and transfer of electrons from the NCs to oxygen as the oxidizing agent similar to the $\text{Cu}_{2-x}\text{Se}@Cu_{2-x}\text{S}$ system described by Misztal et al.^[26] Cu^+ ions need to diffuse through the ZnS film first which can explain the longer duration, compared to the Cu_{2-x}Se NPs, until the maximum LSPR position only changes little within several days. The copper diffusivity of Cu^+ in polycrystalline cubic ZnS $D_{\text{Cu}^+} = 1.0 \times 10^{-11} \text{ cm}^2 \text{ s}^{-1}$ (80 °C)^[27] is a bit less than the high dif-

3 Encapsulation of Cu_{2-x}Se in a Closed ZnS Shell

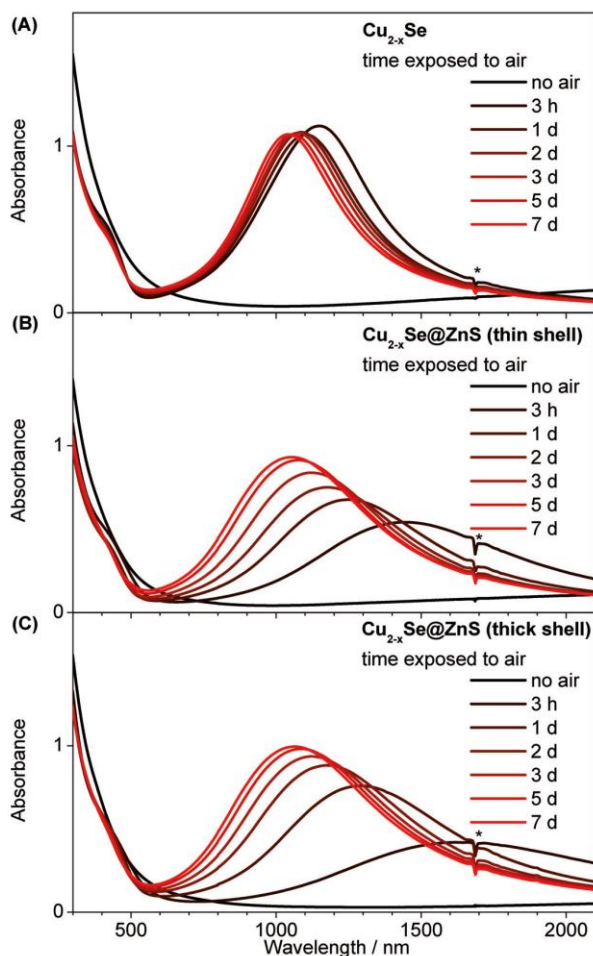


Figure 4. UV/Vis/NIR absorbance spectra of Cu_{2-x}Se (A), Cu_{2-x}Se@ZnS (thin shell) (B), and Cu_{2-x}Se@ZnS (thick shell) (C), showing the emerging LSPR in all three samples due to copper-vacancy formation upon oxygen exposure. *The sharp signal around 1700 nm is due to solvent absorption.

fusivity in chalcocite ($D_{\text{Cu}^+} = 3.5 \times 10^{-10} \text{ cm}^2 \text{ s}^{-1}$ at 73 °C).^[28] As the shell thickness is comparably thin it is likely that the shell slows the oxidation due to the Cu⁺ diffusion through ZnS but not enough to fully prohibit it. Hence it is still possible to slowly oxidize the core resulting in a strong LSPR within a few days. The bathochromic shift for a thicker shell fits well with the expectations. ZnS has, with roughly 2.29–2.27^[29] in the wavelength region from 1000–1550 nm, a higher refractive index than toluene (1.4969), hence a bathochromic shift of the LSPR is expected due to the increase of the refractive index of the dielectric environment surrounding the plasmonic core NP. We performed electrostatics simulations of the extinction spectra of the core-shell particles by means of the MMP method.^[30,31] The dielectric function of Cu_{2-x}Se was calculated, as described by Dorfs et al.,^[1] from the bulk reflectivity measurements reported by Mansour et al.^[32] An *x*-value of 0.15 was used as this value showed the best match between the experi-

mental and theoretical extinction spectra of the pure Cu_{2-x}Se particles. For Cu_{1.85}Se the calculations show an extinction maximum of 1020 nm for the core only NPs and a bathochromic shift of 200 nm for a 1.5 nm shell and of 240 nm for a 2.2 nm shell (see Figure S1 of the Supporting Information, SI). This is a significantly stronger bathochromic shift than we can observe in the synthesized samples by oxidation with air, even so a certain variation is expected due to the standard deviations of the synthesized sample. We considered the influence of alloy formation; however, the solid-state characterization shows no evidence of such a structure. Alloy formation would also cause a further bathochromic shift as the effective size of the plasmonic NPs would increase. Additionally, already small changes of the dielectric function, caused through alloy formation, would lead to a further bathochromic shift.^[33] Another possible reason for this phenomenological discrepancy is that the core@shell NPs reach a higher value of copper deficiency after several days of oxidation. A speculative explanation for the latter might be that the interface between the Cu_{2-x}Se phase and the ZnS phase is especially vacancy rich. However, it must be pointed out that the reason for the only very weakly pronounced bathochromic shift remains not completely understood at this stage. Further comparison of the absorption spectra of pure and core@shell particles shows a broadening of the LSPR band which is also predicted by the theoretical calculations (see Figure 4 and Figure S1).

To show the protective effect of the ZnS shell and its tightness, we treated the core as well as core@shell particles with different reducing agents, namely, BTB and DIBAL. DIBAL was previously shown to bathochromically shift and decrease the intensity of the LSPR of pure copper chalcogenide NPs due to a reduction of copper vacancies.^[34] Our core Cu_{2-x}Se particles behave similarly, as can be seen in Figure 5 for BTB (and in Figure S2 for DIBAL), which shows a bathochromic shift and intensity decrease for the Cu_{2-x}Se NPs after addition of the reducing agent. Adding the same amount of reducing agent to the Cu_{2-x}Se@ZnS sample (thick shell) does not result in any change of the absorption spectra (the small intensity drop directly after addition over the whole spectral range is due to the dilution of the measured sample) and hence obviously reduction of the Cu_{2-x}Se core is completely absent. To support these findings, oxidized, concentrated solutions of both core and core@shell NPs have been treated with BTB and XRD measurements of these samples were measured first under argon and subsequently after exposure to air for several hours (see Figure S3). The XRD patterns show that the reflexes of the core NPs shift to longer wavelength due to the oxidation. The reflexes of the core@shell NPs however do not change, as the particles are already oxidized and did not get reduced by BTB, as the core NPs did. This is an additional evidence of the closed nature of the grown ZnS shell.

Figure S4 shows the absorbance spectra of Cu_{2-x}Se@ZnS (thick shell) NPs in water after successful phase transfer. The core@shell NPs were phase transferred using a facile approach^[35] with the non-toxic, biocompatible^[36] polymer polyvinylpyrrolidone (PVP) as well as with MPA.^[37,38] Both resulted in clear, green dispersions, with a slight tendency to agglomerate

3 Encapsulation of Cu_{2-x}Se in a Closed ZnS Shell

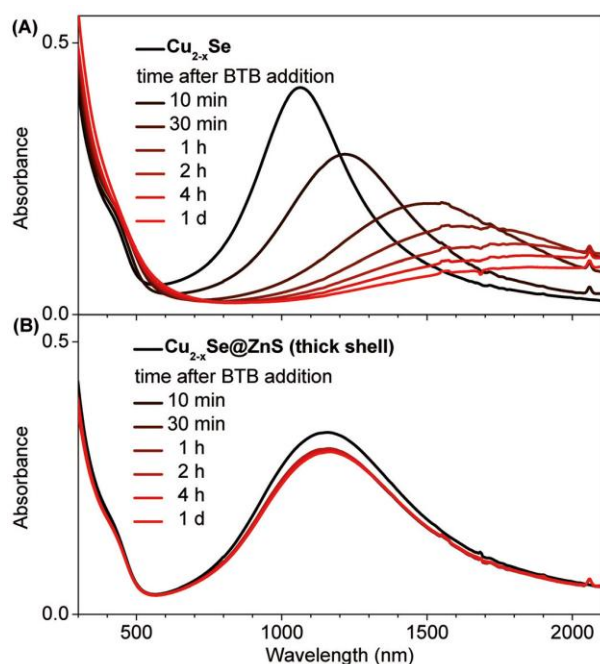


Figure 5. Absorbance spectra of Cu_{2-x}Se (panel A) and Cu_{2-x}Se@ZnS (thick shell) NPs (panel B) before and after the addition of 100 µL 0.25 M BTB solution.

for the NPs transferred with PVP as can be seen in the slightly broadened absorbance spectra of these NPs in water. The LSPRs of the Cu_{2-x}Se@ZnS (thick shell) in water for both phase transfer approaches show a maximum at 1070 nm.

3. Conclusions

We have demonstrated an approach to synthesize plasmonic Cu_{2-x}Se@ZnS core-shell nanoparticles with variable shell thickness. We based this synthesis on quasispherical Cu_{2-x}Se NPs known from the literature,^[23] which we encapsulated with a closed ZnS shell. Solid-state characterization showed that the synthesis led to the growth of a crystalline ZnS shell with no evidence of alloy formation. The absorbance measurements show that the shell allows oxygen-induced oxidation of the Cu_{2-x}Se core to occur, leading to the formation of a strong LSPR band in the NIR, probably due to a possible Cu⁺ diffusion through the ZnS shell. Contrary to this observation, a reduction with reducing agents (BTB and DIBAL) does not occur, showing the protective behavior in a strongly reducing environment.

We compared the measured absorbance spectra of the core and two different core@shell samples with the theoretical values obtained by MMP calculations. The observed difference was rationalized with different oxidation states for the Cu_{2-x}Se core and the Cu_{2-x}Se@ZnS core@shell NPs.

In summary, we showed the growth of a new plasmonic Cu_{2-x}Se@ZnS core@shell structure, which shows a stable plasmonic behavior—also under strongly reducing conditions—while still

being accessible for tuning of the LSPR via oxidative treatment of the particles.

Experimental Section

Materials

Copper (I) chloride (CuCl, 99.99% extra pure), ethanol (EtOH, 99.5%, extra dry), and diethylzinc solution in n-hexane (1 M, ZnEt₂) were purchased from Acros Organics. Methanol (MeOH, 99.9%, anhydrous), selenium (Se, 99.999%, 200 mesh), borane tert-butylamine complex (BTB, 97%), and toluene (99.8%, anhydrous under argon) were purchased from Alfa Aesar. Hexamethyldisilthiane ((TMS)₂S, 97%) and tri-(*n*-)octyl-phosphine oxide (TOPO, 99%) were purchased from ABCR. Oleylamine (OLA, > 70%), octadecene (ODE, 90%), polyvinylpyrrolidone (PVP, Mw = 10,000), chloroform (anhydrous, ≥ 99%), 3-mercaptopropionic acid (MPA, ≥ 99%), diisobutylaluminum hydride (DIBAL, 1 M in toluene), and potassium hydroxide (KOH, ≥ 85%) were purchased from Sigma Aldrich.

ODE and OLA were placed in separate flasks, purged several times with argon, and refluxed under vacuum ($\leq 1 \times 10^{-3}$ mbar, 115 °C) for 6 h. Afterwards, they were transferred and stored in a glovebox under inter gas to obtain pre-degassed ODE and OLA. All other chemicals were used without any further purification.

Unless otherwise stated, all experiments were conducted under inter gas using a nitrogen-filled glove box or applying standard Schlenk-line techniques under argon.

Synthesis of Cu_{2-x}Se Nanoparticles

A procedure from Deka et al. was adapted to synthesize quasispherical Cu_{2-x}Se NPs.^[13,23] In a 100 mL 3-neck flask, 15 mL OLA and 15 mL ODE were degassed at 115 °C for 3 h under vacuum ($\leq 1 \times 10^{-3}$ mbar). Subsequently, the flask was set under a constant argon flow and cooled to room temperature. CuCl (297 mg, 3 mmol) was added. The mixture was evacuated again and kept at 115 °C for 15 min. The temperature was raised rapidly to 300 °C within 5–6 min after the flask was set again under an argon flow.

Se (117 mg, 1.5 mmol) and pre-degassed OLA (9 mL) were placed in a 25 mL flask and kept at 115 °C for 15 min under vacuum. The flask was purged with argon and heated to 190–200 °C until all Se was dissolved. Subsequently, the temperature was raised to 230 °C for 20 min. After the solution was cooled to 150 °C, it was transferred to a glass syringe and rapidly injected into the Cu precursor solution. The temperature was allowed to recover to 290 °C. The reaction was rapidly cooled down for 15 min after the injection. 20 mL toluene was added at 150 °C. The NPs were precipitated with 20 mL EtOH and 10 mL MeOH and collected by centrifugation (3700 g, 20 min). The NPs were redispersed in 20 mL toluene and ultrasonicated for 5 min. The solution was allowed to stand overnight and was then again centrifuged (3700 g, 20 min) to remove larger side products. The supernatant was collected and stored under argon. The resulting dispersion typically contains 0.044 mmol mL⁻¹ Cu_{2-x}Se (1.9 nmol NPs mL⁻¹).

Synthesis of Cu_{2-x}Se@ZnS Particles

To grow a 2.5 nm-thick ZnS shell on Cu_{2-x}Se (diameter 13.1 nm) nanoparticles, TOPO (12.5 g) was placed in a 50 mL flask and heated to 175 °C for 3 h under vacuum. The temperature was dropped to 60 °C and 3.4 mL Cu_{2-x}Se NPs dispersed in toluene (6.4 nmol

NPs), mixed with 4.5 mL pre-degassed OLA, were injected. The flask was again evacuated for 30 min to remove residual toluene; subsequently, the flask was set under argon and heated to 160 °C.

The calculated amount, 1 M ZnEt₂ (315 μmol, 315 μL), was dissolved in pre-degassed OLA (12.27 mL) to receive a 1:40 diluted solution. The equimolar amount of (TMS)₂S (315 μmol, 66 μL) was dissolved in pre-degassed OLA (12.58 mL). The precursor solutions were filled in separate syringes and parallel added into the reaction solution with a speed of 7.9 mL h⁻¹.

Addition of Reducing Agents

60 μL Cu_{2-x}Se solution and 116 μL Cu_{2-x}Se@ZnS (thick shell) solution were diluted with toluene (12 mL) and oxidized for six days under air. 1 mL of the resulting solutions was transferred to a 4 mm quartz glass cuvette, after storing the oxidized NP solutions for several days under nitrogen. For the reduction with BTB, 100 μL of a 0.25 M solution (21.7 mg BTB in 1 mL toluene) were added to 1 mL of the sample solution. For the reduction with DIBAL, 30 μL of a 0.1 M solution in toluene were added to 1 mL sample solution. The absorbance spectra were recorded in regular time intervals to monitor the changes of the LSPR.

Phase Transfer with MPA

The Cu_{2-x}Se@ZnS (thick shell) NPs were transferred to water, inspired by previous reports from Xie et al. and Wuister et al.^[37,38] 100 μL NP solution were added to n-hexane (4.78 mL).

A second solution was prepared by dissolving MPA (1.39 mmol, 121 μL) and KOH (1.8 mmol, 0.1 g) in MeOH (4.68 mL). The two solutions were mixed and shaken for 1 h. After removal of the now colorless hexane phase, the residual solution was centrifuged (3700 g, 5 min) and the resulting precipitate dried under air flow and subsequently dissolved in deionized water (10.5 mL). The PVP-coated particles yielded a clear, green solution when dispersed in water.

Phase Transfer with PVP

For this phase transfer, an approach for Fe₃O₄ NPs was adapted.^[35] 1.5 mL core@shell NPs were precipitated, by addition of MeOH and centrifugation, and subsequently redissolved in CHCl₃ (12 mL). 6 mL of a pre-prepared CHCl₃-PVP solution (25 mg mL⁻¹) was added under stirring. After three days, the NPs were washed by precipitation with n-hexane and centrifugation (14500 g, 5 min). They were subsequently redissolved in MeOH. For transfer to water, the MeOH was evaporated and the precipitate redissolved in deionized water.

UV/Vis/NIR Absorbance Spectroscopy

Samples were dispersed in the chosen solvent and filled in a 10 mm-path-length quartz glass cuvette (4 mm for reduction experiments). The spectra were recorded using an Agilent Cary 5000 UV/Vis/NIR spectrophotometer.

Electron Microscopy

Conventional TEM and HRTEM images were measured using a FEI Tecnai G2 F20, equipped with a field-emission gun operated at 200 kV.

HAADF-STEM images and EDX mappings in the STEM mode were measured using a JEOL JEM-2100F operated at 200 kV and equipped with a field-emission gun.

Samples were prepared by dropping 10 μL of a diluted particle solution on a carbon-coated copper grid (QUANTIFOIL, 300 mesh) that was placed on a filter paper. For elemental mappings, a carbon-coated gold grid (QUANTIFOIL, 300 mesh) was used.

Calculation of the NP Extinction Spectra

We performed electrodynamic simulations of the extinction spectra of the core-shell particles using the MMP method^[30,31] and the dielectric data for ZnS reported in ref. [29]. The dielectric function of Cu_{2-x}Se was calculated, as described in ref. [1], from the bulk reflectivity measurements reported in ref. [32]. An x-value of 0.15 was used as this value showed the best match between the experimental and theoretical extinction spectra of the pure Cu_{2-x}Se particles. Toluene, with a refractive index of $n=1.4969$, was used as the surrounding medium. The particles were assumed to be spherical with a core of 13 nm diameter and shells of 1.5 and 2.2 nm, respectively.

Acknowledgements

D.D. is grateful to the German research foundation (DFG) for funding (DFG research Grants DO 1580/2-1 and DO 1580/3-1). Furthermore, D.D. is grateful to the Volkswagen foundation (lower Saxony/Israel cooperation, Grant ZN2916). The authors are thankful to the Laboratory of Nano and Quantum Engineering of the Leibniz Universität Hannover. T.H. acknowledges funding from the Fraunhofer internal programs (grant number 692271).

Keywords: core-shell nanoparticles · materials science · plasmon resonances · quantum dots · synthesis

- [1] D. Dorfs, T. Härtling, K. Miszta, N. C. Bigall, M. R. Kim, A. Genovese, A. Falqui, M. Povia, L. Manna, *J. Am. Chem. Soc.* **2011**, *133*, 11175–11180.
- [2] J. M. Luther, P. K. Jain, T. Ewers, A. P. Alivisatos, *Nat. Mater.* **2011**, *10*, 361–366.
- [3] M. Kanehara, H. Koike, T. Yoshinaga, T. Teranishi, *J. Am. Chem. Soc.* **2009**, *131*, 17736–17737.
- [4] A. Comin, L. Manna, *Chem. Soc. Rev.* **2014**, *43*, 3957–3975.
- [5] X. Liu, M. T. Swihart, *Chem. Soc. Rev.* **2014**, *43*, 3908–3920.
- [6] S. Link, Z. L. Wang, M. A. El-Sayed, *J. Phys. Chem. B* **1999**, *103*, 3529–3533.
- [7] S. Link, M. El-Sayed, *J. Phys. Chem. B* **1999**, *103*, 4212–4217.
- [8] S. J. Oldenburg, R. D. Averitt, S. L. Westcott, N. J. Halas, *Chem. Phys. Lett.* **1998**, *288*, 243–247.
- [9] T. K. Sau, A. L. Rogach, F. Jaeckel, T. A. Klar, J. Feldmann, *Adv. Mater.* **2010**, *22*, 1805–1825.
- [10] C. J. Murphy, T. K. Sau, A. M. Gole, C. J. Orendorff, J. Gao, L. Gou, S. E. Huynh, T. Li, *J. Phys. Chem. B* **2005**, *109*, 13857–13870.
- [11] A. N. Bashkatov, E. A. Genina, V. I. Kochubey, V. V. Tuchin, *J. Phys. D* **2005**, *38*, 2543–2555.
- [12] E. Gullotti, Y. Yeo, *Mol. Pharm.* **2009**, *6*, 1041–1051.
- [13] A. Wolf, T. Kodanek, D. Dorfs, *Nanoscale* **2015**, *7*, 19519–19527.
- [14] C. Kirchner, T. Liedl, S. Kudera, T. Pellegrino, A. Munoz Javier, H. E. Gaub, S. Stolzle, N. Fertig, W. J. Parak, *Nano Lett.* **2005**, *5*, 331–338.
- [15] J. P. Zimmer, S. Kim, S. Ohnishi, E. Tanaka, J. V. Frangioni, M. G. Bawendi, *J. Am. Chem. Soc.* **2006**, *128*, 2526–2527.
- [16] S. Link, M. B. Mohamed, M. El-Sayed, *J. Phys. Chem. B* **1999**, *103*, 3073–3077.
- [17] M. Chanana, L. Liz-Marzan, *Nanophotonics* **2012**, *1*, 199–220.

3 Encapsulation of Cu_{2-x}Se in a Closed ZnS Shell

- [18] V. Lesnyak, R. Brescia, G. C. Messina, L. Manna, *J. Am. Chem. Soc.* **2015**, *137*, 9315–9323.
- [19] D. Ha, A. H. Caldwell, M. J. Ward, S. Honrao, K. Mathew, R. Hovden, M. K. A. Koker, D. A. Muller, R. G. Hennig, R. D. Robinson, *Nano Lett.* **2014**, *14*, 7090–7099.
- [20] F. Huang, J. Xu, D. Chen, Y. Wang, *Nanotechnology* **2012**, *23*, 425604.
- [21] F. Huang, X. Wang, J. Xu, D. Chen, Y. Wang, *J. Mater. Chem.* **2012**, *22*, 22614–22618.
- [22] C. V. Durgadas, K. Sreenivasan, C. P. Sharma, *Biomaterials* **2012**, *33*, 6420–6429.
- [23] S. Deka, A. Genovese, Y. Zhang, K. Miszta, G. Bertoni, R. Krahn, C. Giannini, L. Manna, *J. Am. Chem. Soc.* **2010**, *132*, 8912–8914.
- [24] J. Gui, M. Ji, J. Liu, M. Xu, J. Zhang, H. Zhu, *Angew. Chem. Int. Ed.* **2015**, *54*, 3683–3687; *Angew. Chem.* **2015**, *127*, 3754–3758.
- [25] H. Li, M. Zanella, A. Genovese, M. Povia, A. Falqui, C. Giannini, L. Manna, *Nano Lett.* **2011**, *11*, 4964–4970.
- [26] K. Miszta, R. Brescia, M. Prato, G. Bertoni, S. Marras, Y. Xie, S. Ghosh, M. R. Kim, L. Manna, *J. Am. Chem. Soc.* **2014**, *136*, 9061–9069.
- [27] E. Bacaksiz, T. D. Dzhafarov, V. D. Novruzov, K. Oeztuerk, M. Tomakin, T. Kuecukoemeroglu, M. Altunbas, E. Yanmaz, B. Abay, *Phys. Status Solidi A* **2004**, *201*, 2948–2952.
- [28] A. Etienne, *J. Electrochem. Soc.* **1970**, *117*, 870–874.
- [29] *CRC Handbook of Chemistry and Physics, Internet Version 2005* (Ed.: D. R. Lide), CRC Press, Boca Raton, FL, **2005**, p. 12–174.
- [30] C. Hafner, *MaX-1. A visual electromagnetics platform for PCs*, Wiley Sons, Chichester, **1999**.
- [31] C. Hafner, *Post-modern Electromagnetics: Using Intelligent Maxwell Solvers*, Wiley, Chichester, **1999**.
- [32] B. A. Mansour, S. E. Demian, H. A. Zayed, *J. Mater. Sci. Mater. Electron.* **1992**, *3*, 249–252.
- [33] N. C. Bigall, T. Härtling, M. Klose, P. Simon, L. M. Eng, A. Eychmüller, *Nano Lett.* **2008**, *8*, 4588–4592.
- [34] I. Kriegel, C. Jiang, J. Rodriguez-Fernandez, R. D. Schaller, D. V. Talpin, C. da Enrico, J. Feldmann, *J. Am. Chem. Soc.* **2012**, *134*, 1583–1590.
- [35] G. Lu, S. Li, Z. Guo, O. K. Farha, B. G. Hauser, X. Qi, Y. Wang, X. Wang, S. Han, X. Liu, J. S. DuChene, H. Zhang, Q. Zhang, X. Chen, J. Ma, S. C. J. Loo, W. D. Wei, Y. Yang, J. T. Hupp, F. Huo, *Nat. Chem.* **2012**, *4*, 310–316.
- [36] X. Tan, Z. Wang, J. Yang, C. Song, R. Zhang, Y. Cui, *Nanotechnology* **2009**, *20*, 445102.
- [37] S. F. Wuister, I. Swart, F. van Driel, S. G. Hickey, C. de Mello Donegá, *Nano Lett.* **2003**, *3*, 503–507.
- [38] R. Xie, U. Kolb, J. Li, T. Basche, A. Mews, *J. Am. Chem. Soc.* **2005**, *127*, 7480–7488.

Manuscript received: October 12, 2015

Accepted Article published: November 25, 2015

Final Article published: December 17, 2015

CHEMPHYSCHEM

Supporting Information

Synthesis of Plasmonic $\text{Cu}_{2-x}\text{Se@ZnS}$ Core@Shell Nanoparticles

Andreas Wolf,^[a] Thomas Härtling,^[b] Dominik Hinrichs,^[a] and Dirk Dorfs*^[a]

cphc_201500907_sm_miscellaneous_information.pdf

3 Encapsulation of Cu_{2-x}Se in a Closed ZnS Shell

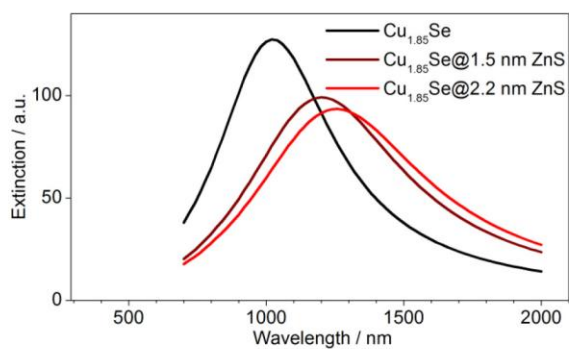


Figure S1. Electrodynamic simulations of the extinction spectra of Cu_{2-x}Se (diameter 13 nm), and $\text{Cu}_{2-x}\text{Se}@ZnS$ NPs with a 1.5 nm and a 2.2 nm thick shell using an x-value of 0.15.

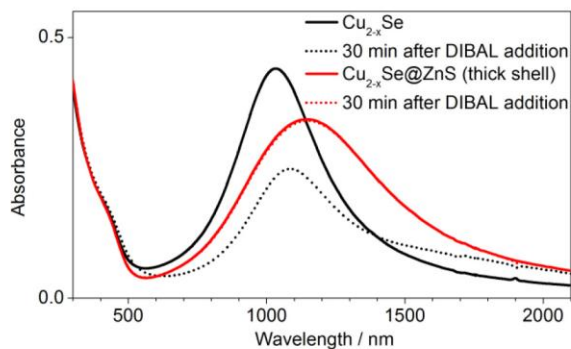


Figure S2. Absorbance spectra of Cu_{2-x}Se (black) and $\text{Cu}_{2-x}\text{Se}@ZnS$ (thick shell) NPs (red) before and 30 min after treatment with 30 μl of a 0.1 M DIBAL solution in toluene.

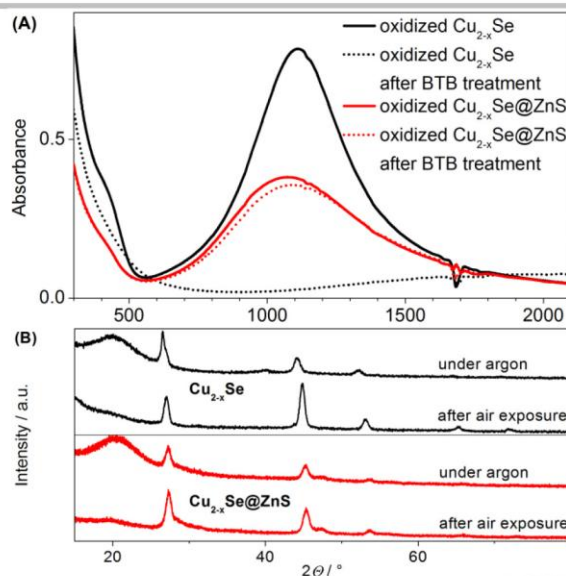


Fig. S3. UV/Vis absorbance spectra (A) of Cu_{2-x}Se core NPs (black) and $\text{Cu}_{2-x}\text{Se}@ZnS$ (thick shell) NPs (red) that have been oxidized (solid lines) and were subsequently treated with the reducing agent BTB for 30 minutes (dotted lines). XRD patterns of the BTB treated NPs under argon and after exposure to air for several hours.

To show the protective effect of the ZnS shell against reducing agents, XRD measurements have been conducted additional to the absorbance measurements (Figure S4 (B)). Concentrated solutions of Cu_{2-x}Se core NPs and $\text{Cu}_{2-x}\text{Se}@ZnS$ (thick shell) NPs that have been oxidized under air were subsequently treated with the reducing agent BTB for 30 minutes inside the glove box. As shown earlier in this publication this treatment of the Cu_{2-x}Se NPs bathochromically shift the LSPR band accompanied by a near fully decrease of its intensity (figure S4 A). $\text{Cu}_{2-x}\text{Se}@ZnS$ (thick shell) NPs show however a nearly unaltered absorbance spectra after the same treatment, as has been shown earlier in this publication (see figure 5). The samples were precipitated under argon atmosphere on a Si crystal of a sample holder that enables XRD measurement under argon atmosphere. After measuring the XRD patterns under argon (figure S4B), the samples were exposed to air for several hours. The reflexes of the Cu_{2-x}Se sample shift by 0.6° to larger 2θ angles due to oxidation. The reflexes in the $\text{Cu}_{2-x}\text{Se}@ZnS$ (thick shell) sample do not change, as expected from the absorbance spectra.

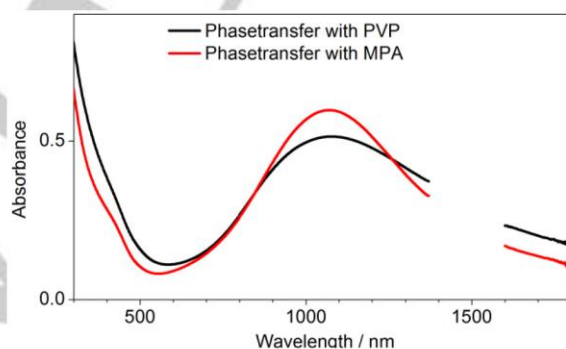


Figure S4. Absorbance spectra of $\text{Cu}_{2-x}\text{Se}@ZnS$ (thick shell) in water after phase transfer with MPA (red) and PVP (black) in water. The spectra show an absorbance maximum of 1070 nm for both approaches. The spectral region from 1370 nm-1600 nm is not shown, due to strong absorption of water in that spectral region.

4 Encapsulation of Plasmonic Semiconductor NPs in a Porous Shell

4.1 Summary

Combining the outstanding optical properties of degenerately doped semiconductor NPs with the ones of MOFs, gives rise to composites that promise a vast amount of possible applications in sensing and catalysis. As described in chapter 1.5.1, MOFs are characterized by their homogenous framework with defined cavity and gate sizes, as well as high surface area. The following chapter 4.2 describes the fusion of their exceptional properties with the tunable plasmonic resonances of degenerately doped semiconductor NPs in composite particles. Specifically, the successful encapsulation of the plasmonic NPs in ZIF-8 is presented, resulting in $\text{Cu}_{2-x}\text{Se}@ZIF-8$ and $\text{ITO}@ZIF-8$ particles, representing typical examples of p-type and n-type doped semiconductors, respectively.

The presented fabrication procedure allows independent control over composite particle's size and NP loading. The comparison of the NP's and composite's spectra show the preservation of the LSPRs during the encapsulation process. Moreover, the LSPR of the Cu_{2-x}Se NPs could still be tuned by oxidation while already being integrated in the $\text{Cu}_{2-x}\text{Se}@ZIF-8$ composite. The integration of the NPs was achieved without crystallographic changes compared to the starting NPs. Electron microscopy revealed that the NPs were fully built in the composite without agglomeration. Elemental mapping with EDX in STEM mode further verified the composition dispersion within the composite, confirming the assignment of the high contrast regions to the integrated NPs.

The suitability of Cu_{2-x}Se NPs for cation exchange reactions is well studied in literature (see chapter 1.2.3) and is also discussed in chapter 2.2. Hence, cation

4 Encapsulation of Plasmonic Semiconductor NPs in a Porous Shell

exchange reactions were used to show the accessibility of the NPs within the $\text{Cu}_{2-x}\text{Se}@ZIF-8$ composites. Due to a gate size of 3.4 Å the ZIF-8 allows the diffusion of added Hg(II) and Ag(I) ions to the embedded Cu_{2-x}Se NPs. A full cation exchange, producing $\text{HgSe}@ZIF-8$ and $\text{Ag}_2\text{Se}@ZIF-8$ composites, was achieved within 90 min. Electron microscopy analysis (incl. EDX), as well as XRD showed the full exchange of the Cu_{2-x}Se NPs, without influencing the composition or structural integrity of the metal-organic framework. With this experiments the accessibility of the physically from the environment separated, and from agglomeration protected semiconductor NPs is proven.

4.2 Plasmonic Semiconductor Nanoparticles in a Metal-Organic Framework Structure and Their *in Situ* Cation Exchange

Andreas Wolf, Lisa Diestel, Franziska Lübke, Torben Kodanek, Tarek Mohamed, Jürgen Caro and Dirk Dorfs

Chemistry of Materials 2016, 28, 7511-7518.

Reprinted (adapted) with permission from Chemistry of Materials. Copyright 2016 American Chemical Society.

DOI: [10.1021/acs.chemmater.6b03425](https://doi.org/10.1021/acs.chemmater.6b03425)

Supporting Information is also available online on the journal's website.

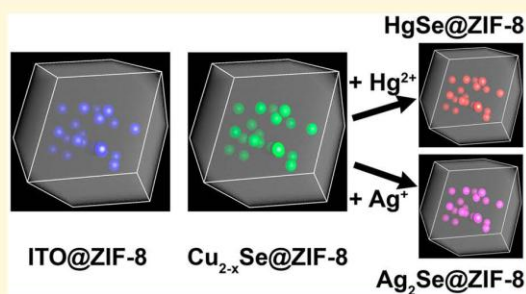
Plasmonic Semiconductor Nanoparticles in a Metal–Organic Framework Structure and Their *in Situ* Cation Exchange

Andreas Wolf, Lisa Diestel, Franziska Lübke, Torben Kodanek, Tarek Mohamed, Jürgen Caro, and Dirk Dorfs*

Institute of Physical Chemistry and Electrochemistry, Leibniz Universität Hannover, Callinstrasse 3A, 30167 Hannover, Germany

Supporting Information

ABSTRACT: Composites of nanoparticles (NPs) in metal–organic frameworks (MOFs) combine the versatile properties of NPs with the defined porosity of MOFs. Here, we show the encapsulation of plasmonic semiconductor NPs in ZIF-8 crystals. Both p-type and n-type doped plasmonic semiconductor NPs (consisting of Cu_{2-x}Se and indium tin oxide, respectively) are encapsulated. The plasmonic and structural properties of each system are preserved during the formation of the composites. Furthermore, we demonstrate the accessibility of the NPs integrated in ZIF-8 via the successful first-time *in situ* cation exchange of MOF-embedded Cu_{2-x}Se NPs to HgSe NPs and Ag_2Se NPs. This ion exchange occurs without influencing the composition or structural integrity of the metal–organic framework. This approach hence allows a fixation of plasmonic nanoparticles avoiding strong plasmon–plasmon coupling but still keeping the plasmonic nanoparticles accessible.



1. INTRODUCTION

The discovery of the origin of the near-infrared (NIR) absorption band in copper chalcogenides has sparked intensive research in degenerately self-doped semiconductor nanoparticles that exhibit localized surface plasmon resonances (LSPRs).^{1–9} Compared to classical metal nanoparticles (NPs), these materials opened a further path for tuning the LSPR. While the tuning for metal NPs is limited to size, shape, and material choice during synthesis, the LSPR of self-doped copper chalcogenides can further be tuned by postsynthetic oxidation and reduction.² In addition, the cation exchange with different cations allows the shift of the LSPR maximum.¹⁰ The accessibility of the copper chalcogenides encouraged studies that use these particles as a starting or intermediate structure for various cation exchange experiments. These reactions can lead to crystallographic phases and shapes that are not directly accessible.^{7,11–20} The LSPR in Cu_{2-x}Se is caused by p-type self-doped free charge carriers.² In contrast to that, indium tin oxide (ITO) is n-type doped. The doping of indium oxide with Sn^{4+} causes a material composition-dependent charge carrier density and thus a tunable NIR LSPR that is stable under ambient conditions.²¹ Hence, these two systems are excellent examples of plasmonic semiconductors with a LSPR in the NIR that are covering p-type as well as n-type doped semiconductors.

Growing shells on a desired core nanoparticle is common practice in nanotechnology for enhancing the properties of the nanoparticle or protecting the core.^{22,23} Our group previously showed the synthesis of plasmonic $\text{Cu}_{2-x}\text{Se}@ZnS$ NPs. The ZnS shell allows the Cu_2Se core to be oxidized to Cu_{2-x}Se and exhibit a strong plasmon absorption band in the NIR after the

oxidation. However, at the same time, the shell protects the oxidized core from reduction with several reducing agents.²⁴

Nanoporous metal–organic framework (MOF) structures have been studied and applied in various applications over the past decade.^{25,26} Their homogeneous structure with a defined cavity and gate size fueled the research efforts in this area. Combining the properties of MOFs with the unique properties of nanosized materials was a logical consequence of achieving highly functional composite materials.^{27–34} Reports on the formation of such composites can mostly be grouped into two approaches. On the one hand, the infiltration of a ready-made MOF structure with the precursor of the desired material, and the subsequent precipitation or reduction inside the existing pores. On the other hand, the growth of a porous MOF structure around the ready-made NPs, whose properties are pretailored, is allowing the NPs not to occupy the pores but rather to be enwrapped by the MOF.³⁴ While the former approach is limited by pore size, the latter allows composite structures, which host NPs with various dimensions and tuned properties as needed for the desired application. A further functionalization step was taken by Zhang et al., who achieved, starting from metal-NP@MOF structures, mesoporous MOFs by removal of the metal NPs via etching.³⁵

We show here, to the best of our knowledge, the first-ever incorporation of plasmonic semiconductor NPs into a MOF structure. While previous works have shown the incorporation

Received: August 17, 2016

Revised: September 30, 2016

Published: September 30, 2016

of several plasmonic metal nanoparticles, plasmonic semiconductor NPs have not been successfully built into MOF NPs to date. In this work, the formation of composite particles consisting of multiple Cu_{2-x}Se NPs or ITO in one ZIF-8 particle resulting in $\text{Cu}_{2-x}\text{Se}@ZIF-8$ or $\text{ITO}@ZIF-8$ composites, respectively, will be shown. In the ZIF-8 lattice, the Zn^{2+} ions are interconnected by methylimidazolate anions forming a sodalite (SOD) topology.³⁶ The resulting composite particles exhibit a strong absorption band in the NIR originating from the LSPR of the incorporated NPs. Oxidation permits the tuning of the Cu_{2-x}Se LSPR inside the $\text{Cu}_{2-x}\text{Se}@ZIF-8$. While postsynthesis cation exchange reactions of the metal nodes of MOFs have been reported previously,^{37–39} no reports are known for the selective cation exchange of NPs embedded in MOFs. We here report for the first time a cation exchange of NPs inside a NP@MOF composite. Specifically, we exchange the Cu_{2-x}Se NPs inside a $\text{Cu}_{2-x}\text{Se}@ZIF-8$ composite with Ag^+ and Hg^{2+} ions, resulting in $\text{HgSe}@ZIF-8$ and $\text{Ag}_2\text{Se}@ZIF-8$ composite particles, without modifying the ZIF-8 host structure. This further demonstrates the accessibility of the plasmonic NPs, while the fixation within the MOF framework prevents an agglomeration of them.

2. EXPERIMENTAL SECTION

Additional information about used materials, the synthesis of quasi-spherical Cu_{2-x}Se NPs, and ITO NPs can be found in the Supporting Information.

2.1. Phase Transfer of Cu_{2-x}Se and ITO NPs. We adapted a PVP phase transfer approach developed for Fe_3O_4 NPs.²⁸ A 0.4 mL Cu_{2-x}Se NP solution in toluene (corresponds to 3.5 mg of Cu_{2-x}Se NPs as determined by AAS) was precipitated by addition of MeOH (180 μL) and EtOH (200 μL) and centrifugation. The precipitate was redissolved in 5 mL of CHCl_3 . While the mixture was being stirred, PVP 55k (63 mg) dissolved in CHCl_3 (2.5 mL) was added to the Cu_{2-x}Se particles. The mixture was left to stir for 10 days. To remove excess PVP, the NPs were precipitated with *n*-hexane (400 μL of *n*-hexane/mL of NP/PVP solution) and centrifugation (14500g). After redissolution in CHCl_3 (3 mL), the precipitation was repeated with 750 μL of *n*-hexane and the NPs were finally redispersed in MeOH (3 mL).

The ITO NPs were collected from a 150 μL solution in toluene by centrifugation (5000g for 5 min), after precipitation with EtOH (100 μL). The precipitate was redissolved in CHCl_3 (150 μL) and precipitated again with 500 μL of EtOH (centrifugation at 10000g for 10 min). The particles were then transferred inside the glovebox, redissolved in CHCl_3 (5 mL), and treated under a nitrogen atmosphere henceforward. The ITO NPs were cleaned by precipitation with *n*-hexane (3.5 mL) and centrifugation (15 min at 14500g). After that, they were redissolved in CHCl_3 (2.8 mL), again precipitated with *n*-hexane (0.7 mL), and centrifuged (15 min at 14500g). The PVP-coated ITO NPs are finally dissolved in MeOH (2.4 mL).

2.2. Growth of $\text{Cu}_{2-x}\text{Se}@ZIF-8$ and $\text{ITO}@ZIF-8$ Composite Particles. The encapsulation of plasmonic Cu_{2-x}Se and ITO NPs into ZIF crystals was adapted from a method previously reported for different NPs;²⁸ 3 mL of PVP-coated NPs in MeOH (concentration of 0.9 mL of NP solution and 2.1 mL of MeOH) was mixed with 15 mL of a 30 mM HMIM in MeOH solution and ultrasonicated for 5 min. Fifteen milliliters of a 30 mM $\text{Zn}(\text{NO}_3)_2$ in MeOH solution was added in one step. After being shaken for 3 s, the reaction mixture was left for 24 h without being agitated.

The ready composite particles were cleaned by repeated centrifugation (1000g) and redispersed in MeOH (6 mL).

2.3. Cu_{2-x}Se Cation Exchange with Ag^+ and Hg^{2+} inside the ZIF-8 Composite. For cation exchange with Hg^{2+} , 40 μL of a 25 mM HgCl_2 solution in MeOH was added to 500 μL of a methanolic solution of the $\text{Cu}_{2-x}\text{Se}@ZIF-8$ composite solution. After 90 min, the

particles were cleaned by being washed three times with fresh MeOH. For cation exchange with Ag^+ , a 25 mM AgNO_3 solution in MeOH was used and the sample was further treated as described above.

2.4. UV/Vis/NIR Absorbance Spectra. Samples were diluted with the chosen solvent and placed in a quartz glass cuvette (4 and 1 mm path lengths). The spectra were recorded in standard transmission mode or the center mounting position of an Agilent DRA-2500 Ulbricht sphere, which was mounted in an Agilent Cary 5000 UV/vis/NIR spectrophotometer.

2.5. Electron Microscopy. Transmission electron microscopy (TEM) measurements were performed on an FEI Tecnai G2 F20 instrument, equipped with a field emission gun operated at 200 kV.

Energy-dispersive X-ray spectroscopy (EDX) and high-angle annular dark-field scanning transmission electron microscopy (HAADF-STEM) measurements were performed with a JEOL JEM-2100F instrument, operated at 200 kV and equipped with a field emission gun. EDX copper mapping cannot be conducted reliably with this setup, because of the high level of background noise caused by copper pole pieces of the transmission electron microscope.

All TEM and EDX sample preparation was conducted by dropping thrice 10 μL of the composite particle solution on a carbon-coated copper grid that is placed on filter paper (gold grid for EDX measurements); no sample thinning was performed.

Scanning electron microscopy (SEM) measurements were performed on a JEOL-JSM-6700F scanning electron microscope, operated at 2.0 kV.

Samples were prepared by drop casting a diluted solution on a graphite sample holder.

2.6. Powder X-ray Diffraction Analysis. A Bruker D8 Advance instrument in reflection mode was used for XRD pattern acquisition. It was operated at 40 kV and 40 mA, with Cu K-alpha radiation.

Samples were prepared by drying the NP solution on a single crystalline sample holder.

2.7. Atomic Absorption Spectroscopy. The copper concentration was determined by atomic absorption spectroscopy (AAS) by applying a Varian AA 140 spectrometer. The solvent of the sample was evaporated, and the precipitate was dissolved in aqua regia (1 part HNO_3 and 3 parts HCl) and diluted with deionized water. The measurements were taken using an acetylene flame at 324.8 nm.

3. RESULTS AND DISCUSSION

3.1. $\text{Cu}_{2-x}\text{Se}@ZIF-8$ Composite Particles. Metal-organic framework ZIF-8 was grown around quasi-spherical Cu_{2-x}Se NPs while their plasmonic properties were preserved. Therefore, the Cu_{2-x}Se NPs were synthesized by adapting a strategy previously reported by Deka et al.⁴⁰

The average size of the pristine, quasi-spherical, and OLA-capped Cu_{2-x}Se NPs of 13.1 ± 1.5 nm is determined by TEM (see Figure S1). These particles are coated with polyvinylpyrrolidone (PVP) 55k by being stirred in a PVP CHCl_3 solution for several days to ensure successful functionalization with this amphiphilic polymer. The subsequent removal of excess amounts of PVP by repeated washing is essential. Previous works on NP@ZIF-8 composite materials have shown that excess amounts of free PVP hinder the integration of NPs into the ZIF-8 particles, due to competitive adsorption of free PVP molecules on the forming ZIF-8 crystal.²⁸ For a typical synthesis, a $\text{Cu}_{2-x}\text{Se}@PVP$ NP dispersion in methanol (MeOH) is mixed with a 30 mM 2-methylimidazole (HMIM) solution in MeOH, and subsequently, a 30 mM ZnNO_3 solution in MeOH is quickly added. After a short mixing, the reaction solution is left without agitation to allow the undisturbed growth of the composite particles. After 2–3 min, the reaction solution becomes continuously hazy. After 24 h, a brown-greenish-colored precipitate can be observed at the bottom of the reaction vial, while the supernatant is clear and colorless.

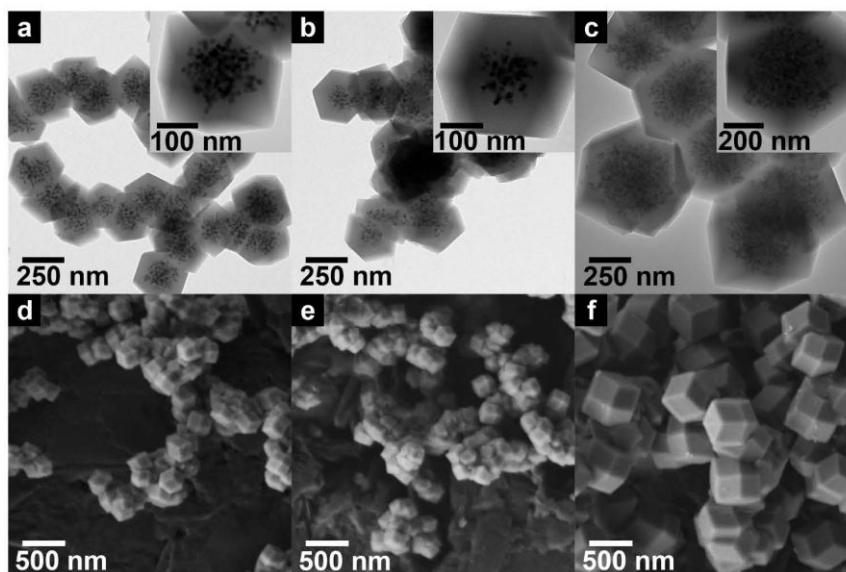


Figure 1. (a–c) TEM and (d–f) SEM micrographs of (a and d) typical $\text{Cu}_{2-x}\text{Se}@ZIF-8$ particles, (b and e) $\text{Cu}_{2-x}\text{Se}@ZIF-8$ particles with a low Cu_{2-x}Se NP concentration, and (c and f) $\text{Cu}_{2-x}\text{Se}@ZIF-8$ composite particles resulting from 50 mM HMIM and ZnNO_3 precursor solutions. The insets show the magnifications of single composite particles.

Transmission electron microscopy reveals the formation of 281 ± 23 nm (smallest distance from edge to edge) sized $\text{Cu}_{2-x}\text{Se}@ZIF-8$ composite crystals, with multiple smaller, higher-contrast Cu_{2-x}Se NPs embedded (Figure 1a). Using in addition the associated SEM micrograph (Figure 1d), we can see that the majority of the ZIF-8-based composite particles exhibit a rhombic dodecahedron shape. However, other shapes such as cubes are also present as described by Cravillon et al.⁴¹ The composite particles agglomerate easily during dispersion. This follows from the TEM and SEM micrographs showing mostly agglomerated particles, but it can also be deduced from the complete self-precipitation of the particle dispersions within 1–2 h. Some particles further exhibit crystal twinning. Because the supernatant of the synthesis, after reaction for 24 h, is colorless and nearly no free Cu_{2-x}Se NPs can be detected in the TEM micrographs, we conclude that with the described synthesis parameters a quantitative integration of the Cu_{2-x}Se NPs into the ZIF-8 crystals can be achieved. The TEM micrographs further show that multiple Cu_{2-x}Se NPs are always integrated in a single ZIF-8 crystal and that these are not agglomerated as described in several previous reports.^{42,43}

Figure 2 shows the elemental mapping of a $\text{Cu}_{2-x}\text{Se}@ZIF-8$ composite particle, established by EDX in the scanning mode of the TEM (STEM). The HAADF-STEM micrograph (Figure 2) of the analyzed composite particle shows the brighter Cu_{2-x}Se

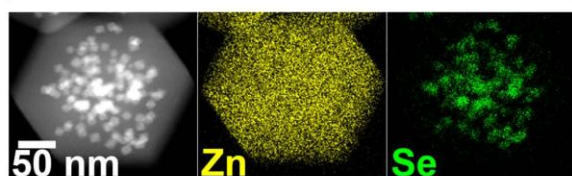


Figure 2. HAADF-STEM micrograph of a $\text{Cu}_{2-x}\text{Se}@ZIF-8$ composite particle and the corresponding EDX mappings for Zn and Se.

NPs that are well dispersed inside the ZIF-8 crystal, as also seen in the TEM bright field images (Figure 1). The larger ZIF-8 crystals, however, exhibit only low contrast, because of their comparably low electron density. As expected, zinc (Zn) can be detected in the whole ZIF-8-based composite particle. The Se mapping of the composite particle shows that selenium (Se) can be detected only in the corresponding high-contrast areas. Thus, we can confirm that the observed NPs are indeed the introduced Cu_{2-x}Se NPs. In the TEM bright field micrographs (Figure 1a) as well as in the HAADF-STEM micrographs (Figure 2), one can see that the embedded Cu_{2-x}Se NPs are well-dispersed inside the ZIF-8 crystals.

The TEM and SEM micrographs in panels b and e, respectively, of Figure 1 show the resulting composite particles when only half of the concentration of Cu_{2-x}Se NPs is used in the ZIF-8 synthesis batch, while all other synthesis parameters are kept the same. The composite particles have an average size of 286 ± 24 nm (smallest distance from edge to edge), hence showing that the size of the composite particles is independent of the concentration of the introduced Cu_{2-x}Se NPs. The same applies for the shape, as also mainly rhombic dodecahedron particles and some cubic-shaped particles are formed. However, it can be observed that the embedded Cu_{2-x}Se NPs are located in a smaller radius around the center of the composite particle. This concentration of the embedded NPs results in a larger NP-free ZIF-8 shell, showing the expected faster NP depletion during ZIF-8 growth. To create larger composite particles, the concentrations of the ZIF-8 precursors (HMIM and ZnNO_3) are increased to 50 mM while all other reaction conditions are kept constant. The resulting $\text{Cu}_{2-x}\text{Se}@ZIF-8$ particles are nearly double in size (619 ± 55 nm, smallest distance from edge to edge), as can be seen in the corresponding TEM and SEM micrographs (panels c and e, respectively, of Figure 1). The particles are mostly rhombic dodecahedral and cubic in shape. It is furthermore evident that the radii in which Cu_{2-x}Se NPs are observed are larger, and no NP-free ZIF-8 particles can

be found. Pure ZIF-8 particles that are received with the described synthesis method have a size of 604 ± 90 nm (see TEM micrographs in Figure S2). The large size of the pure ZIF-8 particles compared to that of the composite particles shows that the addition of the Cu_{2-x}Se NP solution affects the crystallization behavior of the ZIF-8 hosting crystal. Previous works in other NP@MOF composites showed, however, that the crystallization mechanism is homogeneous nucleation and that the NPs are continuously adsorbed on the growing crystal surface until their depletion, rather than acting as centers for heterogeneous nucleation.²⁸ We additionally observed that reducing the NP concentration in the ZIF-8 synthesis batch does not change the particle size of the resulting composite. We speculate, therefore, that small amounts of copper ions in solution, set free due to the partial oxidation of the Cu_{2-x}Se NPs, promote ZIF-8 nucleation and result in composite particles that are smaller than those of pure ZIF-8. Nevertheless, with the method presented herein, the overall composite particle size as well as the NP loading can be adjusted in a controlled way by simply adapting the NP concentration as well as the ZIF-8 precursor concentration.

The LSPR in the Cu_{2-x}Se NPs is caused by a copper deficiency in the system that can, for example, be induced by postsynthetic oxidation of the stoichiometric Cu_2Se system. Recent XPS and Raman spectroscopy studies by the Manna group have shown that only Cu(I), not Cu(II), is present in the crystal and that during oxidation the selenide ions are partially forming diselenides.^{9,13,44} Exposure to oxygen or other oxidizing agents leads to self-doping that causes an increased density of free p-type charge carriers, resulting in the development of the LSPR.² This can be recognized as an increasing intensity of the absorption band in the NIR, which hypsochromically shifts with an increasing copper deficiency. Typically, the absorption band reaches a maximum around 1000–1200 nm after oxidation for several days under air.^{2,10} The pristine Cu_{2-x}Se NPs show only a very weak LSPR at relatively long wavelengths. When they are exposed to air, however, the absorption band evolves and reaches a maximum at 1190 nm after 2 days (see Figure S3). The PVP-functionalized NPs show a weak LSPR band with a maximum at roughly 1700 nm before their exposure to air (see Figure S3). When exposed to air, these NPs develop a stronger LSPR with a maximum comparable to that of the pristine NPs in toluene. The $\text{Cu}_{2-x}\text{Se}@ZIF-8$ composite particles strongly scatter because of their size but also exhibit an absorbance maximum at 1450 nm in normal transmission mode (see Figure 3). Measuring only the absorption of the same sample, by employing an integrating sphere to account for the scattering, results in a spectrum that correspond to that of typical Cu_{2-x}Se NPs. This further shows that while the NPs are fixed in the MOF framework no agglomeration of the NPs occurred, as this would have caused a strong bathochromic shift and broadening of the resonance band. When the NPs are exposed to air, a hypsochromic shift for the LSPR of the composite particle can be detected, as seen for the pristine and PVP-functionalized NPs, and as previously reported.^{2,10} Following this finding, it can be stated that the ZIF-8 crystal around the plasmonic Cu_{2-x}Se NPs does not significantly change their optical properties. However, the oxidation of the Cu_{2-x}Se NPs is slowed, which is most likely due to the kinetic obstruction due to the pore system of the surrounding ZIF-8 host crystal. A further reason for the weak bathochromic shift in comparison to the pristine and PVP-coated NPs could also be a change in the

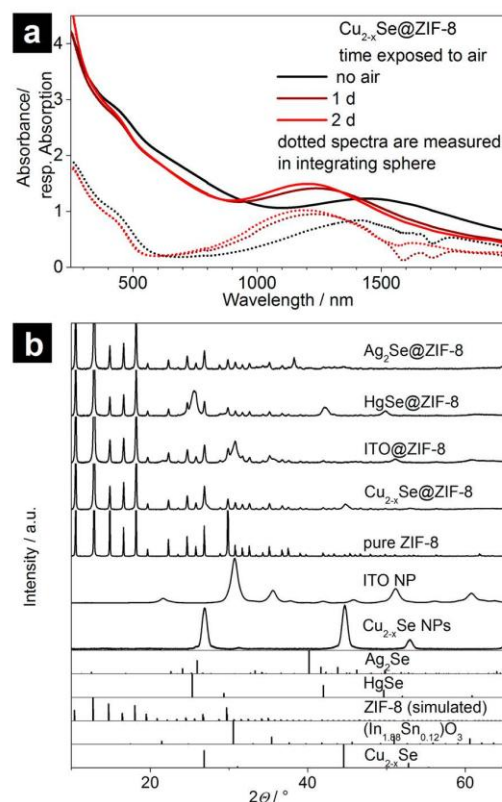


Figure 3. (a) Absorbance spectra of $\text{Cu}_{2-x}\text{Se}@ZIF-8$ composite particles after different periods of exposure to air, measured in transmission mode (solid lines) and absorption spectra in the integrating sphere (dotted lines). (b) XRD patterns of pristine Cu_{2-x}Se and ITO NPs, ZIF-8 particles, and $\text{Cu}_{2-x}\text{Se}@ZIF-8$, ITO@ZIF-8, HgSe@ZIF-8, and Ag₂Se@ZIF-8 composite particles (magnification of the lower-intensity range for pure ZIF-8 and composites, to highlight the reflexes of the embedded NPs; the full intensity range is depicted in Figure S4). The reference structural data show the simulated ZIF-8 pattern, fcc Cu_{2-x}Se berzelianite (PDF Card No. 01-072-7490), bcc $(\text{In}_{1.88}\text{Sn}_{0.12})\text{O}_3$ (PDF Card No. 01-089-4598), fcc HgSe tiemannite (PDF Card No. 00-008-0469), and orthorhombic Ag₂Se naumannite (PDF Card No. 01-089-2591).

dielectric environment of the NPs due to the surrounding ZIF-8 crystal. The refractive index for dense ZIF-8 films given in the literature ranges from 1.54⁴⁵ to 1.584.⁴⁶ Because of the similarity to the refractive index of toluene (1.4950)⁴⁷ and methanol (1.3289),⁴⁷ the effect would be relatively small in comparison to the changes that even small amounts of copper deficiencies cause in the maximal position of the LSPR. Furthermore, the UV/vis/NIR absorbance measurements show no signs of composite decomposition when NPs are exposed to lamp light or daylight.

The X-ray powder diffraction (XRD) pattern (see Figure 3) of the pure Cu_{2-x}Se NPs shows, as previously reported, the cubic berzelianite structure.⁴⁰ Comparing the XRD patterns (see Figure 3 for the lower quarter of the intensity region and Figure S4 for the full intensity range) of pure ZIF-8 particles and of $\text{Cu}_{2-x}\text{Se}@ZIF-8$ particles, one can state that the intensity ratios of the diffraction peaks, which are assigned to ZIF-8, are slightly changed for the composite particles. Additionally, at a 2θ of 26.9° , a slight broadening of the

diffraction peak can be seen, and weak additional diffraction peaks at a 2θ of 44.6° can be observed for the composite. These correspond to the diffraction peaks that are associated with the berzelianite structure of the Cu_{2-x}Se NPs, thus confirming that the integrated NPs did not undergo a phase change during the composite synthesis. The large difference in the intensity ratios between the ZIF-8- and Cu_{2-x}Se -assigned diffraction peaks is caused by the small volume fraction and crystal size of Cu_{2-x}Se compared to those of ZIF-8 in the $\text{Cu}_{2-x}\text{Se}@ZIF-8$ composite particles.

In this paper, we describe for the first time the successful synthesis of plasmonic $\text{Cu}_{2-x}\text{Se}@ZIF-8$ composite particles. The characterization showed that the embedded Cu_{2-x}Se NPs are integrated without agglomeration and retained their structural properties and LSPR. Because of the universality of the approach, which applies PVP to integrate NPs,²⁸ it should also be possible to achieve further copper chalcogenide@ZIF-8 composites, e.g., with Cu_{2-x}S , Cu_{2-x}Te , or ternary copper chalcogenides like CuInS_2 for applications in photocatalysis, solar energy conversion, etc.^{7,48}

3.2. ITO@ZIF-8 Composite Particles. For the synthesis of ITO@ZIF-8 composite particles, we synthesized first ITO NPs, doped with 10% Sn following a method from Kanehara et al.²¹ The ITO NPs stabilized with OLA were coated with PVP and transferred to MeOH, which is similar to the described method for the Cu_{2-x}Se NPs. The ITO NPs have an average size of 8.7 ± 1.5 nm (see the TEM micrograph in Figure S5).

The ITO@ZIF-8 composites were synthesized as described for the $\text{Cu}_{2-x}\text{Se}@ZIF-8$ particles. The resulting precipitate of the composite particles looks white in contrast to the $\text{Cu}_{2-x}\text{Se}@ZIF-8$ composites, because of the lack of ITO absorption features of ITO in the visible range of the spectrum.

The ITO@ZIF-8 composite particles are larger than the comparable $\text{Cu}_{2-x}\text{Se}@ZIF-8$ particles, as one can see in the TEM and SEM micrographs in panels b and c, respectively, of Figure 4. The TEM micrographs further show the good dispersion of the ITO NPs throughout the whole ZIF-8 host crystal. The higher dispersion is likely due to the slightly smaller NP size (compared to Cu_{2-x}Se), but possibly also influenced by a very good colloidal stabilization of the ITO NPs with PVP. The elemental mapping (Figure 4d) indicates the expected assignment of the higher-contrast particles to the ITO NPs containing indium (In) and tin (Sn). XRD analysis (see Figure 3 and Figure S4) shows, furthermore, that these particles did not undergo changes in their body-centered crystallographic structure throughout the phase transfer and composite formation. The optical measurements of the pristine NPs in toluene show a strong LSPR with a maximum at 1880 nm, which originates from the heavy n-type doped free charge carrier concentration.²¹ The coating with PVP and the transfer to MeOH result in a small hypsochromic shift to 1840 nm that is likely caused by the smaller refractive index of MeOH in comparison to that of toluene. The absorbance spectra of the ITO@ZIF-8 composite particles show a strong scattering, caused by the large particles, in the NIR and the visible spectral range as well as a clear maximum at 1856 nm. The absorption spectrum is comparable to that of the pristine and PVP-coated NPs and shows no sign of agglomeration. The LSPR maximum, however, is bathochromically shifted to 1856 nm in comparison to that of the PVP-coated particles. This is expected because the refractive index of ZIF-8 is higher than that of MeOH. Similar to the $\text{Cu}_{2-x}\text{Se}@ZIF-8$ composites, no decomposition can be observed under lamp or daylight exposure.

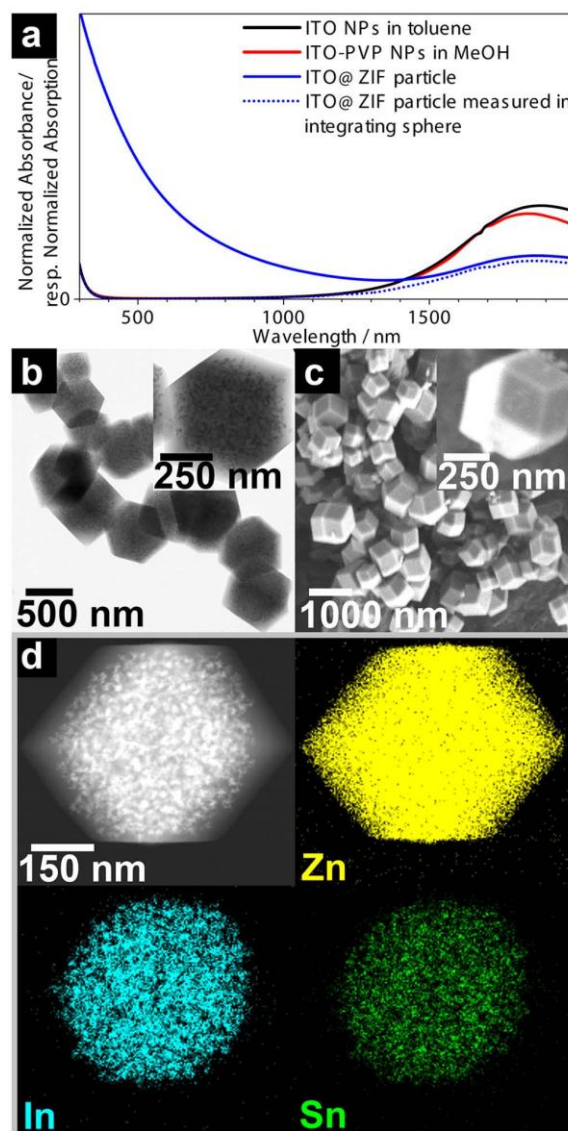


Figure 4. (a) Absorbance spectra of the as-synthesized ITO NPs in toluene (black), the ITO-PVP NPs in MeOH (red), and the ITO@ZIF-8 composite particles (blue) as well as the absorption spectra (measured in an integrating sphere) of the ITO@ZIF-8 composite particles (dotted line). (b) TEM and (c) SEM micrographs of ITO@ZIF-8 particles. (d) HAADF-STEM micrograph and corresponding elemental mappings for Zn, In, and Sn of a typical ITO@ZIF-8 composite particle.

We demonstrate the integration of plasmonic ITO NPs into ZIF-8 crystals while preserving their plasmonic properties. In contrast to the $\text{Cu}_{2-x}\text{Se}@ZIF-8$ particles, the embedded ITO NPs show a fixed LSPR position that cannot be changed by oxidation. Therefore, small variations caused by the changes in the dielectric environment can be detected with greater certainty, in comparison to that for the $\text{Cu}_{2-x}\text{Se}@ZIF-8$ composite. This fact opens the application for size exclusive LSPR-based optical sensing in the NIR region that is not accessible for metal NP LSPR sensing. Furthermore, this

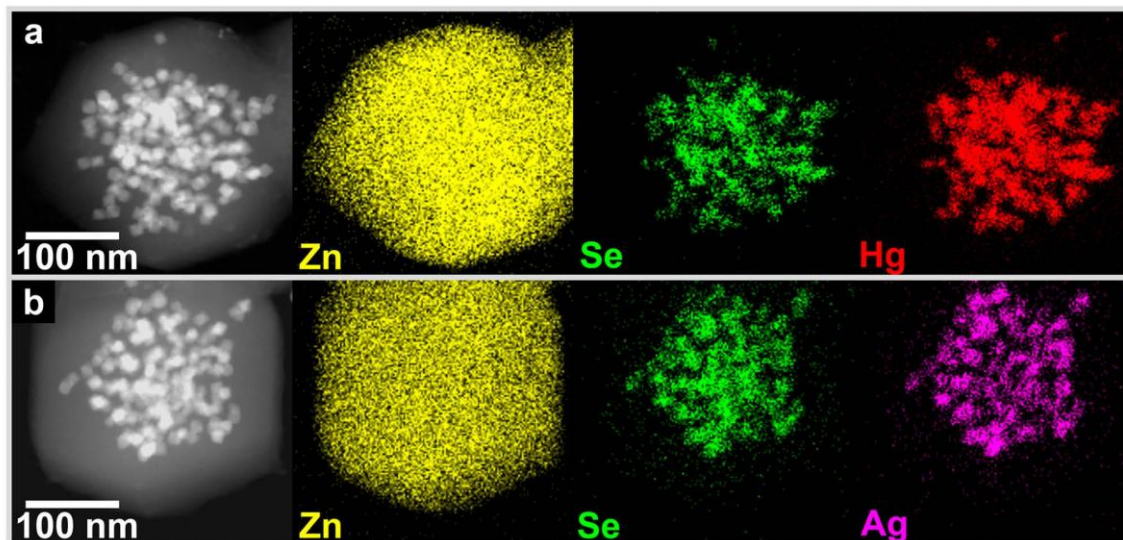


Figure 5. HAADF-STEM micrograph and EDX mapping of Zn, Se, Hg, or Ag for the (a) HgSe@ZIF-8 and (b) Ag₂Se@ZIF-8 composite particles obtained by ion exchange.

finding shows that it is likely that other n-type doped plasmonic oxide particles^{6,8} can also be integrated into ZIF-8 with this universal approach.

3.3. In Situ Cation Exchange of NPs inside the Cu_{2-x}Se@ZIF-8 Composite. Copper chalcogenide systems have been shown to be a very versatile starting material (or intermediate) for cation exchange reactions.^{7,49–51} Consequently, we analyzed the behavior of the Cu_{2-x}Se@ZIF-8 composite particles upon their exposure to Ag⁺ and Hg²⁺ ions in the solvent methanol. As demonstrated in Figure S6, the addition of both ions leads to the complete disappearance of the LSPR, as it was previously observed for plain nonembedded and therefore freely accessible Cu_{2-x}Se NPs.^{10,11} Analyzing the subsequently washed particles via TEM (Figure S7) shows that the composite particles have average sizes of 257 ± 28 nm (Hg²⁺) and 255 ± 22 nm (Ag⁺). Despite the minimal etching at the ZIF-8 edges, the embedded NPs are still fully encapsulated after treatment with Ag⁺ or Hg²⁺ ions for ~2 h. The elemental mapping in Figure 5 shows that the Cu_{2-x}Se NPs underwent complete ion exchange and were transformed into Ag₂Se or HgSe NPs. However, no evidence that the added ions exchanged with the Zn²⁺ ions in the ZIF-8 framework could be found. These results are further supported by the corresponding XRD patterns (see Figure 3 and Figure S4), showing the clear disappearance of the Cu_{2-x}Se berzelianite diffraction peaks (e.g., at 2θ values of 26.9° and 44.6°) for both cation exchanges. The appearance of new strong refraction peaks at 2θ values of 25.5° and 42.0°, which can be assigned to face-centered cubic HgSe (PDF Card No. 00-008-0469) when Hg²⁺ is added, is proof of the formation of HgSe@ZIF-8 composite particles. While the exchange with Ag⁺ ions also leads to the disappearance of the berzelianite structure, the new crystal phase formed cannot be identified with absolute certainty due to the low diffraction peak intensities of the resulting silver selenide phase. However, because of previous results for Ag⁺ cation exchange with Cu_{2-x}Se NPs and the elemental mapping discussed above, the formation of the orthorhombic Ag₂Se naumannite phase can be anticipated.^{10,49}

The ZIF-8 windows that connect the larger cavities possess a size of 3.4 Å, and it was shown that even larger molecules can penetrate these through the gate opening effect.^{52,53} Therefore, we suggest that the cations can diffuse through the ZIF-8 pores to the embedded Cu_{2-x}Se NPs because of their comparable small ionic diameters (0.69 Å for Hg²⁺ and 1.00 Å for Ag⁺), which is similar to the situation discussed for the cation exchange of several MOF metal nodes.^{38,39,54} This further reveals the accessibility of the embedded NPs, while they are fixed in the MOF framework.

We show here an innovative approach to achieving new material combinations for NP@MOF composites. We demonstrate that NP@MOF composites, such as Ag₂Se@ZIF-8 and HgSe@ZIF-8, can be synthesized via *in situ* cation exchange.

4. CONCLUSION

In this work, we present the successful integration of two plasmonic semiconductor systems into the nanoporous MOF type ZIF-8. We call them Cu_{2-x}Se@ZIF-8 and ITO@ZIF-8 composite particles. Both the p-type doped Cu_{2-x}Se NPs and the n-type doped ITO NPs preserve their LSPR while being incorporated into the respective ZIF-8 composite structure. The Cu_{2-x}Se@ZIF-8 composite further showed that the LSPR can still be tuned by oxidation, comparable to the case for pristine Cu_{2-x}Se NPs, while the LSPR of ITO@ZIF-8 particles was found to be stable under ambient conditions. Therefore, both systems are potentially interesting for sensory application in which the ZIF network is discriminating on the basis of size the access to the LSPR particles and can be used for optical sensing of redox active substances (Cu_{2-x}Se) or for simply sensing changes in the dielectric surrounding (ITO).

Furthermore, we showed that, while being physically protected from the environment and from agglomeration, the NPs are still accessible as can be seen from ion exchange reactions. Via this straightforward strategy, we successfully synthesized HgSe@ZIF-8 and Ag₂Se@ZIF-8 composite particles starting from the Cu_{2-x}Se@ZIF-8 composites through an *in situ* cation exchange that is not destroying the ZIF-8

framework. Thus, ion exchange shows a possible approach to functionalized ZIF-8 composite particles that might not be accessible via direct synthesis.

■ ASSOCIATED CONTENT

Supporting Information

The Supporting Information is available free of charge on the ACS Publications website at DOI: 10.1021/acs.chemmater.6b03425.

Further experimental details; TEM micrographs of Cu_{2-x}Se NPs, ITO NPs, and ZIF-8 particles as well as HgSe@ZIF-8 and $\text{Ag}_2\text{Se@ZIF-8}$ composite particles; absorbance spectra of Cu_{2-x}Se NPs and *in situ* cation exchange; and XRD patterns (PDF)

■ AUTHOR INFORMATION

Corresponding Author

*E-mail: dirk.dorfs@pci.uni-hannover.de.

Notes

The authors declare no competing financial interest.

■ ACKNOWLEDGMENTS

The authors are grateful to the German Research Foundation (DFG) for funding (DFG Research Grants DO 1580/2-1 and DO 1580/3-1). The authors thank the Laboratory of Nano and Quantum Engineering of the Leibniz Universität Hannover and the Volkswagen foundation (lower Saxony/Israel cooperation, Grant ZN2916). T.K. is grateful to the Hannover School for Nanotechnology (HSN) for funding.

■ REFERENCES

- Luther, J. M.; Jain, P. K.; Ewers, T.; Alivisatos, A. P. Localized Surface Plasmon Resonances Arising from Free Carriers in Doped Quantum Dots. *Nat. Mater.* **2011**, *10*, 361–366.
- Dorfs, D.; Härtling, T.; Miszta, K.; Bigall, N. C.; Kim, M. R.; Genovese, A.; Falqui, A.; Povia, M.; Manna, L. Reversible Tunability of the Near-Infrared Valence Band Plasmon Resonance in Cu_{2-x}Se Nanocrystals. *J. Am. Chem. Soc.* **2011**, *133*, 11175–11180.
- Zhao, Y.; Burda, C. Development of Plasmonic Semiconductor Nanomaterials with Copper Chalcogenides for a Future with Sustainable Energy Materials. *Energy Environ. Sci.* **2012**, *5*, 5564–5576.
- Xie, Y.; Riedinger, A.; Prato, M.; Casu, A.; Genovese, A.; Guardia, P.; Sottini, S.; Sangregorio, C.; Miszta, K.; Ghosh, S.; Pellegrino, T.; Manna, L. Copper Sulfide Nanocrystals with Tunable Composition by Reduction of Covellite Nanocrystals with Cu^+ Ions. *J. Am. Chem. Soc.* **2013**, *135*, 17630–17637.
- Kriegel, I.; Rodríguez-Fernández, J.; Wisnet, A.; Zhang, H.; Waurisch, C.; Eychmüller, A.; Dubavik, A.; Govorov, A. O.; Feldmann, J. Shedding Light on Vacancy-Doped Copper Chalcogenides: Shape-Controlled Synthesis, Optical Properties, and Modeling of Copper Telluride Nanocrystals with Near-Infrared Plasmon Resonances. *ACS Nano* **2013**, *7*, 4367–4377.
- Comin, A.; Manna, L. New Materials for Tunable Plasmonic Colloidal Nanocrystals. *Chem. Soc. Rev.* **2014**, *43*, 3957–3975.
- van der Stam, W.; Berends, A. C.; de Mello Donega, C. Prospects of Colloidal Copper Chalcogenide Nanocrystals. *ChemPhysChem* **2016**, *17*, 559–581.
- Liu, X.; Swihart, M. T. Heavily-Doped Colloidal Semiconductor and Metal Oxide Nanocrystals: an Emerging New Class of Plasmonic Nanomaterials. *Chem. Soc. Rev.* **2014**, *43*, 3908–3920.
- Hessel, C. M.; Pattani, V. P.; Rasch, M.; Panthani, M. G.; Koo, B.; Tunnell, J. W.; Korgel, B. A. Copper Selenide Nanocrystals for Photothermal Therapy. *Nano Lett.* **2011**, *11*, 2560–2566.
- Wolf, A.; Kodanek, T.; Dorfs, D. Tuning the LSPR in Copper Chalcogenide Nanoparticles by Cation Intercalation, Cation Exchange and Metal Growth. *Nanoscale* **2015**, *7*, 19519–19527.
- Zhang, H.; Xia, Y. Ratiometry, Wavelength, and Intensity: Triple Signal Readout for Colorimetric Sensing of Mercury Ions by Plasmonic Cu_{2-x}Se Nanoparticles. *ACS Sens.* **2016**, *1*, 384–391.
- Bouet, C.; Laufer, D.; Mahler, B.; Nadal, B.; Heuclin, H.; Pedetti, S.; Patriarche, G.; Dubertret, B. Synthesis of Zinc and Lead Chalcogenide Core and Core/Shell Nanoplatelets Using Sequential Cation Exchange Reactions. *Chem. Mater.* **2014**, *26*, 3002–3008.
- Lesnyak, V.; Brescia, R.; Messina, G. C.; Manna, L. Cu Vacancies Boost Cation Exchange Reactions in Copper Selenide Nanocrystals. *J. Am. Chem. Soc.* **2015**, *137*, 9315–9323.
- Xie, Y.; Bertoni, G.; Riedinger, A.; Sathya, A.; Prato, M.; Marras, S.; Tu, R.; Pellegrino, T.; Manna, L. Nanoscale Transformations in Covellite (CuS) Nanocrystals in the Presence of Divalent Metal Cations in a Mild Reducing Environment. *Chem. Mater.* **2015**, *27*, 7531–7537.
- Miszta, K.; Dorfs, D.; Genovese, A.; Kim, M. R.; Manna, L. Cation Exchange Reactions in Colloidal Branched Nanocrystals. *ACS Nano* **2011**, *5*, 7176–7183.
- Adel, P.; Wolf, A.; Kodanek, T.; Dorfs, D. Segmented CdSe@CdS/ZnS Nanorods Synthesized via a Partial Ion Exchange Sequence. *Chem. Mater.* **2014**, *26*, 3121–3127.
- Deka, S.; Miszta, K.; Dorfs, D.; Genovese, A.; Bertoni, G.; Manna, L. Octapod-Shaped Colloidal Nanocrystals of Cadmium Chalcogenides via “One-Pot” Cation Exchange and Seeded Growth. *Nano Lett.* **2010**, *10*, 3770–3776.
- Akkerman, Q. A.; Genovese, A.; George, C.; Prato, M.; Moreels, I.; Casu, A.; Marras, S.; Curcio, A.; Scarpellini, A.; Pellegrino, T.; Manna, L.; Lesnyak, V. From Binary Cu_2S to Ternary Cu-In-S and Quaternary Cu-In-Zn-S Nanocrystals with Tunable Composition via Partial Cation Exchange. *ACS Nano* **2015**, *9*, 521–531.
- Rivest, J. B.; Jain, P. K. Cation Exchange on the Nanoscale: an Emerging Technique for New Material Synthesis, Device Fabrication, and Chemical Sensing. *Chem. Soc. Rev.* **2013**, *42*, 89–96.
- Beberwyck, B. J.; Surendranath, Y.; Alivisatos, A. P. Cation Exchange: A Versatile Tool for Nanomaterials Synthesis. *J. Phys. Chem. C* **2013**, *117*, 19759–19770.
- Kanehara, M.; Koike, H.; Yoshinaga, T.; Teranishi, T. Indium Tin Oxide Nanoparticles with Compositionally Tunable Surface Plasmon Resonance Frequencies in the Near-IR Region. *J. Am. Chem. Soc.* **2009**, *131*, 17736–17737.
- Ghosh Chaudhuri, R.; Paria, S. Core/Shell Nanoparticles: Classes, Properties, Synthesis Mechanisms, Characterization, and Applications. *Chem. Rev.* **2012**, *112*, 2373–2433.
- Chanana, M.; Liz-Marzan, L. Coating Matters: the Influence of Coating Materials on the Optical Properties of Gold Nanoparticles. *Nanophotonics* **2012**, *1*, 199–220.
- Wolf, A.; Haertling, T.; Hinrichs, D.; Dorfs, D. Synthesis of Plasmonic $\text{Cu}_{2-x}\text{Se@ZnS}$ Core@Shell Nanoparticles. *ChemPhysChem* **2016**, *17*, 717–723.
- Eddaoudi, M.; Sava, D. F.; Eubank, J. F.; Adil, K.; Guillelm, V. Zeolite-Like Metal-Organic Frameworks (ZMOFs): Design, Synthesis, and Properties. *Chem. Soc. Rev.* **2015**, *44*, 228–249.
- Gangu, K. K.; Maddila, S.; Mukkamala, S. B.; Jonnalagadda, S. B. A Review on Contemporary Metal-Organic Framework Materials. *Inorg. Chim. Acta* **2016**, *446*, 61–74.
- Hermes, S.; Schroeter, M.; Schmid, R.; Khodeir, L.; Muhler, M.; Tissler, A.; Fischer, R. W.; Fischer, R. A. Metal@MOF: Loading of Highly Porous Coordination Polymers Host Lattices by Metal Organic Chemical Vapor Deposition. *Angew. Chem., Int. Ed.* **2005**, *44*, 6237–6241.
- Lu, G.; Li, S.; Guo, Z.; Farha, O. K.; Hauser, B. G.; Qi, X.; Wang, Y.; Wang, X.; Han, S.; Liu, X.; DuChene, J. S.; Zhang, H.; Zhang, Q.; Chen, X.; Ma, J.; Loo, S. C. J.; Wei, W. D.; Yang, Y.; Hupp, J. T.; Huo, F. Imparting Functionality to a Metal-Organic Framework Material by Controlled Nanoparticle Encapsulation. *Nat. Chem.* **2012**, *4*, 310–316.

- (29) Meilikhov, M.; Yusenko, K.; Esken, D.; Turner, S.; Van Tendeloo, G.; Fischer, R. A. Metals@MOFs - Loading MOFs with Metal Nanoparticles for Hybrid Functions. *Eur. J. Inorg. Chem.* **2010**, *2010*, 3701–3714.
- (30) Doherty, C. M.; Buso, D.; Hill, A. J.; Furukawa, S.; Kitagawa, S.; Falcaro, P. Using Functional Nano- and Microparticles for the Preparation of Metal-Organic Framework Composites with Novel Properties. *Acc. Chem. Res.* **2014**, *47*, 396–405.
- (31) Falcaro, P.; Ricco, R.; Yazdi, A.; Imaz, I.; Furukawa, S.; Maspooh, D.; Ameloot, R.; Evans, J. D.; Doonan, C. J. Application of Metal and Metal Oxide Nanoparticles @ MOFs. *Coord. Chem. Rev.* **2016**, *307*, 237–254.
- (32) Hu, P.; Morabito, J. V.; Tsung, C. Core-Shell Catalysts of Metal Nanoparticle Core and Metal-Organic Framework Shell. *ACS Catal.* **2014**, *4*, 4409–4419.
- (33) Roesler, C.; Fischer, R. A. Metal-Organic Frameworks as Hosts for Nanoparticles. *CrystEngComm* **2015**, *17*, 199–217.
- (34) Aguilera-Sigalat, J.; Bradshaw, D. Synthesis and Applications of Metal-Organic Framework-Quantum Dot (QD@MOF) Composites. *Coord. Chem. Rev.* **2016**, *307*, 267–291.
- (35) Zhang, W.; Liu, Y.; Lu, G.; Wang, Y.; Li, S.; Cui, C.; Wu, J.; Xu, Z.; Tian, D.; Huang, W.; DuCheneu, J. S.; Wei, W. D.; Chen, H.; Yang, Y.; Huo, F. Mesoporous Metal-Organic Frameworks with Size-, Shape-, and Space-Distribution-Controlled Pore Structure. *Adv. Mater.* **2015**, *27*, 2923–2929.
- (36) Park, K. S.; Ni, Z.; Cote, A. P.; Choi, J. Y.; Huang, R.; Uribe-Romo, F.; Chae, H. K.; O’Keeffe, M.; Yaghi, O. M. Exceptional Chemical and Thermal Stability of Zeolitic Imidazolate Frameworks. *Proc. Natl. Acad. Sci. U. S. A.* **2006**, *103*, 10186–10191.
- (37) Lalonde, M.; Bury, W.; Karagiari, O.; Brown, Z.; Hupp, J. T.; Farha, O. K. Transmetalation: Routes to Metal Exchange within Metal-Organic Frameworks. *J. Mater. Chem. A* **2013**, *1*, 5453–5468.
- (38) Brozek, C. K.; Dinca, M. Cation Exchange at the Secondary Building Units of Metal-Organic Frameworks. *Chem. Soc. Rev.* **2014**, *43*, 5456–5467.
- (39) Deria, P.; Mondloch, J. E.; Karagiari, O.; Bury, W.; Hupp, J. T.; Farha, O. K. Beyond Post-Synthesis Modification: Evolution of Metal-Organic Frameworks Via Building Block Replacement. *Chem. Soc. Rev.* **2014**, *43*, 5896–5912.
- (40) Deka, S.; Genovese, A.; Zhang, Y.; Miszta, K.; Bertoni, G.; Krahn, R.; Giannini, C.; Manna, L. Phosphine-Free Synthesis of p-Type Copper(I) Selenide Nanocrystals in Hot Coordinating Solvents. *J. Am. Chem. Soc.* **2010**, *132*, 8912–8914.
- (41) Cravillon, J.; Schroeder, C. A.; Bux, H.; Rothkirch, A.; Caro, J.; Wiebcke, M. Formate Modulated Solvothermal Synthesis of ZIF-8 Investigated Using Time-Resolved In Situ X-ray Diffraction and Scanning Electron Microscopy. *CrystEngComm* **2012**, *14*, 492–498.
- (42) Tsuruoka, T.; Kawasaki, H.; Nawafune, H.; Akamatsu, K. Controlled Self-Assembly of Metal-Organic Frameworks on Metal Nanoparticles for Efficient Synthesis of Hybrid Nanostructures. *ACS Appl. Mater. Interfaces* **2011**, *3*, 3788–3791.
- (43) Lohe, M. R.; Gedrich, K.; Freudenberg, T.; Kockrick, E.; Dellmann, T.; Kaskel, S. Heating and Separation Using Nanomagnet-Functionalized Metal-Organic Frameworks. *Chem. Commun. (Cambridge, U. K.)* **2011**, *47*, 3075–3077.
- (44) Saldanha, P. L.; Brescia, R.; Prato, M.; Li, H.; Povia, M.; Manna, L.; Lesnyak, V. Generalized One-Pot Synthesis of Copper Sulfide, Selenide-Sulfide, and Telluride-Sulfide Nanoparticles. *Chem. Mater.* **2014**, *26*, 1442–1449.
- (45) Demessence, A.; Boissiere, C.; Grosso, D.; Horcajada, P.; Serre, C.; Ferey, G.; Soler-Illia, G.; Sanchez, C. Adsorption Properties in High Optical Quality NanoZIF-8 Thin Films with Tunable Thickness. *J. Mater. Chem.* **2010**, *20*, 7676–7681.
- (46) Cookney, J.; Ogieglo, W.; Hrabanek, P.; Vankelecom, I.; Fila, V.; Benes, N. E. Dynamic Response of Ultrathin Highly Dense ZIF-8 Nanofilms. *Chem. Commun.* **2014**, *50*, 11698–11700.
- (47) Lide, D. R., Ed. *CRC Handbook of Chemistry and Physics*, Internet Version 2005; CRC Press: Boca Raton, FL, 2005.
- (48) Kolny-Olesiak, J.; Weller, H. Synthesis and Application of Colloidal CuInS₂ Semiconductor Nanocrystals. *ACS Appl. Mater. Interfaces* **2013**, *5*, 12221–12237.
- (49) Miszta, K.; Gariano, G.; Brescia, R.; Marras, S.; De Donato, F.; Ghosh, S.; De Trizio, L.; Manna, L. Selective Cation Exchange in the Core Region of Cu_{2-x}Se/Cu_{2-x}S Core/Shell Nanocrystals. *J. Am. Chem. Soc.* **2015**, *137*, 12195–12198.
- (50) Li, H.; Zanella, M.; Genovese, A.; Povia, M.; Falqui, A.; Giannini, C.; Manna, L. Sequential Cation Exchange in Nanocrystals: Preservation of Crystal Phase and Formation of Metastable Phases. *Nano Lett.* **2011**, *11*, 4964–4970.
- (51) Luther, J. M.; Zheng, H.; Sadtler, B.; Alivisatos, A. P. Synthesis of PbS Nanorods and Other Ionic Nanocrystals of Complex Morphology by Sequential Cation Exchange Reactions. *J. Am. Chem. Soc.* **2009**, *131*, 16851–16857.
- (52) Diestel, L.; Bux, H.; Wachsmuth, D.; Caro, J. Pervaporation Studies of n-Hexane, Benzene, Mesitylene and their Mixtures on Zeolitic Imidazolate Framework-8 Membranes. *Microporous Mesoporous Mater.* **2012**, *164*, 288–293.
- (53) Kolokolov, D. I.; Diestel, L.; Caro, J.; Freude, D.; Stepanov, A. G. Rotational and Translational Motion of Benzene in ZIF-8 Studied by ²H NMR: Estimation of Microscopic Self-Diffusivity and Its Comparison with Macroscopic Measurements. *J. Phys. Chem. C* **2014**, *118*, 12873–12879.
- (54) Fei, H.; Cahill, J. F.; Prather, K. A.; Cohen, S. M. Tandem Postsynthetic Metal Ion and Ligand Exchange in Zeolitic Imidazolate Frameworks. *Inorg. Chem.* **2013**, *52*, 4011–4016.

Supporting Information: Plasmonic Semiconductor
Nanoparticles in a Metal-Organic Framework
Structure and Their *in Situ* Cation Exchange

*Andreas Wolf, Lisa Diestel, Franziska Lübke, Torben Kodanek, Tarek Mohamed, Jürgen Caro and Dirk Dorfs**

Institute of Physical Chemistry and Electrochemistry, Leibniz Universität Hannover,
Callinstrasse 3A, 30167 Hannover, Germany

DOI: 10.1021/acs.chemmater.6b03425

EXPERIMENTAL DETAILS

Materials

Selenium (Se, 99.999%, 200 mesh), toluene (99.8 %, anhydrous under argon), indium(III) acetate (99,99 %), and methanol (MeOH, 99.9 %, anhydrous) were purchased from Alfa Aesar. Polyvinylpyrrolidone (PVP, Mw 55k), octadecene (ODE, 90 %), oleylamine (OLA, >70 %), chloroform (CHCl₃, ≥99 %, anhydrous), dioctyl ether (99 %), tin(II) 2-ethylhexanoate (95 %) and 2-methylimidazole (HMIM, 99 %) were purchased from Sigma Aldrich. Copper (I) chloride

4 Encapsulation of Plasmonic Semiconductor NPs in a Porous Shell

(CuCl, 99.99 %, extra pure), and ethanol (EtOH, 99.5 %, extra dry) were purchased from Acros Organics. Octanoic acid (>99 %) was purchased from Merck.

Pre-degassed OLA was prepared by alternating evacuating of the solvent and purging with argon before it was refluxed under vacuum (115 °C, $\leq 1 \cdot 10^{-5}$ mbar) for 6 h, and subsequently stored under inter gas.

If not stated otherwise, all experiments were carried out under inter gas, either by handling inside the glovebox (nitrogen) or by applying standard Schlenk-line techniques (argon).

Synthesis of Cu_{2-x}Se nanoparticles

We adapted a synthesis procedure previously reported by Deka et al. resulting in quasispherical Cu_{2-x}Se NPs.^{1,2} At 115 °C 15 ml OLA and 15 ml ODE were degassed in a 3-neck flask by heating under reflux at 115 °C and under vacuum ($\leq 1 \cdot 10^{-3}$ mbar) for 3h. The mixture was cooled to room temperature, while the flask was set under a constant argon flow. CuCl (297 mg, 3 mmol) was added to the mixture applying a high argon flow. After evacuating the flask again the mixture was rapidly heated to 300 °C under a constant argon flow.

The Se-Precursor was prepared by placing Se (117 mg, 3 mmol) and pre-degassed OLA (9 ml) in a flask. After it was refluxed at 115 °C for 15 min under vacuum, the temperature was raised to 190 – 200 °C under a constant argon flow. When all Se was dissolved, the mixture was heated to 230°C for 20 min, subsequently cooled down to 150 °C, and transferred to a glass syringe. After rapid injection into the Cu precursor solution the temperature was allowed to recover to 290 °C. 15 min after the injection, the reaction was quenched by cooling to room temperature. At 150 °C 20 ml toluene were added. The NPs were cleaned by precipitating with EtOH and MeOH and collected by centrifugation (3700g, 20min). After being redispersed in toluene the solution

4 Encapsulation of Plasmonic Semiconductor NPs in a Porous Shell

was allowed to stand overnight. The solution was then centrifuged (3700g, 20 min) again to remove agglomerates. The supernatant was collected and stored under argon.

Synthesis of ITO nanoparticles, 10% tin doped

We adapted a synthesis procedure previously reported by Kanehara et al.³ In a 3-neck, 25 ml flask indium(III)acetate (157.7 mg; 0.54 mmol), tin(II) 2-ethylhexanoate (24,3 mg, 0.06 mmol), n-octanoic acid (271,1mg, 1.8 mmol), dioctyl ether (5 ml), and oleylamine (5ml) are mixed and stirred at 80 °C under vacuum for 30 min. Subsequently, the flask was set under a constant argon flow, and was heated at 150 °C for an additional hour. Finally, the temperature was raised to 280 °C, and kept at this temperature for 2 h before the solution was cooled down to room temperature. The ITO NPs were collected by precipitating with ca 20 ml ethanol, and collected with centrifugation (3700 g, 5 min). The NPs were redissolved in 7 ml toluene and stored under air.

REFERENCES

1. Deka, S.; Genovese, A.; Zhang, Y.; Miszta, K.; Bertoni, G.; Krahne, R.; Giannini, C.; Manna, L. Phosphine-Free Synthesis of p-Type Copper(I) Selenide Nanocrystals in Hot Coordinating Solvents. *J. Am. Chem. Soc.* **2010**, *132*, 8912-8914.
2. Wolf, A.; Kodanek, T.; Dorfs, D. Tuning the LSPR in Copper Chalcogenide Nanoparticles by Cation Intercalation, Cation Exchange and Metal Growth. *Nanoscale* **2015**, *7*, 19519-19527.
3. Kanehara, M.; Koike, H.; Yoshinaga, T.; Teranishi, T. Indium Tin Oxide Nanoparticles with Compositionally Tunable Surface Plasmon Resonance Frequencies in the Near-IR Region. *J. Am. Chem. Soc.* **2009**, *131*, 17736-17737.

SUPPORTING INFORMATION FIGURE SECTION

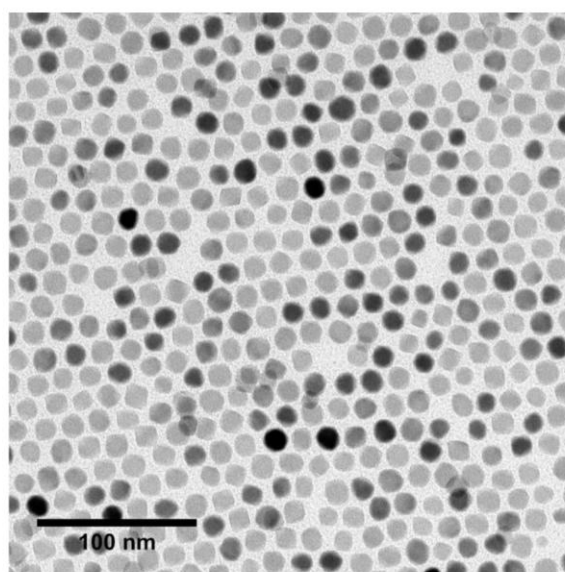


Figure S1. TEM micrograph of Cu_{2-x}Se NPs.

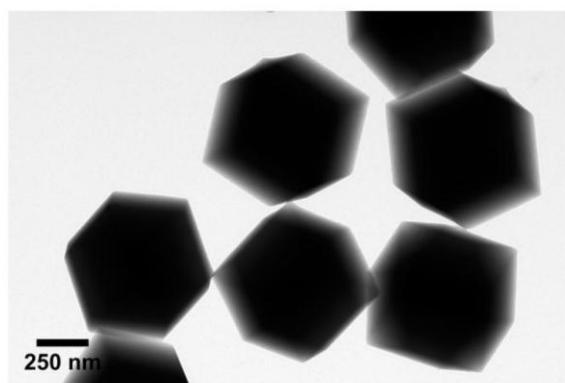


Figure S2. TEM micrograph of pure ZIF-8 crystals without incorporated NPs.

4 Encapsulation of Plasmonic Semiconductor NPs in a Porous Shell

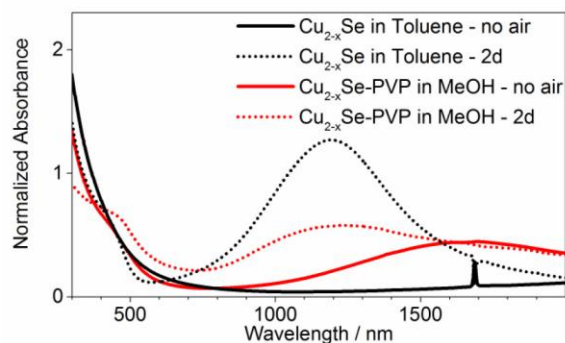


Figure S3. Absorbance spectra of OLA stabilized Cu_{2-x}Se NPs in toluene (black), and with PVP into MeOH transferred Cu_{2-x}Se@PVP NPs (red); no air exposure (solid line) and after 2 d exposure to air (dotted line).

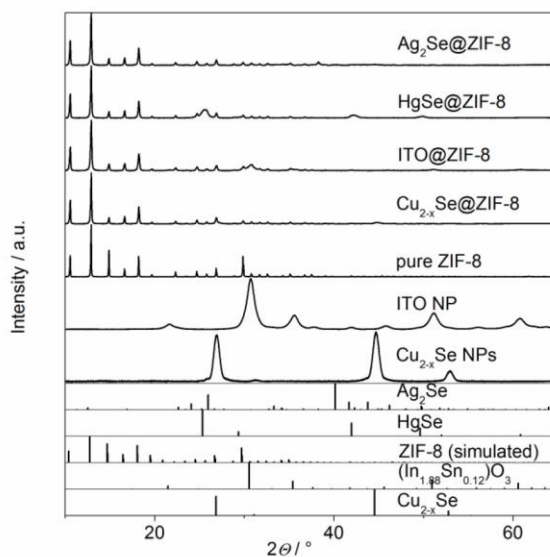


Figure S4. Full intensity range of the XRD pattern as shown in Figure 3b.

4 Encapsulation of Plasmonic Semiconductor NPs in a Porous Shell

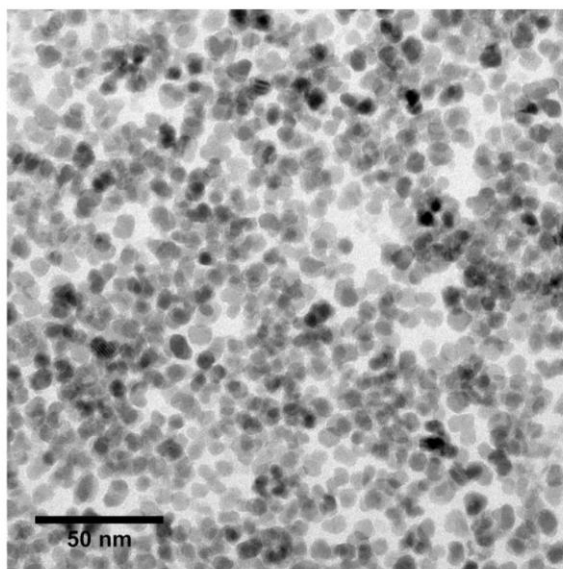


Figure S5. TEM micrograph of pristine ITO NPs. Since most ITO NPs are not spherical, for size determination always the longest edge-to-edge distance was measured.

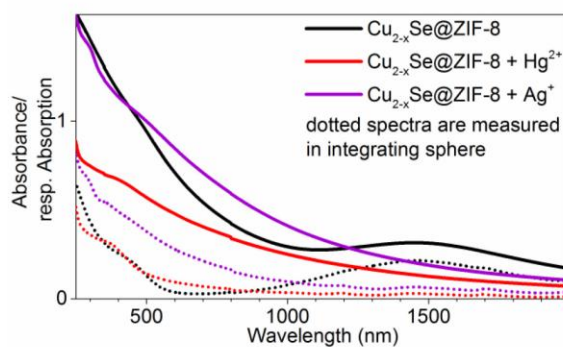


Figure S6. Absorbance spectra (solid lines) of the Cu_{2-x}Se@ZIF-8 composite particles before (black) and after cation exchange with Hg²⁺ (red) or Ag⁺ (magenta) and their corresponding absorption spectra (dotted lines).

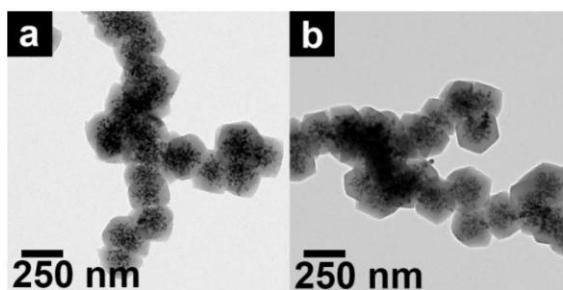


Figure S7. TEM micrographs of composite particles after the cation exchange – HgSe@ZIF-8 (a) and Ag₂Se@ZIF-8 (b). For the Ag⁺ treated sample a few high contrast particles are observed outside the particles, which are larger than the parent Cu_{2-x}Se NPs. Hence, we speculate that a few Ag NPs formed.

5 Closing Remarks

The main focus of the present thesis is the controlled modification of the LSPR of plasmonic copper chalcogenide particles; in particular, from the degenerately self-doped Cu_{2-x}Se NPs and of metallic covellite. While Cu_{2-x}Se NPs exhibit a plasmon only after oxidation, due to the formation of copper vacancies and the conjunct increase of free electron holes in the valence band, covellite exhibits lattice constitutional free electron holes. This work demonstrated different approaches to tune their LSPR, to increase the optical stability under air exposure, as well as against exposure to strong reducing agents. Furthermore, not only the influence of metallic domain growth onto these particles was analyzed, but also their implementation and behavior as part of functional plasmonic NP@MOF composites.

Firstly, in chapter 2 the stability of the LSPR from berzelianite and covellite NPs was assessed after their treatment with Cu(I) ions. The optical characterization showed that the plasmon resonance continued to shift hypsochromically after the treatment, making the achieved adjustments non-permanent. To overcome this fact, in a further step the stability after their treatment with Ag(I) was evaluated. The characterization showed a nearly permanent LSPR tuning. Optical and solid state characterization suggested that in Cu_{2-x}Se NPs Ag(I) exchanges Cu(I), resulting in a controllable damping with only minimal shifting of the maximal LSPR wavelength, because of an increase in scattering centers. In contrast, the treatment of covellite NPs with Ag(I) resulted in a bathochromic shift and damping, comparable to the observations after Cu(I) treatment. This showed that Ag(I) ions intercalate under breaking the S-S bonds, instead of exchanging the Cu(I) ions. Au(I) treatment on the other hand, added in an reducing reaction environment, resulted in a partial cation exchange under the formation of a $\text{Cu}_{1.1}\text{S-Au}_2\text{S}$ core-crown structure.

Chapter 2 also analyzes the effect of the growth of metallic domains on the plasmonic copper chalcogenide NPs. In section 2.2 the fabrication procedure of Au-Cu_{2-x}Se hybrids is developed with controlled Au domain sizes. The hybrid particles (up to a Cu_{2-x}Se:Au ratio of 1:056) exhibit two distinct LSPRs: the one in the visible region originated from the grown Au domain, and the one in the NIR from the Cu_{2-x}Se NP. It was proven by reducing experiments with Cu(I) that they are surprisingly very weakly coupled. This was assumed to be caused by a charge carrier barrier between the domains, possibly due to the mild reaction conditions compared to previously reported hybrids in literature. In section 2.3, it was shown that the attempt to grow Pt domains on Cu_{2-x}Se NPs resulted in the formation of CuPt-Cu_{2-x}Se hybrids with one large cubic CuPt domain, and additionally several small ones for large Cu_{2-x}Se:Pt ratios (1:8). The formation of the alloy domain resulted in a strong damping up to a complete disappearance of the seed NP LSPR. While for larger Pt amounts a clear crystallographic change could be observed, the damping for smaller Pt amounts was assigned to electron injection from the CuPt as a corresponding strong structural change could not be observed at this stage. On the other hand, on covellite particles, Pt growth results in multiple small, and pure Pt domains on the covellite seeds. The damping and finally complete disappearance of the covellite LSPR in the Cu_{1.1}S-Pt hybrids was found to be a combination of electron injection and structural changes. The difference between the two systems is presumable the harsher reaction environments in the Pt growth approach, that most likely lead to a smaller electron barrier between the copper chalcogenide and the Pt (or CuPt) domain in comparison to the Cu_{2-x}Se-Au hybrids. Hence, chapter 2 presented a clear overview of different ways to shift and damp the LSPR of copper chalcogenide NPs in a way that the LSPR shift is stable also under ambient conditions, and to fabricate various metal-copper chalcogenide hybrids with and without conservation of their LSPRs.

The objective of chapter 3 was the physical shielding of single plasmonic Cu_{2-x}Se NPs from their environment. It showed the development of a growth procedure of ZnS shells with defined thicknesses under conservation of the plasmonic properties of the Cu_{2-x}Se core NPs. The resulting Cu_{2-x}Se@ZnS core@shell NPs, were achieved without Zn(II) cation exchange into the core NP, due to the avoidance of oxidation of the seed particles, and a phosphine free reaction medium, both known to facilitate the cation exchange in Cu_{2-x}Se. The ZnS shell was proven to be highly crystalline and

homogeneous for the 2 presented thicknesses of 1.5 nm and 2.2 nm. Despite the fact that the ZnS shell did not prevent the oxygen-induced oxidation of the Cu_{2-x}Se core, it slowed it down considerably from a few hours to several days. The results were further compared to electrodynamic simulations, which suggested a variation of the final degree of oxidation. Most significantly is the behavior of these core@shell particles when treated with strong reducing agents. While the blank Cu_{2-x}Se NPs were reduced as expected, the LSPR of the NPs with a ZnS shell was not altered even with prevalence of harsh environment conditions. For these reasons, they could represent an innovative and interesting option for future applications in different areas including bio-imaging and photothermal therapy.

After achieving the complete encapsulation of the plasmonic NPs, the next step was the fixation of these NPs in a matrix that allows access to the particles. Chapter 4 presents the accomplishment of this with the synthesis of $\text{Cu}_{2-x}\text{Se}@ZIF-8$, as well as $\text{ITO}@ZIF-8$ composite particles. Multiple of the p-type, vacancy doped Cu_{2-x}Se NPs or n-type, tin doped ITO NPs were incorporated in a single ZIF-8 particle with a composite size of 280-600 nm. The synthesis method presented allows the fabrication of composites with independently tunable NP loading and size. The LSPRs of both systems were conserved during the composite fabrication. Even though the LSPR of the $\text{Cu}_{2-x}\text{Se}@ZIF-8$ composite was still tunable by oxygen exposure, $\text{ITO}@ZIF-8$ was found to be stable under ambient conditions. Hence, both are interesting for sensing applications, for example: $\text{Cu}_{2-x}\text{Se}@ZIF-8$ can be applied to detect oxidizing or reducing chemicals, while $\text{ITO}@ZIF-8$ is highly sensitive to changes of the dielectric environment. Furthermore, the ZIF-8 host allows certain size discrimination, and prevents the agglomeration of plasmonic NPs that would considerably alter its optical properties. The direct synthesis of NPs and composites is often the preferred approach; however, it might not always be possible. Consequently, the conversion of the $\text{Cu}_{2-x}\text{Se}@ZIF-8$ composites to $\text{HgSe}@ZIF-8$ and $\text{Ag}_2\text{Se}@ZIF-8$ by *in situ* cation exchange was developed. This straight forward reaction showed, on the one hand the accessibility of the embedded NPs, and on the other hand an approach to simply switch the functional center of a composite without the need of developing a new synthesis strategy. The ZIF-8 structure was conserved unaltered during this cation exchange. As for ZIF-8 a gate opening effect was reported in literature, the formation of composites with more rigid MOFs should be explored in future. Furthermore, the incorporation

into electrical conducting MOFs might be an interesting further research area, enabling *e.g.* photovoltaics and sensing. The composites might be also interesting for photocatalysis.

6 Appendix

Publications included in this thesis

1. Andreas Wolf, Torben Kodanek, and Dirk Dorfs
Tuning the LSPR in copper chalcogenide nanoparticles by cation intercalation,
cation exchange and metal growth
Nanoscale, 2015, 7, 19519-19527.
2. Andreas Wolf, Dominik Hinrichs, Joachim Sann, Jan F. Miethe; Nadja C. Bigall,
and Dirk Dorfs
Growth of Cu_{2-x}Se -CuPt and $\text{Cu}_{1.1}\text{S}$ -Pt Hybrid Nanoparticles
Journal of Physical Chemistry C, 2016, 120, 21925-21931.
3. Andreas Wolf, Thomas Härtling, Dominik Hinrichs and Dirk Dorfs
Synthesis of Plasmonic Cu_{2-x}Se @ZnS Core@Shell Nanoparticles
ChemPhysChem, 2016, 17, 717-723
4. Andreas Wolf, Lisa Diestel, Franziska Lübke, Torben Kodanek, Tarek
Mohamed, Jürgen Caro, and Dirk Dorfs
Plasmonic Semiconductor Nanoparticles in a Metal – Organic Framework Structure
and Their *in Situ* Cation Exchange
Chemistry of Materials, 2016, 28, 7511-7518

Publications not included in this thesis

1. Patrick Adel, Andreas Wolf, Torben Kodanek, and Dirk Dorfs
Segmented CdSe@CdS/ZnS Nanorods Synthesized *via* a Partial Ion Exchange Sequence
Chemistry of Materials, 2014, 26, 3121-3127
2. Sara Sanchez-Paradinas, Dirk Dorfs, Sebastian Friebe, Axel Freytag, Andreas Wolf,
Nadja C. Bigall
Aerogels from CdSe/CdS Nanorods with Ultra-long Exciton Lifetimes and High
Fluorescence Quantum Yields
Advanced Materials (Weinheim, Ger.), 2015, 27, 6152-6156
3. Suraj Naskar, Franziska Lübke, Saher Hamid, Axel Freytag, Andreas Wolf,
Julian Koch, Irina Ivanova, Herbert Pfnür, Dirk Dorfs, Detlef W. Bahnemann and
Nadja C. Bigall
Synthesis of Ternary and Quaternary Au and Pt Decorated CdSe/CdS
Heteronanoplatelets with Controllable Morphology
Advanced Functional Materials, In Press

Curriculum Vitae

Personal Details

Date of birth 05.11.1986
Place of birth Dresden, Germany

Education

03/2012 – present **Doctoral Candidate and Researcher Associate**
Working group of Dr. D. Dorfs/ Prof. J. Caro
Institute for physical chemistry and electrochemistry
(PCI)
Gottfried Wilhelm Leibniz Universität Hannover

10/2009 – 12/2012 **Master of Science, Chemistry**
Technische Universität Dresden

09/2008 – 06/2009 **Exchange Year, Department of Chemistry**
University College London

10/2005 – 09/2008 **Bachelor of Science, Chemistry**
Technische Universität Dresden

09/1998 – 07/2005 **Abitur**
Gymnasium Dresden-Plauen

Acknowledgement

I relish the last years that I worked in the field of plasmonic nanoparticles, and I would like to thank everyone who supported me during this time.

My sincere gratitude goes to my supervisor Dr. Dirk Dorfs, for giving me the opportunity to work with this highly interesting and versatile research topic, with excellent working conditions, and his guidance. Many thanks also for the great support with challenging tasks, manuscript preparations, as well as the freedom to develop my own ideas during the entire time of my thesis.

I would like to extend my gratitude to Prof. Dr. Jürgen Caro, for the opportunity to work in his group and productive discussions. Furthermore, I would also like to thank him, as well as Prof. Dr. Alexander Eychmüller, Prof. Dr. Josef-Christian Buhl and Dr. Nadja-Carola Bigall for being the examiners of my thesis defense.

I am thankful with Prof. Dr. Armin Feldhoff and Frank Steinbach for providing me with excellent knowledge about transmission electron microscopy, and for supporting me in achieving my measurements.

Special thanks goes to all colleagues and members of the Institute of Physical Chemistry and Electrochemistry, for always creating a great working atmosphere in the group, but specially to Torben Kodanek, Dr. Lisa Diestel, Dominik Hinrichs, Franziska Lübke, Tarek Mohamed, Jan Mieth and Axel Freytag. Also I would like to thank Yvonne Gabbey-Uebe and Kerstin Janze as well as everyone from the mechanical and electrical workshop.

To all my friends outside of chemistry I thank for the great memories we made during this time. Specially, I want to thank: Martina, Christoph, Carlos, Varun, Bora and Ross.

My deepest gratitude goes to my family, specially my parents, Birgit and Achim, and my sister Antje for always supporting me during my whole life, and enabling me to

Acknowledgement

reach this point. Most of all, my gratitude goes to Cynthia for her love, understanding, huge patience, endless support, proof reading and for reminding me to take a break from time to time.